

A STUDY OF THE
EQUATORIAL ELECTROJET

(In-situ measurements of magnetic and electric fields)

Thesis Presented by

SARANGAN SAMPATH

to the

GUJARAT UNIVERSITY, AHMEDABAD

for the degree of

DOCTOR OF PHILOSOPHY

OCTOBER 1976

Physical Research Laboratory

Ahmedabad - 380009

India

043



B7605

D e d i c a t e d t o

My Parents

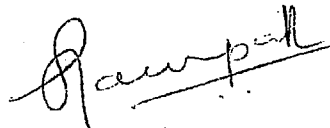
SARANGAN

and

VEDAVALLI

CERTIFICATE

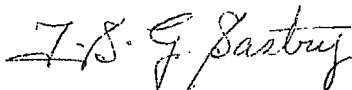
I hereby declare that the work presented in this dissertation is original and has not formed the basis for the award of any degree or diploma by any University or Institution.



S. SAMPATH

(Author)

Certified,



T.S.G. SASTRY

(Professor-in-charge)

October 20, 1976.

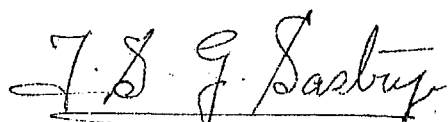
STATEMENT

This dissertation is based on the results from rocket-borne magnetic and electric field measurements made from Thumba Equatorial Rocket Launching Station, India. Magnetic field measurements were carried out using proton precession and Rb. vapour magnetometers. The electric field and its fluctuations were measured using the Langmuir double probe technique. The data from the in-situ measurements and the data from the ground magnetic observatories have been used to study the diurnal and day-to-day variability of the equatorial electrojet parameters, the effect of the depression of the main phase of a magnetic storm on the electrojet, the joule heating effect of the electrojet in increasing the electron temperature over that of the neutrals and the ac electric fields associated with the plasma instabilities in the electrojet region.

The author was closely associated with the fabrication, integration and pre-flight check outs of the rocket payloads and in setting up the ground Rb. magnetometer stations. He developed the necessary data reduction systems, to reduce the data from the rocket experiments. He has analysed the data and interpreted the results, under the guidance of Professor T.S.G. Sastry.

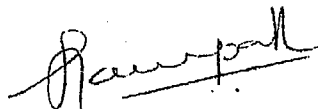
This thesis has been divided into 8 chapters. The first chapter is an introduction to the study of the equatorial electrojet and its effects. Chapter 2 deals with the rocket-borne instruments used by the author and the data reduction systems developed by him. The method of analysis of the rocket data and the various errors and uncertainties involved in the analysis are discussed in chapter 3. The diurnal and day-to-day variability of the electrojet parameters, as observed by rocket-borne magnetometers and their relation to the ground magnetic variations are discussed in chapter 4. The effect of the main phase of a magnetic storm on the electrojet is discussed in chapter 5. Chapter 6 deals with the joule heating of electrons by the electrojet currents and chapter 7 discusses the results concerning the electric field fluctuations associated with the plasma instabilities in the regions of the equatorial electrojet.

The important conclusions arrived at from the present study of the electrojet and its effects are summarised in chapter 8.


Prof. T.S.G. SASTRY

Physical Research Laboratory
Ahmedabad-380009
India

October 20, 1976.


S. SAMPATH
(Author)

ACKNOWLEDGEMENTS

The author wishes to express his sincere gratitude to Prof. T.S.G. Sastry, for his valuable guidance and constant encouragement throughout the work.

The inspiration and encouragement derived from Late Prof. Vikram A. Sarabhai, who initiated the project "Space Magnetometry" in our country, is acknowledged with a deep sense of respect and gratitude.

The author is thankful to Prof. Hirao of the Institute of Space and Aeronautical Sciences, University of Tokyo, Japan, Prof. Blamont and Dr. J. Sartiel of CNES, France and Dr. Burrows of Appleton Laboratory, UK for allowing him to use some of the data obtained during rocket-borne experiments conducted by them in collaboration with us.

The author is thankful to Prof. B.N. Bhargava, Director, Indian Institute of Geomagnetism for the ground observatory magnetic data and to Prof. S. Prakash of P.R.L. for the electron density profiles used in this thesis.

The rocket payloads were constructed as a team work, under the supervision of Prof. T.S.G. Sastry. The author expresses his thanks to his colleagues Mr. S.G. Tikekar and Mr. H.S. Mazumdar for the help in the construction and testing of the rocket payloads and in the design and

construction of the data reduction system. The author is also thankful to Mr.N.R. Shah and Mr.D.D. Damle for neat wiring of the payloads.

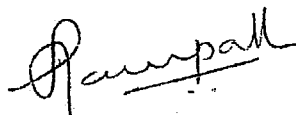
The cooperation and help rendered by the personnel of the Thumba Equatorial Rocket Launching Station, in making the rocket flights, a success, is highly appreciated. The author is particularly thankful to M/s. R. Arvamudan, V. Sudhakar and M.D. Bhaskar of TERLS, for their help at various stages of the rocket campaigns.

The author is thankful to Dr. M.R. Sivaraman, for many useful discussions, during the early stages of the work. The author is greatly grieved by the sudden and sad demise of his colleague Mr.M. Jayarama Rao, with whom he had many memorable discussions. The author is grateful to Prof. S.R. Govindarajan and Sri S. Srinivasan of D.G.V. College, Madras for their constant encouragement throughout his academic career.

The author is grateful to the Physical Research Laboratory, for providing excellent facilities for the research work. It is with pleasure, I acknowledge the help and understanding of the personnel of the Computer center, photography and documentation section and the workshop.

The computational assistance of Mrs. S.G. Bakre and the help rendered by Mr.C.S.R. Murthy in the data analysis are highly appreciated.

The author duly acknowledges the neat typing of the thesis done by Mr.K.S. Nair.

A handwritten signature in cursive script, appearing to read 'Sampath', written over a horizontal line.

S. SAMPATH

(Author)

TABLE OF CONTENTS

		Page No.
Chapter 1	<u>Introduction</u>	
1.1	The Equatorial Electrojet	1
1.2	Conductivities in the ionosphere	3
1.3	Investigation of the equatorial electrojet	6
1.3.1	Ground based techniques	6
1.3.2	In-situ techniques	7
1.4	Magnetic field variations	8
1.5	Quiet day variations	9
1.5.1	Ground based investigations	9
1.5.2	Day-to-day variability	14
1.5.3	In-situ measurements of the equatorial electrojet	17
1.6	Disturbance variations	22
1.7	Irregularities in the electrojet region	22
1.8	Joule heating of electrons by the electrojet currents	24
1.9	Statement of the problem	24
Chapter 2	<u>Instrumentation</u>	
2.1	Magnetic field measurements	28
2.1.1 ✓	The Proton Precession Magnetometer	
2.1.1.1	Principle	28
2.1.1.2	Payload design	31

2.1.1.3	Payload integration and performance	35
2.1.1.4	Data reduction,	37
2.1.2	The Rubidium Vapour Magnetometer	
2.1.2.1	Principle	38
2.1.2.2	Rb. magnetometer payload design	43
2.1.2.3	Integration and pre-launch operation of the payload	44
2.1.2.4	The data reduction system	46
2.1.3	Ground Magnetometer Stations - set up	49
2.2	Electric field Measurements in the Ionosphere	53
2.2.1	The Langmuir double probe	
2.2.1.1	Principle	54
2.2.1.2	Design of the experiment	55
2.2.1.3	The Data Reduction System	56

Chapter 3 Data Analysis

3.1	Determination of the profile of field intensity (F) versus the flight time (T)	60
3.2	The Trajectory determination	63
3.3	Derivation of the perturbation field ΔF	67
3.4	Evaluation of the theoretical field F_T	68
3.5	Derivation of the electrojet current density J	70
3.6	Errors and uncertainties in the measurement and data analysis	

3.6.1	Error in the measurement of F	72
3.6.2	Uncertainty in the trajectory determination	75
3.6.3	Uncertainty in the theoretical field F_T	77
3.6.4	Rocket precession effect due to payload field	77
Chapter 4	<u>Diurnal and day-to-day variability of the electrojet</u>	
4.1	Diurnal variation	81
4.1.1	Flight details	82
4.1.2	Flight results	83
4.1.3	Discussion of flight results	84
4.2	Day-to-day variability	87
4.2.1	Experimental details and results	88
4.2.2	Discussion of results	89
4.3	Prediction of vertical profile of current density on a quiet day	93
4.4	Relation between J, ΔH and H induced	98
4.4.1	The Model	99
4.4.2	Determination of width	100
4.4.3	Ground induced image of the electrojet	101
4.4.4	Evaluation of H due to the currents	102
4.4.5	Errors and uncertainties in the estimation of H_{int} and H_{ext}	104
4.5	Conclusions	106

Chapter 5	<u>Electrojet during the main phase of a magnetic storm</u>	
5.1	Introduction	109
5.2	Details of the experiment	111
5.3	Ground data	112
5.4	Discussion	113
5.5	Conclusions	117
Chapter 6	<u>Joule heating of electrons due to the electrojet currents</u>	
6.1	Introduction	118
6.2	Flight details and flight data	122
6.3	Discussion of the flight results	123
6.4	Conclusions	126
Chapter 7	<u>Electric field fluctuations in the electrojet</u>	
7.1	Introduction	127
7.2	Noon time experiments	
7.2.1	Flight details	133
7.2.2	Flight results	134
7.2.3	Discussion of flight results	141

7.3	The early morning experiment	
7.3.1	Flight details	143
7.3.2	Payload details and performance	143
7.3.3	The results	144
7.3.4	Discussion of results	146
7.4	Conclusions	148
Chapter 8	<u>Conclusions</u>	151

REFERENCES

1.1 The Equatorial Electrojet:

It is now well known, that the equatorial electrojet is a band of intense current, situated in the E region of the ionosphere above the dip equator. The current in the band flows eastwards during the daytime and in the night, current is small or negligible.

Abnormally large amplitudes of the diurnal variation of the horizontal component (H) of the earth's magnetic field, observed at Huancayo, Peru, near the dip equator, by Johnston and McNish (1937) led to the discovery of this phenomenon of "the equatorial electrojet". Egedal in 1948 analysed the data from a number of magnetic observatories operating at that time near the dip equator, and found that the solar quiet day variation $Sq(H)$ is a maximum at the dip equator and falls off on either side of the dip equator. Egedal suggested that this enhancement could be due to a varying current, flowing in a narrow region, over the dip equator. The abnormally large $Sq(H)$ observed at Huancayo, was later found to be a global phenomenon, by Chapman (1948), Pontier (1950), Gulate (1950), Giesecke (1951), Pramanik and Yegnanarayanan (1952), Pramanik and Hariharan (1953) and Madwar (1953). The narrow

layer of intense current, flowing over the dip equator, responsible for the observed large amplitudes of $Sq(H)$ was named, "the equatorial electrojet", by Chapman (1951).

Bartels and Johnston first reported in 1940, the enhancements in the lunar semi-diurnal variation of the geomagnetic field L , at Huancayo. Similar enhancements of L in the dip equatorial region were later found to be a global phenomenon associated with the electrojet by Onwumuchilli and Alexander (1959), Raja Rao (1962) and Rastogi (1964). These results indicated that the electrojet is under the influence of both the Sun and the Moon.

The cause for the enhancement of $Sq(H)$ at the dip equator was theoretically investigated by Hirono (1950, 1952), Maeda (1952, 1953), Baker and Martyn (1952, 1953) and many others. These investigators showed that the enhancement of the east-west conductivity in a narrow region over the dip equator is the cause of the equatorial electrojet. Cowling (1932) had suggested that if the flow of Hall currents is prevented by polarisation of the medium, then the effective conductivity is enhanced in the medium. This suggestion was applied to the equatorial ionosphere first by Hirono and followed by Maeda and Baker and Martyn. These workers showed that at the dip equator, where the magnetic field is purely horizontal, the Hall currents are prevented by polarisation

of the medium and this enhances the effective conductivity in the ionosphere over the dip equator. This enhanced conductivity is responsible for the flow of the equatorial electrojet currents. The present understanding of the formation of the equatorial electrojet, is illustrated schematically in Figure 1.1.

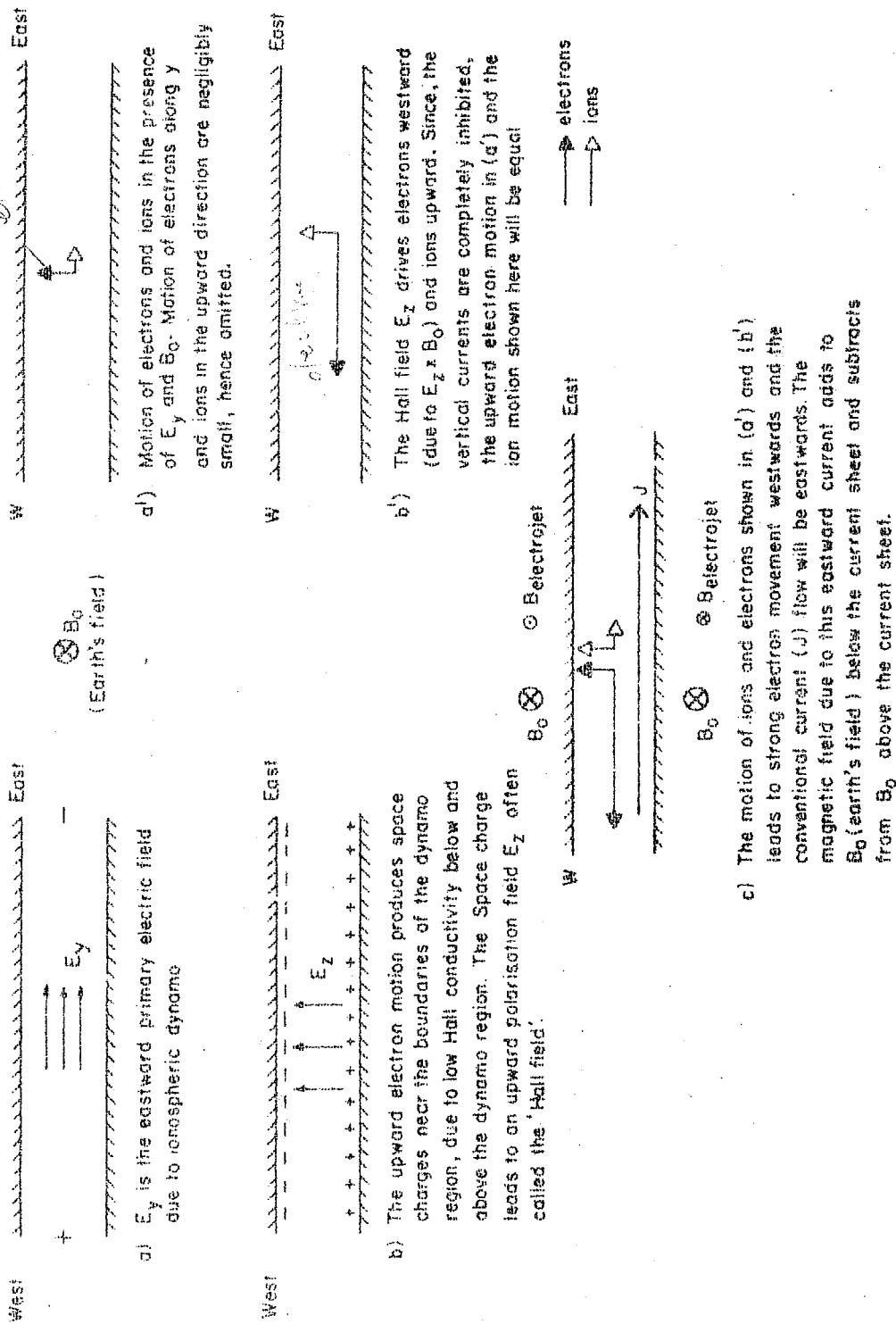
1.2 Conductivities in the ionosphere:

For the discussion and understanding of the diurnal and day-to-day variability of ionospheric currents and consequent magnetic field variations observed at the ground, it is important to understand the nature of ionospheric conductivities, their altitude distribution and time variations.

The conductivity in the ionosphere becomes anisotropic in the presence of magnetic field and the tensor conductivity can be written as,

$$\underline{\underline{T}} = \begin{pmatrix} \sigma_{xx} & \sigma_{xy} & \sigma_{xz} \\ \sigma_{yx} & \sigma_{yy} & \sigma_{yz} \\ \sigma_{zx} & \sigma_{zy} & \sigma_{zz} \end{pmatrix}$$

where the current density $\underline{J} = \underline{T} \cdot \underline{E}$, \underline{E} being the electric field. Under the consideration that, the stratification in the ionosphere restricts currents to flow primarily in



FORMATION OF THE EQUATORIAL ELECTROJET

FIG. 1.1. Schematics, illustrating the formation of the electrojet.

horizontal layers, the tensor conductivity reduces to,

$$\underline{\underline{T}} = \begin{pmatrix} \sigma_{xx} & \sigma_{xy} \\ -\sigma_{xy} & \sigma_{yy} \end{pmatrix}$$

where $\sigma_{yx} = -\sigma_{xy}$. The components of current density are then given by,

$$J_x = \sigma_{xx} E_x + \sigma_{xy} E_y$$

$$J_y = -\sigma_{xy} E_x + \sigma_{yy} E_y$$

When an electric field \underline{E} , is parallel to the magnetic field \underline{B} , the conductivity is called the direct conductivity or longitudinal conductivity and is denoted as σ_0 . This is independent of the strength of the magnetic field. When an electric field is perpendicular to the magnetic field, the conductivity is called the Pedersen conductivity, Pedersen (1927), and is denoted as σ_1 . In the case of crossed electric and magnetic fields, there will be a flow of current perpendicular to both the electric and magnetic fields and this current is called the Hall current. This has the direction of $\underline{B} \times \underline{E}$ and the conductivity that becomes operative in this case, is called the Hall conductivity, σ_2 . These conductivities are functions of the electron density, electron and ion gyro-frequencies and their collision frequencies with the neutrals.

Consider a coordinate system in which the x and y axes coincide with the magnetic south and east respectively and the z axis points vertically upwards. The magnetic field is in the **zx** plane and dips downwards with a dip angle I. In this case, the layer conductivities σ_{xx} , σ_{xy} and σ_{yy} can be expressed in terms of the primary conductivities σ_0 , σ_1 and σ_2 as

$$\sigma_{xx} = \sigma_0 \sigma_1 / P$$

$$\sigma_{xy} = \sigma_0 \sigma_2 \sin I / P$$

$$\sigma_{yy} = [\sigma_1 \sigma_0 \sin^2 I + (\sigma_1^2 + \sigma_2^2) \cos^2 I] / P$$

where $P = [\sigma_0 \sin^2 I + \sigma_1 \cos^2 I]$

At the dip equator, the magnetic inclination $I = 0$, therefore

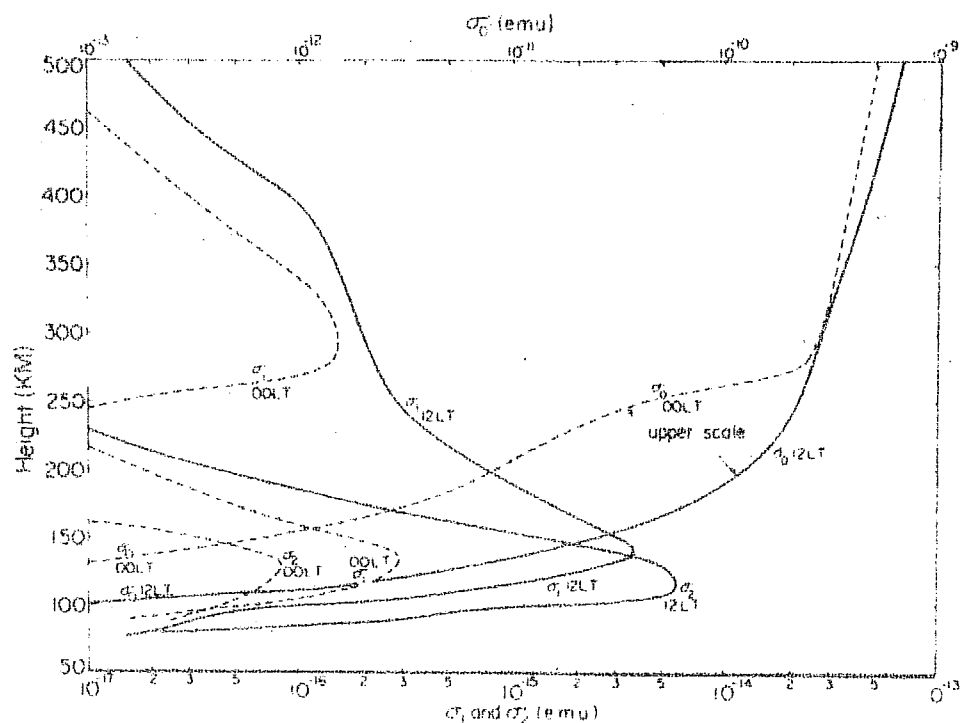
$$\sigma_{xx} = \sigma_0$$

$$\sigma_{xy} = 0$$

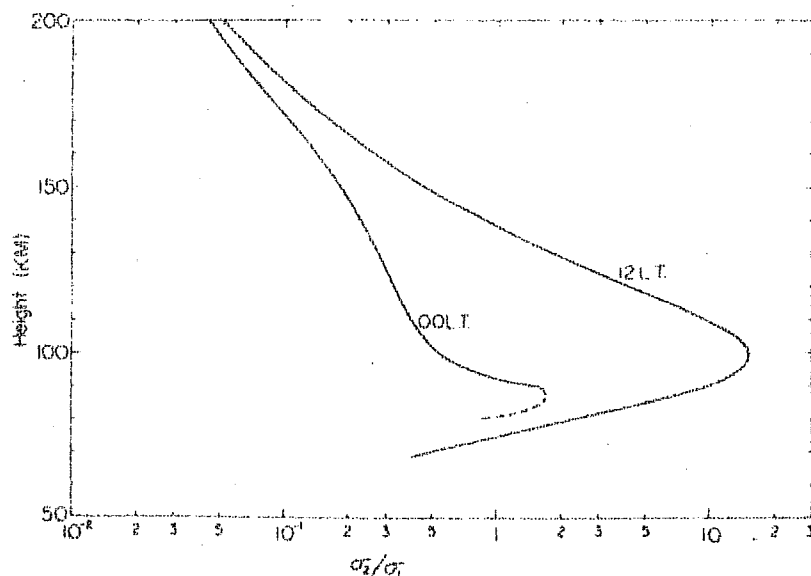
$$\sigma_{yy} = \sigma_1 + \frac{\sigma_2^2}{\sigma_1} = \sigma_3$$

σ_3 is called the cowling conductivity and it is higher than σ_1 , the Pedersen conductivity and σ_2 , the Hall conductivity. The cowling conductivity is responsible for the flow of the electrojet currents.

The conductivities σ_0 , σ_1 and σ_2 have been calculated as a function of altitude by various workers and notably by Maeda and Matsumoto (1962). The time variation of the vertical profiles of these conductivities, taken from Maeda and Matsumoto [Matsushita (1967)] is shown in Figure 1.2.



Height distributions of σ_0 , σ_1 , and σ_2 at 00 and 12 h Local Time (redrawn from Maeda and Matsumoto [1962]). Note that the abscissa for σ_0 is different from that for σ_1 and σ_2 .



Height distributions of σ_2/σ_1 [Maeda and Kato, 1966].

FIG. 1.2. Height distribution of conductivities, reproduced from, "Physics of Geomagnetic Phenomena", Edited by S. Matsushita and W.H. Campbell (1967), p 383.

The altitude profile of the ratio of σ_2/σ_1 is also shown in the figure. This shows that σ_2/σ_1 maximises around 100 km where σ_3 also maximises, and this region around 100 km, is the seat of the electrojet currents.

1.3 Investigation of the equatorial electrojet:

The equatorial electrojet (EEJ) causes a wide variety of interesting phenomena such as the magnetic field variations observed at the ground, the generation of plasma irregularities, the joule heating of electrons and the atmospheric motor effect in the F region. These phenomena have been studied using ground based and in-situ techniques.

1.3.1 Ground based techniques: Some of the important ground based techniques used for the study of the equatorial electrojet, involve the use of the magnetometers or the variometers in the observatories. These instruments record the magnetic field variations continuously. The construction and performance of these instruments have been discussed by Chapman and Bartels (1940) and Alldredge (1967).

The VHF back scatter radar gives information on the irregularity spectra, drift velocity of irregularities, winds and electron, neutral and ion temperatures. The use of back scatter radar in deducing these informations has been discussed by Cohen (1967) and Balsley (1973).

The HF ionosonde gives the electron density distribution in the ionosphere upto the F layer peak and the spaced-receiver technique gives information of the drift velocity of the irregularities in the ionosphere. The spaced receiver technique has been discussed by Mitra (1949). The ionosonde, a basic tool for the investigation of the ionosphere, has been discussed by many investigators of the ionosphere. A neat description is given by Davies (1966).

1.3.2 In-situ techniques: The in-situ techniques involve the use of rocket and satellite borne instruments. The rocket-borne magnetometers which are mainly the total field ones, of the proton precession and Rb. vapour types, give information concerning the vertical distribution of electrojet current density. The electron density distribution and its fluctuations are measured using a Langmuir probe. The Langmuir double probe detector which uses the potential difference method is used for detecting the electric field and its fluctuations or in other words the DC and AC electric fields. Electric fields are also measured in the twilight periods using Barium cloud releases. Winds in the atmosphere can be determined using sodium cloud releases in the twilight and lithium clouds in the day time. The conventional Langmuir probe used for the electron density measurement has been slightly modified to measure the electron temperatures in the

ionosphere reliably. The details of these techniques, their capabilities, limitations and achievements have been discussed by various workers. Special mention may be made of the excellent review articles on these subjects; for instance Ness (1970) on magnetometers, Mozer (1973) on electric field detectors and by Smith (1969) on Langmuir probes for the measurement of electron density and temperature.

1.4 Magnetic field variations:

The geomagnetic total field F observed at the ground at any time, can be written in general as,

$$F = (M + m) + (Sq + L) + (D + N)$$

where M is the earth's main field and m is its secular variation, both these are of internal origin. Sq and L are the solar and Lunar daily variations which are quiet day variations of earth's magnetic field. D is the disturbance variation which represents the variations due to magnetic storms and other disturbance effects. N represents all non-cyclic variations, which do not form part of other magnetic variations. The topics of interest here are the Sq , L and D . In other words the quiet day and disturbed day variations, especially in the equatorial electrojet region.

1.5 Quiet day variation:

The two important aspects of the quiet day geomagnetic variations are the diurnal variation and its day-to-day variability. In the region of the electrojet the basic cause of these variations have been investigated by studying the spatial and temporal variations of the parameters of the equatorial electrojet. The H, Z and D variations data from the ground based observatories enable us to study the variation of some of these parameters with latitude, longitude and time. The ground data can give the information regarding the electrojet parameters such as the strength of the electrojet as observed from the daily H range, the width of the electrojet and the nature of the variation of H and Z with latitude. Such data has been extensively used for the study of diurnal and day-to-day variability of geomagnetic field. The in-situ measurements give information regarding the electrojet parameters such as the strength of the electrojet (height integrated current density), the vertical extent of the current layer, thickness of the current layer and the altitude at which the electrojet current maximises, which cannot be ascertained by ground based measurements. Hence these two modes of studies are complementary to each other.

1.5.1 Ground based investigations: The results of the investigations concerning the electrojet parameters in the quiet

time, their spatial and temporal variation, the relationship between the electrojet and the mid-latitude Sq current systems have been summarised by Onwumuchilli (1967), Raja Rao (1972) and Kane (1976). Here, attention is drawn to some of the important findings concerning the electrojet, which are of particular relevance to this dissertation.

From the ground based measurements, it is known that the electrojet strength, as obtained from the H ranges ($H_{\max} - H_{\min}$) is maximum in the equinoxes. The nature of variation of the H ranges with latitude is symmetric with respect to the dip equator, according to Forbush and Casavarde (1967) while slight asymmetries have been found by Onwumuchilli (1959) and other workers. The Z variation shows a slight asymmetry with respect to the dip equator. Onwumuchilli (1959), Hutton (1967) and others have found that the degree of asymmetry changes with season and also during the course of a day. To explain the Z variation in the equatorial electrojet region, Knapp and Gettemy (1963) suggested an additional N-S flow superimposed on the conventional Sq current system. Van Sabben (1966) studied this north-south asymmetry in the Z variation and interpreted the asymmetry as the magnetic effect of an asymmetric current system in the ionosphere and the magnetosphere. In his model, he proposed that the ionospheric currents flow from south to north along the meridian and close through the magnetosphere. Such a current system

will produce non-zero D component magnetic variation. Van Sabben's hypothesis has been supported by Raja Rao and Joseph (1971). They computed the east-west toroidal magnetic field under the electrojet, using the mean hourly values of H and D and found that there are meridional currents flowing from south to north, as envisaged by Van Sabben.

Yacob and Khanna (1963) have shown that the half width of the electrojet in the Indian zone during the IGY to be 290 km. Yacob (1966) has found that the half width in all longitude zones in 1958 to be about 280 to 300 km and that it does not exhibit change with season significantly. The presence of day to day variability of the width of the electrojet and the extent of its variation on a day to day basis is an important factor to be considered in the evaluation of the effect of the EEJ at any station under the electrojet and also in checking the validity of EEJ models proposed from time to time.

Recently, the results from a study of data from a chain of ground magnetic stations set up at Chad in South Africa, have been discussed by Fambitakoye and Mayaud (1976a, b, c). They have interpreted the frequent presence of certain effects in the magnetic field variation data as due to neutral winds. These effects have been found to vary throughout the day and from one day to another. The results from these

analyses have been compared with Richmond's model [Richmond (1973)] by Fambitakoye et. al., (1976). In this, they point out that at midday, the westward winds above 120 km altitude tend to augment the current over the model values. The effect of westward winds above 120 km in contributing to the electrojet currents, was first suggested by Stening (1969).

Another important aspect of the geomagnetic field variation in the electrojet region, is its relationship with mid-latitude variation. Price and Wilkins (1963), Price and Stone (1964), Van Sabben (1964), Mayaud (1965), Matsushita and Maeda (1965), Hutton (1967) and others have suggested that the equatorial electrojet is a part of the mid latitude Sq current system, and that it results as a natural consequence of the convergence of the mid latitude current stream lines over the dip equator. If the electrojet is a part of the mid latitude Sq current system, then the daily ranges of the geomagnetic field variation, at different latitudes must correlate well with each other. Onwumuchilli (1967), Osborne (1968), Ogubuehi et. al., (1967) and others found poor correlation between the daily ranges of an equatorial station and a non-equatorial station. From this, they suggested that the electrojet may be an independant current system. If this is true, then it becomes necessary to find the region of return currents.

Onwumuchilli (1967) formulated an empirical model, which includes the possibility of the electrojet return currents a few degrees away from the electrojet axis. His analysis of data from the electrojet and nearby regions indicated the possibility of the presence of return currents around $\pm 5^\circ$ dip latitudes. The presence of return currents have been envisaged in the electrojet model of Sugiura and Poros (1967). One of the rocket magnetometer flights of Maynard (1967) detected a reverse current, north of the electrojet, which he has attributed to the return current.

Kane (1971) analysed the data from the Indian zone, and observed that the quiet day H ranges at the equatorial station Trivandrum and a low latitude station Alibag show poor correlation in all seasons. He also found that if corrections are applied for D_{st} effects and the position of the northern focus of the mid latitude Sq current system is normalised with respect to the dip equator, then the correlation improved very well. This improvement in correlation suggests that the electrojet is a part of the mid latitude Sq system.

Suzuki (1973) calculated the distribution of the possible return currents and concluded that the magnetic effect of any such return currents is negligible. A close chain of magnetic stations in the electrojet region may resolve the problem of return currents, as suggested by

various workers from time to time. So, the problem whether the electrojet is an independent current system or a part of the mid latitude Sq current system, remains open for investigation. Meanwhile theories for an understanding of the nature and behaviour of the EEJ have been worked out by some investigators treating EEJ as an independent current system (Sugiura and Cain 1966), Untiedt (1967), Sugiura and Poros (1969) and Richmond (1973) and by some others (Schieldge et. al., 1973) treating it as a natural consequence of the global dynamo generated Sq current system.

1.5.2 Day-to-day variability: The H ranges especially in the electrojet region exhibit large day-to-day variations even on magnetically quiet days. Several causes for this day-to-day variability have been suggested by various workers. Bartels and Johnston (1940), suggested that the day to day variability could be due to the influence of L variation. The modulation of the solar quiet day variation by the L variation can give rise to this day-to-day variability. But, the H ranges even on two consecutive days may vary by a factor of two, especially in the electrojet region. This shows that the lunar modulation cannot fully account for the large day-to-day variability in the electrojet region.

The day-to-day shifts in the Sq focus position was first reported by Hasegawa (1936, 60). He also pointed that the changes in the position of the focus could be due to changes in the wind patterns. Hutton (1967) suggested that such shifts may influence the H ranges in the electrojet region. Kane (1974) investigated the relation between the Sq focus position and the electrojet strength and found that, on an average, the electrojet strength was higher when the Sq focus shifted equatorwards.

A possible connection between the day-to-day variability of the H ranges in the electrojet region and the ionospheric dynamics was first suggested by Dunford (1967) and later by Akasofu et. al., (1969), McDoughall (1969) and Rush and Richmond (1973). Matsushita (1973), after a detailed study of this problem suggests that height varying winds, similar to (1,1) mode give rise to considerable effect on day-to-day variations in the near equatorial geomagnetic field. Obayashi and Maeda (1965) have drawn attention to the inevitable motor effect in the F region due to the atmospheric dynamo in the E region. They have pointed out the importance of combined study of E and F region dynamics for interpreting the observed changes in ionospheric parameters. Dunford (1967) using the Alouette I data, showed that the magnitude of the equatorial anomaly and the H ranges in the electrojet region, correlate well. Akasofu et. al., (1969) have suggested that this day-to-day variability may be due to changes in the electric field

of which the so called "bite-out phenomenon" may be an appropriate measure. They have supported this hypothesis with examples. Kane (1972) has found that the daily H ranges of quiet days did not correlate well with the solar radiation parameters, the 2800 MHz flux, or the X-ray flux ($44-60^{\circ}\text{A}$) or the sunspot number. He also found that the daily H ranges, correlated well with the noon-time E region drifts, the bite-out of foF2 and associated with the changes in h'F2. The results of these studies suggest an intimate relationship between the changes in E and F region winds (and consequently the electric fields) and the variation in the daily H ranges.

Sastry (1973) suggested that under certain special conditions, the formation or disappearance of a second current layer around 130 km, could be a cause for the day-to-day variability. The role played by the second current layer however has to be established by further in-situ experiments.

Another contributing factor to the day-to-day variability is the effect of the counter electrojet. Gouin (1962) noticed several instances where the daily variation of H at Addis Ababa (0.5°S dip latitude), reversed around midday hours, on magnetically quiet days. Since then, many workers have investigated this phenomenon. Gouin first attributed this reversal to the lunar effect. If this is true, the L effect must be felt at all longitudes. But Rao and Raja Rao (1963) found no evidence of a lunar effect on their records of

Trivandrum at the same period when it was observed at Addis Ababa. This shows that the effect is limited in longitudinal extent.

Oyinloye (1970) found that E_{s-q} disappeared during the counter electrojet periods. The ionospheric drift measurements of Rastogi (1973) indicate the reversal of the direction of flow of electrojet currents during certain times when counter electrojet is observed. Cain and Sweeney (1973) and Kane (1973) have interpreted the result from one of the passes of POGO, as due to the counter electrojet. However, there are no direct in-situ measurements concerning the nature of flow of ionospheric currents during the periods of counter electrojet. The counter electrojet effect when present modifies the diurnal variation and introduces changes in the diurnal amplitudes and hence contributes to the day-to-day variability in the H ranges in the electrojet region. The cause of the counter electrojet is not yet established.

Apart from these ionospheric effects, a magnetospheric contribution of 20% to the day-to-day variability has been suggested by Olson (1970).

1.5.3 In-situ measurements of the equatorial electrojet: Vestine et. al., (1947), in an effort to find substantiation for the dynamo theory, first suggested the use of rocket-borne magnetometers for the direct measurement of ionospheric

currents. The pioneering flights were conducted by Singer et. al., (1951) near the dip equator. These flights showed the presence of currents in the ionospheric E region. Cahill (1959) investigated the electrojet over the central Pacific and found a current layer around 100 km and another one near 120 km. This was the first time, in which the vertical distribution of the electrojet current density was obtained.

After this, a series of rocket-borne magnetometer experiments were conducted from Thumba, India, by Maynard et. al., (1965) and Maynard and Cahill (1965). During these experiments, the rockets reached an apogee of 160 km. and penetrated the current layer fully. A better calculation of the trajectory and the accurate measurement of magnetic fields during these experiments enabled them the determination of the vertical distribution of the electrojet current density to a higher degree of accuracy than their previous experiments. The results from the Indian flights showed that the electrojet is an intense current layer centered about 109 km altitude with a more diffuse tail extending upto 135 km. The occasional existence of a second current layer around 140-145 km was detected. A night time flight did not detect any appreciable currents that can produce a magnetic field of more than 10 nT.

In 1965, a series of rocket magnetometer flights were conducted from the sea vessel USNS Croatan, off the coast of

Peru. The results from these flights have been presented by Maynard (1967a). These experiments detected the electrojet with maximum current density at 109 km and extending upto 135 km. No reverse currents were found on the flight at the time of maximum negative effect of lunar current system. North of the dip equator, the low latitude Sq currents were found to have a two layered structure, one at 100 km and the other at 120 km altitude. A reverse current, which may be a partial return current from the electrojet was observed to the north of the electrojet at the altitude of 109 km, which corresponds to the altitude of the center of the electrojet.

The latitudinal profile of the electrojet strength was investigated by Davis et. al., (1967), with the data from rocket launches from the sea vessel USNS Croatan, in the south American zone. A normalised latitudinal cross-section of ionospheric current density was obtained using the data from peruvian ground stations and the results of nine rocket flights distributed between 140 km south and 1100 km north of the dip equator. The lower boundary of the current layer was found to be at 87 km altitude and the peak around 107 km directly above the measured location of the dip equator in the region. The half thickness of the current layer was about 12 km (102-114 km) and half width was around 300 km. The latitudinal profile of the current density near the dip equator obtained

by the above experiments indicated that the layer conductivities σ_{xx} and σ_{yy} affect the electrojet configuration and also that the electrojet distorts the magnetic field sufficiently to affect the layer conductivities. Using the observatory magnetic data and the rocket measurements, they found the ratio of $H_{\text{induced}}/H_{\text{ionospheric}} = 0.3$ for this region. A night time rocket flight on the dip equator, detected a weak westward electrojet. A noon time flight on the geographic equator, detected a current layer around 115 km altitude which could be the current layer of the mid latitude Sq system.

The equatorial electrojet has been studied using rocket-borne cesium magnetometers from Peru with the help of the sea vessel USNS Croatan by Shuman (1970). A set of four rocket flights were conducted in this campaign in 1965. A rocket magnetometer flight conducted at the dip equator during the maximum of electrojet effect, detected currents between 96 and 130 km with peak current density of 13.5 amp/km^2 at 106 km. A second flight conducted at the dip equator during the night time did not detect any ionospheric current effects within a resolution of about 5 nT. Two other flights were conducted in the region around $+5^\circ$ and -5° dip angles. The vertical distribution of current density observed at these places indicated a north-south asymmetry in the equatorial electrojet, fitting a wide current model to the north of the dip equator and a narrow one to the south.

Apart from the rocket borne magnetometer investigations, the electrojet has been studied using low altitude satellites such as the POGO and the Kosmos 321. The results of POGO measurements have been summarised by Cain and Sweeney (1973). On certain passes of POGO over the equator Cain and Sweeney have obtained clear records of the effect of the equatorial electrojet, while on some others they have obtained complex triple V structure magnetograms which have given rise to the speculation, that these structures are due to an eastward electrojet embedded in a regional westward current flow. The in-situ rocket measurements conducted so far however have not encountered any such system. The magnetic data from POGO passes over the equator have been correlated with the data from ground station, for different longitudinal zones by Kane, Yacob and Bhargawa, Gouin, Osborne and others. The results have been reviewed by Cain (1973).

The Kosmos 321 results have been presented by Dolginov (1972), in which he has given the magnetic signatures of the electrojet taken during two of its passes over Thumba. He has correlated the observed effect with ΔH at Trivandrum. The half width of the EEJ estimated by him from the Kosmos measurements is 205 km, which is quite small compared to 300 km calculated by Yacob and Khanna (1963) for this region. Smaller layer width needs a lower depth for the conducting

layer to bring the satellite observed effect of EEJ into agreement with ground measurements. Dolginov estimates the depth of the conducting layer as 125 km, which again appears to be too low for this region.

1.6 Disturbance Variations:

Our knowledge of the enhancements of the disturbance effects in the electrojet region comes mostly from ground based studies. The results have been summarised by Bhargava (1969). The effects in the electrojet region, of extra terrestrial origin, have been reviewed by Obayashi (1969). The solar flare effect (sfe) on the geomagnetic field, the geomagnetic impulses and DP2 associated magnetic field variations are some of the important effects prominently recorded at the electrojet stations. The enhancement of the SSC and the initial phase of the magnetic storm in the electrojet region have been studied by Farraro and Unthank (1951), Sugiura (1953), Yamura (1954), Chapman and Raja Rao (1965), Nishida et. al., (1966) and others. The only result available from in-situ measurements of the effect of the magnetic storm on the EEJ, forms the subject matter of Ch. 5 of this dissertation.

1.7 Irregularities in the electrojet region:

Extensive studies of the irregularities in the electrojet region have been carried out using the ground based VHF

back scatter radar at Jicamarca, Peru. The small scale type I irregularities, identified by Cohen and Balsley, are produced by two stream instability and the type II by the crossed field or gradient drift instability. The results of the study of these electrojet associated irregularities have been summarised by Cohen (1967). The electron density fluctuations associated with the plasma instabilities in the EEJ have been investigated using rocket borne Langmuir probes from Thumba by Satyaprakash et. al., (1973). The important conclusions of the study of the irregularities using rocket borne Langmuir probes and the back scatter radar have been reviewed in Chapter 7 of this thesis.

The first attempt to detect the electric field fluctuations associated with the plasma instabilities in the electrojet region, was undertaken at Thumba in 1972. The experiments were repeated in 1973 and 1975. AC electric field, electrojet current density, electron density and its fluctuations were measured on near simultaneous basis, during the experiments of 1972 and 1973. Simultaneous measurements of AC electric field, electron density and its fluctuations were done in 1975. The results from these experiments, concerning the AC electric field and the electrojet current density, are presented in Chapter 7 of this dissertation.

1.8 Joule heating of electrons by the electrojet currents:

The rate of energy input by the solar EUV radiation around 100 km is of the order of 10^{-7} erg/cc/sec. Kato (1963) suggested that the rate of heat input by the electrojet currents is of the order of 10^{-9} to 10^{-8} erg/cc/sec and hence they can preferentially heat the electrons such that the kinetic temperature of electrons will be increased over that of neutrals. This is investigated experimentally for the first time, using simultaneous measurements of electrojet current and electron temperature from Thumba. The result of this study is presented in Chapter 6.

1.9 Statement of the Problem:

As can be seen from the above description, the in-situ investigations carried out so far, for the study of the EEJ, have been oriented to the study of vertical distribution of electrojet current density, the strength of the current in the jet, the altitude at which current maximises, the latitudinal distribution of current density and the night time currents in the Jet region. The results available are mostly from Thumba (India) and Peru (USNS Croatan). Using the data from these investigations, attempts have been made to reconcile the rocket measurements of current density with that estimated from the magnetic variation observed at the ground. The data has also been used for verifying the electrojet models proposed from time to time.

As stated earlier in this chapter both the ground based investigations and the rocket investigations have advantages of their own, hence these two modes of investigations are complementary to each other. Only a combined ground and in-situ study can solve the problems associated with electrojet and its effects. With this in mind, several experiments were planned and carried out during the period 1966-1976, for an understanding of the phenomenon of EEJ and its effects. Using the data from the above experiments, the following problems are studied:

1. The nature of the diurnal and day-to-day variability of the electrojet parameters with a view to find the reason for the diurnal and day-to-day variability of H variation observed at the ground,
2. Using a simple model, whether it is possible to reconcile the rocket measured EEJ intensity with that estimated from ground based observations?
3. On magnetically quiet days, given the magnetogram from a station under the EEJ, is it possible to predict the vertical distribution of current density in the Jet at any time of the day?
4. What is the effect of the main phase depression of a magnetic storm on the electrojet?

5. ✓ Can the joule heating of electrons measured by an in-situ probe account for the theoretically estimated joule heating effect?
6. Does the stabilisation of plasma instabilities in the electrojet, on high jet days, modify the current distribution in the Jet?
7. Can the electric field fluctuations associated with the plasma instabilities in the electrojet region be identified? What are the spectral characteristics of these fluctuations?

The data for the above study has been derived from rocket-borne experiments conducted from Thumba, the details of which have been summarised in Table 1.1. The results from the above studies have been presented in chapters four, five, six and seven. In chapter eight the conclusions of the study have been summarised.

r. Flight Date o. No.	Time IST	Rocket Type	Payload	Scientific Objective	Discussed in
20.06	29.8.68 1108	Nike-Apache	Proton	Diurnal Variation	Chapter-4
20.07	29.8.68 1415	Nike-Apache	Proton	of the equatorial	
20.08	29.8.68 2300	Nike-Apache	Proton	electrojet.	
20.09	27.3.70 1048	Nike-Apache	Proton	Day-to-day variability	Chapter-4
20.11	25.4.71 1130	Nike-Apache	Proton + Te probe	Day-to-day variability and	Chapter-4
20.12	30.4.71 1138	Nike-Apache	Proton	Joule Heating (20.11)	Chapter-6
20.13 (P110)	2.2.72 1100	Petrel	Rubidium	Day-to-day variability	Chapter-4
20.14 (P59)	5.2.72 1130	Petrel	Rubidium		
20.15 (P60)	13.2.72 1825	Petrel	Rubidium	Electrojet during a magnetic storm	Chapter-5
20.16	13.10.72 1259	Nike-Apache	Proton	Electrojet current	Chapter-7
05.17	13.10.72 1225	Centaure	E-field probe	and plasma instabilities	
20.17	3.3.73 1224	Nike-Apache	Proton	Electrojet current and	Chapter-7
05.19	3.3.73 1135	Centaure	E-field probe	plasma instabilities	
P158	9.2.75 0559	Petrel	E-field probe	Plasma instabilities	Chapter-7

ABLE 1.1. Details of the rocket experiments conducted from Thumba, India for the study of the equatorial electrojet and its effects.

In this chapter, the instruments used for the investigation of the equatorial electrojet have been described. The chapter is broadly divided into two sections; the first one deals with the instruments used for the magnetic field measurements and the second deals with the ones used for electric field measurements.

The magnetic field measurements were carried out using Proton and Rubidium magnetometers. The basic principles of operation of these instruments and the problems involved in getting the best performance from these instruments when used for in-situ measurements, have been discussed. A short description of the system used for reduction of data from the rocket magnetometers has also been given.

At the end of section 1, the experimental set up of a typical ground magnetometer station, which was operated as a ground support for the rocket launchings in 1972, is described.

The section two deals with the techniques of electric field measurements in the ionosphere. The Langmuir double probe technique, which is particularly suitable for the study of electric field fluctuations, is described in detail.

This section also includes the description of a data reduction system developed for reducing the electric field data from the flight.

2.1 Magnetic Field Measurements

2.1.1 The Proton Precession Magnetometer:

2.1.1.1 Principle:

If a hydrogenous liquid sample, like water, or kerosene is subjected to a strong external magnetic field, all the protons in the sample, will align their spin axes with this external magnetic field. Now the sample is said to be polarised. The applied external field is called the polarising field B_p . If the polarising field is suddenly removed, all the protons in the sample will tend to align their spin axes with the ambient earth's field B . In doing so, they will precess slowly around the earth's field till they realign themselves with the ambient field. If a suitable pick up coil is used around the sample, the precessing protons would induce in this pick up coil an voltage whose frequency is equal to their precession frequency. By measuring the frequency of the signal induced, the scalar magnitude of the earth's field can be obtained from the Larmor relation,

$$2\pi f = \gamma_p B$$

... (1)

where f is the precession frequency and γ_p is the gyro-magnetic ratio of the protons. For protons in water, $\gamma_p = (2.67513 \pm 0.0002) \times 10^8$ radians/sec. tesla.

In practice, the same coil which is used for producing the polarising field is also used to pick up the signal. The sample is enclosed within a solenoid and this solenoidal coil is switched alternately between a polarising supply and a high gain amplifier. The signal voltage induced in the pick up coil is given by

$$V = 4\pi K N A \chi B_p B \gamma_p \sin^2 \theta \cdot \sin(\gamma_p B t) \cdot \exp[-t/T_2^2] \quad \dots (2)$$

where K = filling factor, N = number of turns, A = area of cross section of the sample, χ = paramagnetic susceptibility of the protons in the sample, t = time in seconds and θ is the angle between the polarising field and the ambient field.

It can be seen from the above equation, that there will be no signal when B_p is parallel to the earth's field ($\theta = 0^\circ$) and the signal is maximum when $\theta = 90^\circ$. The equation also shows that the signal is a sinusoid whose amplitude decays exponentially with a time constant T_2 . Water and Kerosene have large decay times and therefore are suitable liquids for sensor construction.

In order to get good signal from Proton magnetometer, it is necessary to take a few precautions. The polarising field B_p must be stronger than the earth's field B , so that the protons in the sample essentially see B_p and align with it. Also, the polarising field must be maintained for a time greater than T_1 , the thermal relaxation time, to make sure that all the protons will completely align themselves with the polarising field. The polarisation field must then be removed in a time shorter than the spin relaxation time T_2 , so that the protons precess freely under the ambient magnetic field without undergoing quick adiabatic decay. Another important factor is the magnetic field gradient within the sample. In the presence of such a gradient, protons at different parts of the liquid precess with different frequencies. Because of this incoherence in precession no measurable signal will develop across the pick-up coil. In rocket payloads, to avoid such a gradient, the sensor is mounted well away from the main body of electronics and a fibre-glass nose cone is used instead of a steel nose cone.

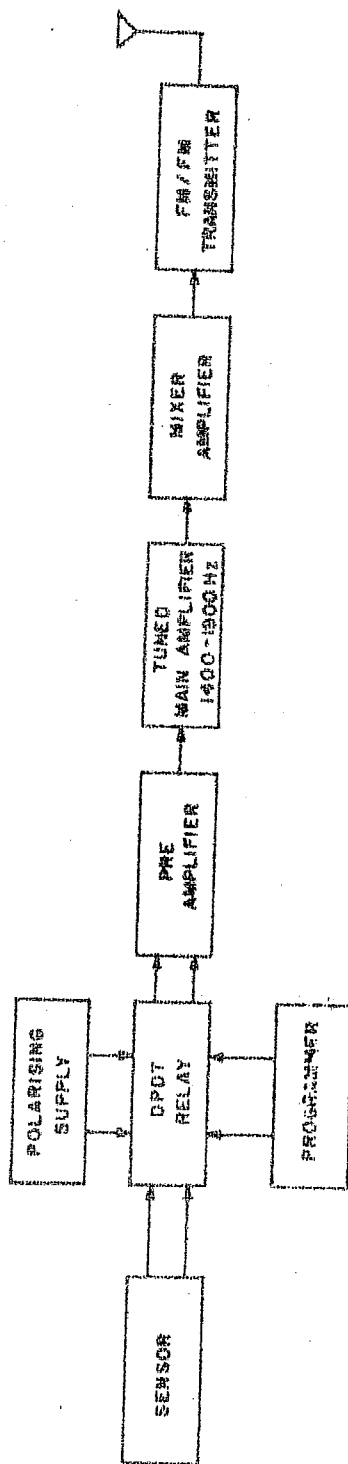
Packard and Varian (1953), Waters (1955), Waters and Francis (1958) and many others have instrumented proton magnetometers for ground based measurements. A miniaturised version of the ground based system has been adopted for the use in rockets with certain modifications to suit the rocket

environment and the requirements of particular measurement. The design, construction and performance of such magnetometers have been discussed by Cahill and Van Allen (1956), Sastry (1964) and Maynard (1967b).

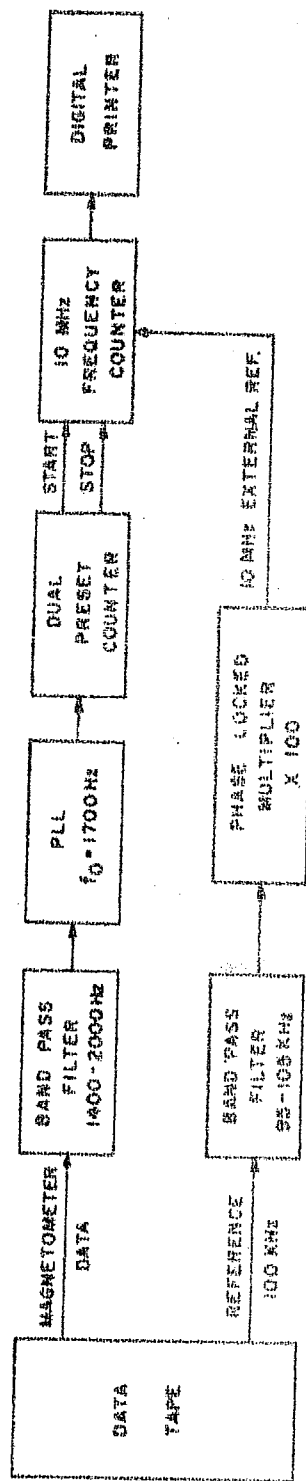
2.1.1.2 Payload design:

The block diagram of the proton magnetometer payload and a picture of the completed units are shown in Fig. 2.1a and Fig. 2.2 respectively. The magnetometer consists of a sensing element, a DPDT relay controlled by a programmer, a polarising supply, a pre-amplifier and a tuned main amplifier. The output of the main amplifier modulates an FM/FM transmitter through a mixer amplifier and this is telemetered to the ground.

The sensing element: A rigid fibre-glass bottle of 9.5 cms length and 6.5 cms diameter is filled with well filtered kerosene and then sealed. A solenoidal coil of 700 turns of # 16 SWG super enamelled copper wire is wound over the sample in multilayers. This system is carefully shielded from electrical noise pick up from the environment using a thin, printed copper clad fibreglass board. The sensor thus prepared is rigidly mounted on an ebonite pedestal and potted with a high density eccofoam. The sensor is then enclosed in a fibreglass gaurd to protect the potted sensor



(a) BLOCK DIAGRAM OF PROTON PRECESSION MAGNETOMETER PAYLOAD



(b) BLOCK DIAGRAM OF DATA REDUCTION SYSTEM FOR PROTON MAGNETOMETER

FIG. 2.1. Block diagram of proton magnetometer payload and data reduction system.

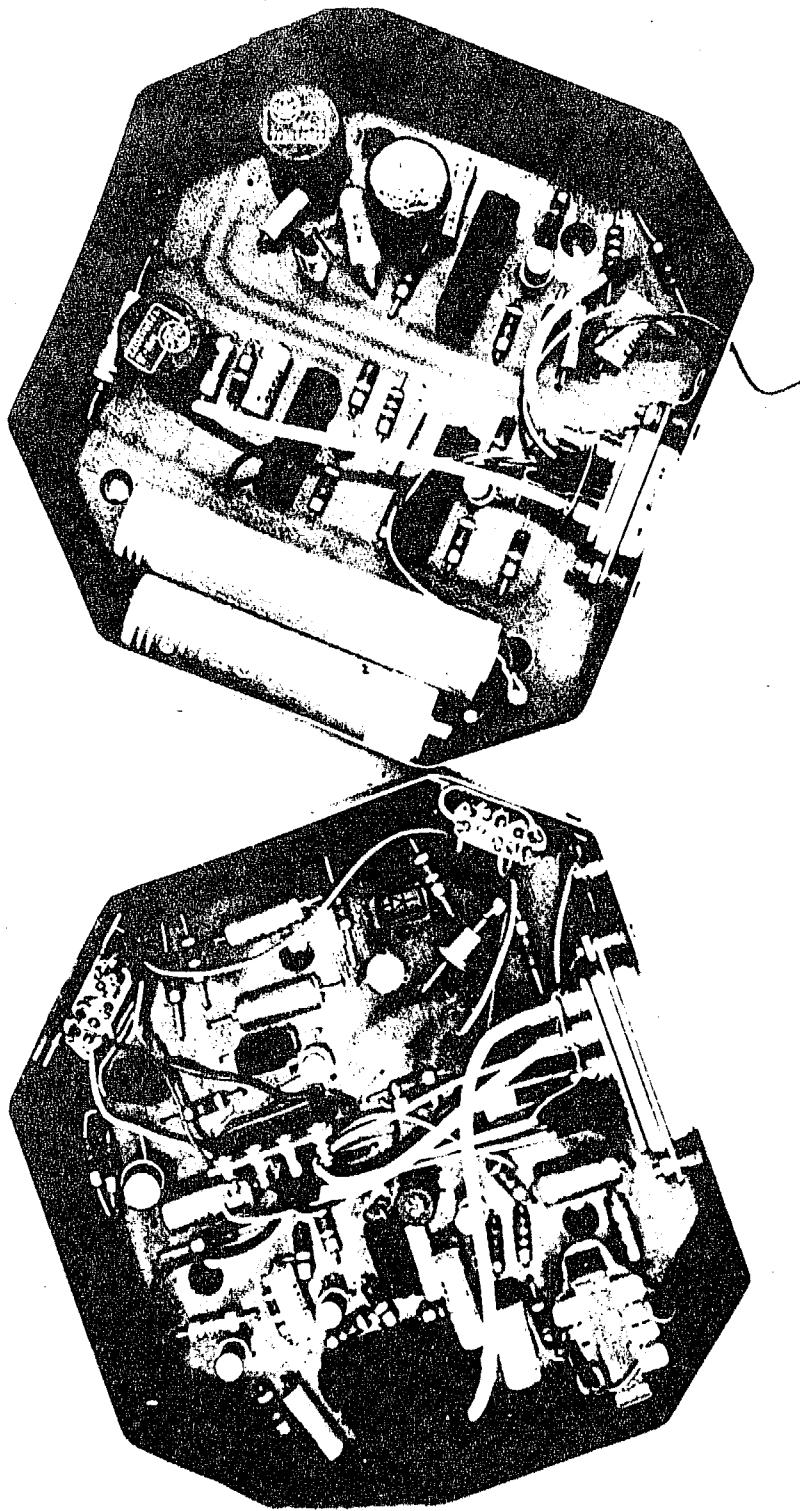


Fig. 2.2

FIGURE CAPTION

- FIG. 2.2. Completed units of the pre-amplifier and the main amplifier of a proton precession magnetometer rocket payload, showing the details of the component layout on a printed circuit-board. Non-magnetic cannon connectors are used. The box with battery cells in it is the main amplifier.
- FIG. 2.3. A completely integrated Nike-Apache payload of proton precession magnetometer and Langmuir probe. The proton magnetometer sensor is mounted on the top-most circular deck, well away from the main body of electronics. The transmitter and the DC/DC converter are enclosed in the mating section at the bottom. The turnstile antennas may be seen coming out of the mating section.
- The fiber glass nose cone with the Langmuir probe sensor at the tip is seen to the right of the integrated payload and the payload control box is seen at the extreme left.

from accidental damage. Only non-magnetic materials, free from magnetic contamination were used for the construction of the sensor. A current of three amperes flowing through the solenoid will produce a polarising field B_p of nearly 400 gauss along the axis of the solenoid which is sufficient to align the protons in the sample with B_p . The polarising current from the batteries to the sensor must be passed through a twisted pair of wires to suppress the effect of magnetic field generated due to 3 amp DC current flow to the sensor.

The programmer: The programmer controls a DPDT relay which switches the sensor alternately between the polarising supply and the pre-amplifier. In rocket payloads, the polarising supply consists of a stack of HR-3 silver cells which can supply a current of 3 amperes at 12V. The programming oscillator which controls the DPDT relay is a symmetric astable multivibrator whose switching period is adjusted to 0.8 second. At the start of the polarising period it switches the relay to connect the sensor to the polarising supply for a duration of 0.8 second and at the end of this period it switches the relay to disconnect the polarising supply from the sensor and connects the sensor to the pre-amplifier for another 0.8 second which is the read period. To protect the input of the pre-amplifier from damage due to the inductive surge produced when the sensor coil is switched off from the

polarising source, a 10 millisecond delay is introduced by means of a relay before connecting the sensor to the pre-amplifier. The surge is also clipped at the input of the pre-amplifier to a low level so that it may not overload the input of the pre-amplifier. During polarisation, when the pre-amplifier is disconnected from coil, the input of the high gain amplifier becomes open. This sets the amplifier system into oscillations. To prevent this a resistance of 100 ohms is shunted across the pre-amplifier input during the polarisation period.

The pre-amplifier: The Larmor frequency signal from the sensor has an amplitude of 3 to 4 μ Volts. Since the sensor coil is also an efficient antenna, it picks up the environmental noise in spite of shielding. The problem is to pick up the low signal against high background noise. In rocket magnetometers, the range of magnetic field to be measured is quite wide, therefore the input of the pre-amplifier cannot be sharply tuned to improve the signal to noise ratio. Taking these problems into consideration a high sensitivity, broad band, low noise amplifier that can rise the micro-volt signal to the level of a millivolt was designed. For maximum signal transfer from the sensor to the pre-amplifier the input impedance of the pre-amplifier was matched to the sensor coil impedance by means of a matching transformer. The output of

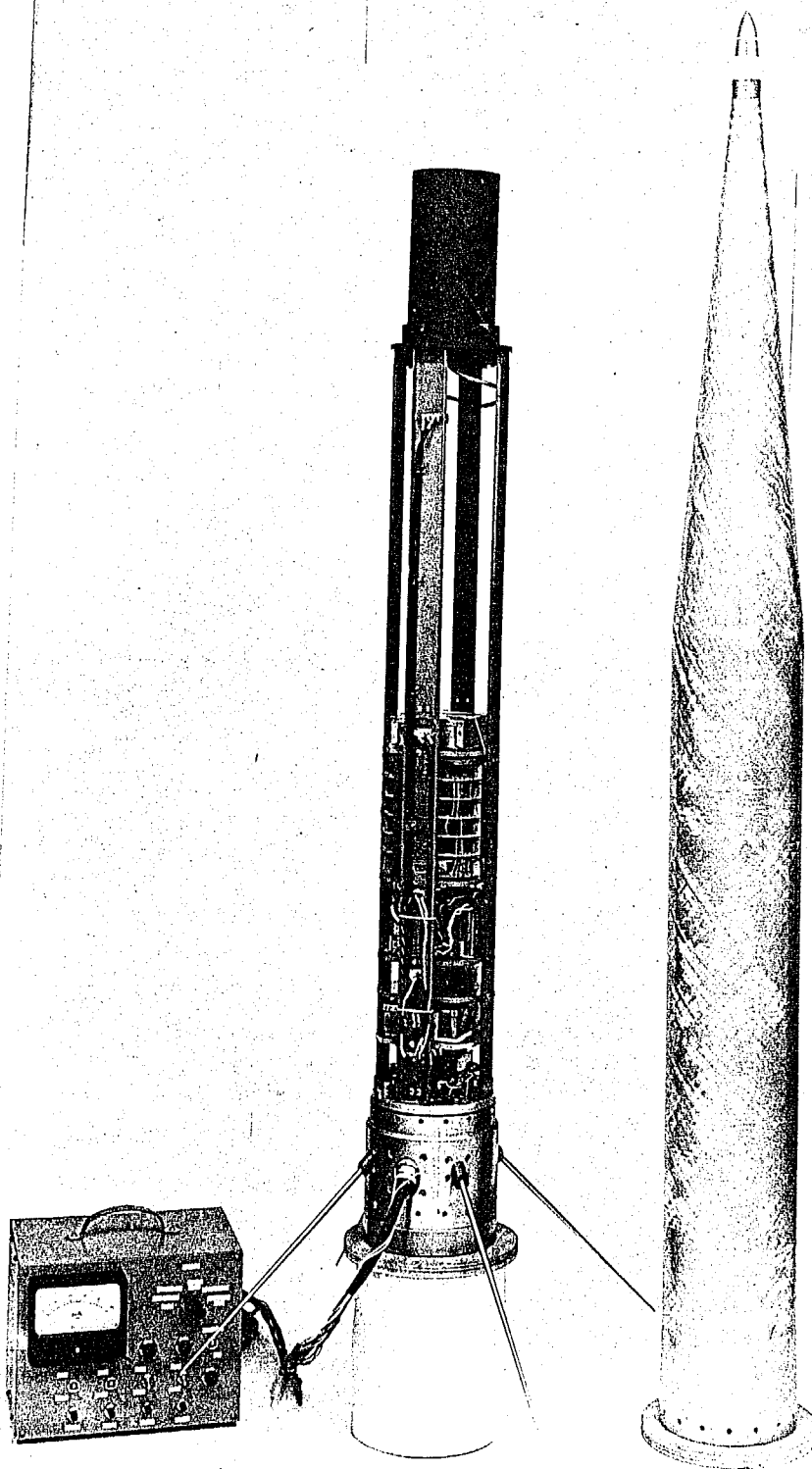


Fig. 2.3

2.1.1.3 Payload integration and performance:

The magnetometer sensor is mounted on the topmost deck with its axis aligned with the spin axis of the rocket. The programmer-preamplifier assembly and the main amplifier are integrated with other experiments and mounted in the lower half of the nose cone, as far away from the sensor as possible. The aluminium base at the bottom (Fig. 2.3) houses the turnstile antenna harness, the telemetry transmitter and its DC/DC converter power supply. The nose cone, the decks and the rack are made from fibreglass. All the proton magnetometers flown so far from Thumba used Nike Apache rockets only. The Nike booster is magnetic but the apache is non-magnetic. The Nike falls off a few seconds after launch leaving the payload on the non-magnetic second stage, the Apache.

The rockets are launched at wind corrected launch setting of 85° elevation and 270° azimuth. Since the magnetic field is horizontal and runs N-S over Thumba, the sensor does not enter into zones of poor signal during the flight when launched at 270° azimuth.

No serious problems were encountered either during the pre-flight checking after the integration or during the actual flight. In one of the payloads the magnetometer started oscillating as soon as the telemetry transmitter was switched on. The trouble was traced to the DC/DC

converter supplying power to the transmitter. This DC/DC converter was operating on a frequency which was within the pass band of the magnetometer amplifier. The problem was solved by replacing it by another converter operating at 4 KHz. It was also found necessary to suppress the ripple in the DC/DC converter output to a few mV to prevent the pick up of this noise by the magnetometer sensor.

It is necessary to take some precautions in selecting the programming relay. In first few experiments SIGMA (33RI490FGSL) relays were used, which have low contact resistance and high current rating for the contacts. But in one of the flights (FL.20.10) this relay failed after the second stage ignition. Thereafter the sigma relays were replaced by SC11DB relays which can withstand higher shock levels. These relays worked without failure but the S to N ratio slightly deteriorated, probably due to their higher contact resistance.

The proton magnetometer payloads instrumented for the investigation of the equatorial electrojet by Sastry and his colleagues have proved to be highly dependable. So far twenty of these magnetometers have been flown from Thumba. Except for the one in which the programming relay failed after the Apache ignition, all others have given good data on ascent as well as on descent.

2.1.1.4 Data reduction:

The data reduction system is shown in Fig. 2.1b. The magnetometer signal is recorded on the tape along with station time code and a reference frequency of 100 KHz from a frequency standard. The magnetometer data from the tape is fed to a band pass filter of pass band 1400 to 1900 Hz, which passes on the magnetometer signal to a phase lock loop (PLL). This PLL has a free running frequency of 1700 Hz and locks in the range of 1400 to 2000 Hz. The output of the PLL goes to a dual preset counter which generates the set and reset pulses for a 10 MHz gated counter. The set pulse is generated after about 100 milliseconds of the appearance of the magnetometer signal. The reset pulse is generated after counting 800 cycles of the precession frequency. The set and reset pulses operate the 10 MHz gated counter whose time base is derived from the 100 KHz standard reference recorded on the tape. The 10 MHz counter operates in the time interval mode and actuates a printer which prints out the time taken for 800 cycles of the precession frequency along with the time at which the sampling is made. The data tape is run several times to make sure of the consistency and stability of the data reduction system.

A sample telemetry chart record of the magnetometer signal taken during the flight time is shown in Fig. 2.4.

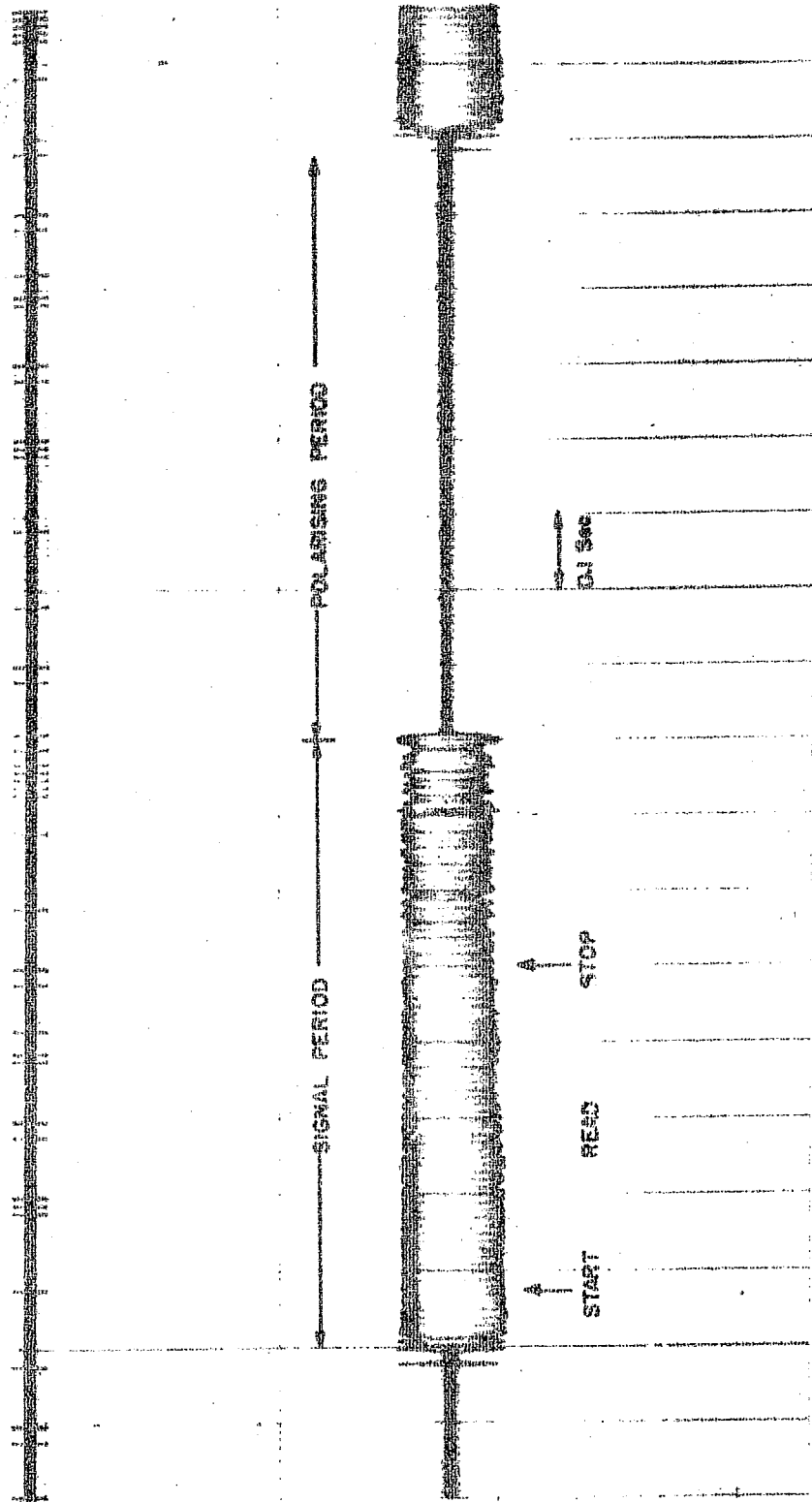


FIG. 2.4. A sample telemetry chart record of the signal from a proton precession magnetometer taken during a flight. The signal period and the polarising periods are shown. The operation of the dual preset counter during the data reduction is also indicated. The signal to noise ratio of the data during the sampling period is around 6 to 8.

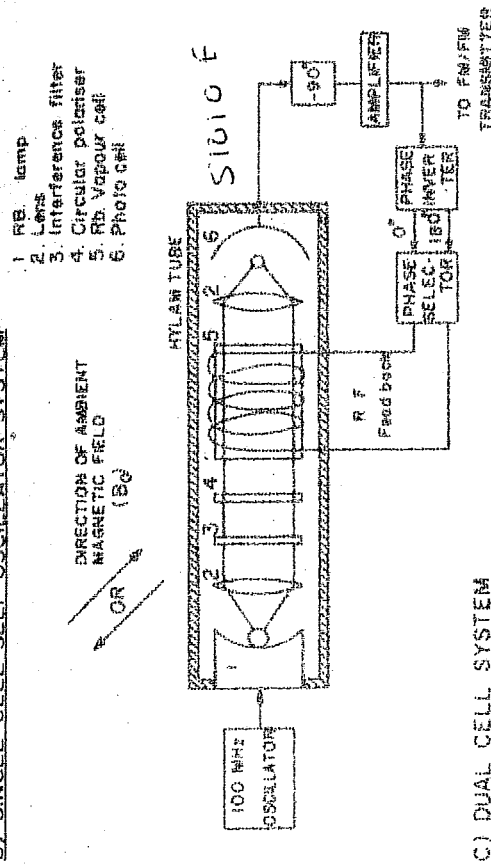
The recorded signal levels during the polarisation and read periods give an idea of the signal to noise ratio obtained, which is about 6 to 8 in this case.

2.1.2 The Rubidium Vapour Magnetometer

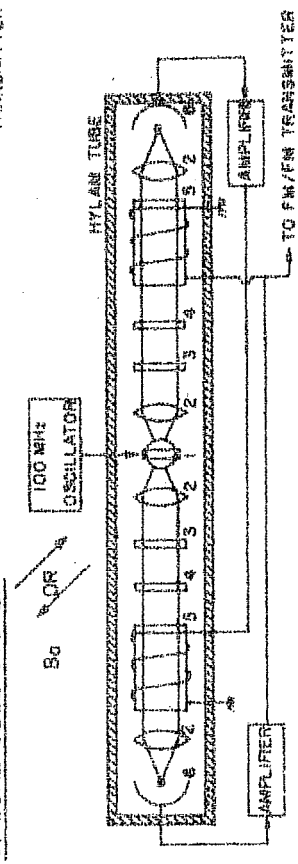
2.1.2.1 Principle:

The functioning of the Rb. magnetometer is based on the principle of optical pumping and light monitoring. This process involves the interaction of the magnetic moment and the angular momentum of the valance electron of Rubidium with the ambient magnetic field. Fig. 2.5a illustrates the energy levels of the single valance electron of Rubidium. In the presence of the earth's magnetic field, the energy levels are split into various sub-levels due to the Zeeman effect. The separation between these sub-levels is dependant on the total intensity of the ambient field. Dehmelt (1957) developed the technique of optical pumping and light monitoring to detect this proportional splitting which resulted in a practical, sensitive and accurate magnetometer.

Fig. 2.5b shows the block diagram of a typical Rb. magnetometer. The source of pumping light is a Rb. lamp which is excited by a 100 MHz, 2 watts power oscillator. The light from the electrodeless discharge in the lamp is focused on to an interference filter which cuts out the



C) DUAL CELL SYSTEM



RB. MAGNETOMETER PAYLOAD

FIG. 2.5. a) Energy level diagram of Rb^{85} , showing various energy levels associated with the single valence electron of Rb . Splitting of energy levels due to Zeeman effect, into various m sub-levels, whose separations are a function of the ambient magnetic field is illustrated in the figure. b) Block diagram of the single cell self-oscillating Rb . magnetometer payload. The details of the components of the sensor are shown. c) Block diagram of the dual cell Rb . magnetometer payload, showing the details of the sensor.

7800Å D_2 line of Rubidium and allows only the 7948Å D_1 line to pass through. This light is then polarised by means of a circular polariser. The polarised light illuminates the Rb. vapour cell in which pumping takes place due to the absorption of energy by the Rb. atoms from the polarised pumping beam. The output of the cell is focused on to a photocell, and the photocell output is amplified and monitored.

The pumping process that takes place inside the cell is briefly described here. The valence electrons of Rb. in the cell absorb energy from the pumping beam and go to the first excited state $2P_{1/2}$ from the ground state $2S_{1/2}$. Fig. 2.5a. As the light is circularly polarised, the transition from the ground state to the first excited state is also accompanied by a change in the magnetic quantum number $m = \pm 1$. The change $m = +1$ or -1 is decided by the sense of polarisation. Here we consider for simplicity that the light is right circularly polarised for which m can change by $+1$ only. The electrons in the excited state $2P_{1/2}$ fall back to the ground state either by radiationless relaxation or spontaneous emission. This kind of transition from the $2S_{1/2}$ state $2P_{1/2}$ state and back is repeated until all the electrons get preferentially populated in the $m = +3$ sub-level in the ground state. Since there is no m level above $m = +3$ in the $2P_{1/2}$ state, transition from $m+3$ sub-level in the $2S_{1/2}$ state

is not possible. The atoms are therefore trapped in this state. Now, no more absorption of pumping light is possible and the vapour is said to have pumped into this state. Since there is no absorption of the incoming light, the cell becomes transparent. To make the pumping process continuous, the atoms have to be redistributed in the ground state. The application of a weak alternating magnetic field perpendicular to the ambient field, varying at the Larmor frequency will redistribute the atoms to all their sub-levels. Now, the atoms will start absorbing the energy again from the pumping beam.

During the pumping process, the transparency of the cell is decreased by as much as 20% as monitored by the output of the photocell. The light transmitted by the gas cell at right angles to the pumping beam is intensity modulated at the Larmor frequency. If this is amplified, phase corrected and fed back to the gas cell, the system will self-oscillate at the Larmor frequency. A measure of this frequency will give the total intensity of the ambient magnetic field.

Some of the important features of the self-oscillator system are given below:

It gives a continuous measurement of the total field.

The signal to noise ratio of this system depends on $\sin 2\theta$, where θ is the angle between the ambient magnetic field direction and the optic axis of the system. When $\theta = 45^\circ$, the S/N is maximum.

The variation of the Larmor frequency with magnetic field intensity is not as straight forward as in the case of the proton magnetometer. At values near the earth's field, the Zeeman effect becomes anomalous, and the m sub-levels are not equispaced. The first order dependance of Larmor frequency on magnetic field is given by

$$f = 4.66737 \text{ nT/Hz for Rb}^{85}$$

$$f = 6.99632 \text{ nT/Hz for Rb}^{87}$$

The exact transition frequencies between various m sub-levels can be calculated using the Breit-Rabi formula as given by Farthing & Folz (1967).

A serious disadvantage of the self-oscillator system is the heading error. When the orientation of the optic axis of the system relative to the ambient magnetic field direction is changed, the Larmor frequency also changes. The maximum difference in the Larmor frequency observed in one full

rotation of the sensor with respect to the ambient field direction is called the heading error. Typical heading errors are 186 nT for Rb^{85} and 82 nT for Rb^{87} .

Ruddock (1961) developed an elegant dual cell system to reduce the heading error by an order of magnitude. The block diagram of the dual cell system is shown in Fig. 2.5c.

Another method which uses a split cell instead of two cells was suggested by Yabuzaki (1973). This system however cannot give continuous signal and has not been used for rocket measurements.

An important factor in the operation of a rubidium magnetometer is that the temperature of Rb gas cell must be maintained at a constant temperature between 35° and 40° C. This will ensure a good S/N and a steady signal which is necessary for trouble free operation of the unit. The cell is warmed by passing a low frequency current through a coil wound around the cell. The temperature of the cell is sensed by a minute thermistor put in contact with the cell and the cell temperature is controlled electronically. In the rocket magnetometer, heating is done only during the pre-launch period when the payload is still on the launcher. Heat around the sensor is conserved by suitable lagging and potting. This keeps the cell temperature within limits during the actual flight. No heating is done during the flight.

The first Rb magnetometer was designed and constructed by Bell and Bloom (1957). Since then several single cell self oscillator systems as well as dual cell systems have been flown in rockets and satellites. The rocket-borne Rb magnetometers have been used to study the electrojet and the Sq current systems by Davis et.al., (1965, 67). Cloutier and Haymes (1968), Shuman (1970), Yabuzaki and Ogawa (1975), Burrows and Sastry (1976) and Burrows et.al., (1976).

1.1.2.2 Rb Magnetometer Payload design:

The Sensor: The complete system Fig. 2.5b consisting of the Rb lamp, the interference filter, the circular polariser, the Rb vapour cell, the photocell and the collimating lenses are enclosed in a Hylam tube and aligned for maximum efficiency for light transmission. This system which is generally called the sensor is shielded from external r.f. interference by an electrostatic shield. It is then rigidised and potted to withstand the thrust and vibration of the rocket take-off. The output of the photocell is taken to the amplifier through shielded cables.

The VHF Oscillator: The power to the Rb lamp is supplied from a remote oscillator through low loss shielded r.f. cables. The oscillator itself is housed in an airtight aluminium chamber to avoid change of frequency due to change in humidity.

The aluminium enclosure also acts as shield and prevents interference of oscillator frequency with the signal frequency. The oscillator delivers 3 watts of power to the lamp at 100 MHz.

The Amplifier: The amplifier has low noise, high gain and a band-pass characteristic. The lower edge of the band-pass is set at 130 KHz which corresponds to the field value at a rocket apogee of 200 kms. The higher edge is set at 200 KHz which corresponds to the field at the ground. The output of the amplifier directly modulates a 240.3 MHz FM/FM transmitter.

2.1.2.3 Integration and Pre-launch operation of the payload:

Inside the rocket nose cone, the sensor is mounted well away from the electronics and the sub-systems. This is to ensure that, at the sensor, the magnetic field due to the electronics and the fields due to the flow of currents in the cables are negligible. The nose cone, the decks and the fixtures are made out of fibreglass and thus contribute little to the pollution of the data. The Rb magnetometers were flown from Thumba either on Indian centaures or British Petrels. The second stage of these rockets are made of steel. To avoid the modulation of the data by the magnetic field of the rocket second stage, the forebody of the rocket containing the experimental payloads was ejected well before the rocket enters the electrojet.

In the flights 20.13 (P110) and 20.14 (P59), the sensor was aligned with the spin axis of the rocket and in the flight 20.15 (P60), the sensor was mounted at an angle of 45° to the rocket spin axis. Both these configurations have their advantages and disadvantages. Axially mounted sensors give continuous data provided the launch elevation is adjusted to bring the geomagnetic vector into the sensor live zones. This results in a significant loss of apogee height. The 45° mount on the other hand, gives good data without compromising the vehicle performance, but goes through two dead zones during a spin period.

Some of the problems faced during the pre-launch operation of the Rb magnetometer are as follows:

1. The main problem was due to the r.f. interference especially from the radiation from the telemetry transmitter. The pick up of the radiation by the amplifier and the associated cables necessitated special shielding and proper grounding of the radiation shields. The inside of the fibreglass nose cone had to be sprayed with a conducting paint to suppress the radiation pick up.
2. Under conditions of low pressure, corona discharge between the tank circuit of the oscillator and the Rb lamp surface, may take place. This means loss of power

delivered to the lamp for excitation. Due to this, the lamp glow shifts resulting in unsteady and noisy signal. In worst cases the lamp might get extinguished. To prevent this, it is necessary to check that the sensor potting is leak proof. Each sensor must be operated in a vacuum chamber to check that the corona discharge does not take place at low pressures.

3. The temperature of the Rb cell has to be carefully monitored and maintained at 40°C till launch.
4. The ripple in the output of the DC/DC converter supplying power to the telemetry transmitter was found to interfere with the performance of the magnetometer. This problem was solved by reducing the ripple in the output of the DC/DC counter to less than 10 mV.

2.1.2.4 The Data Reduction System:

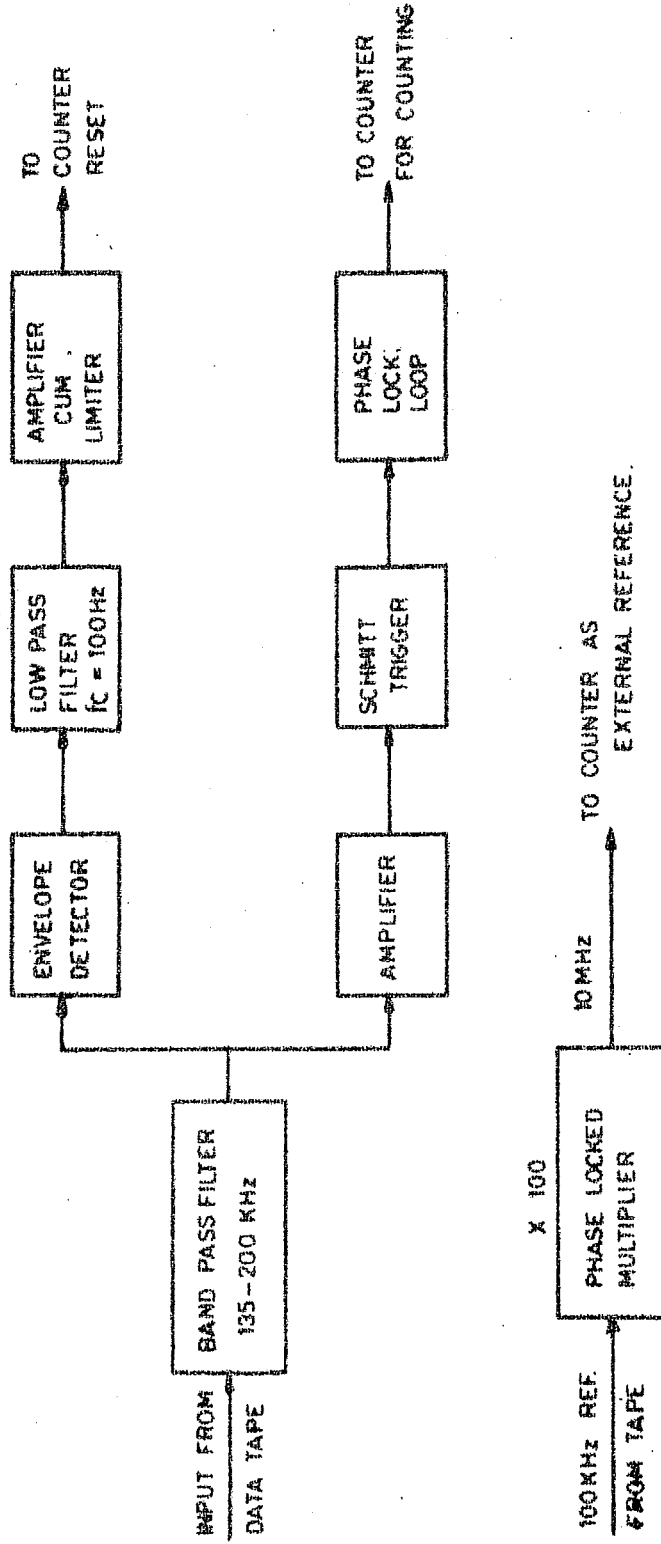
The data from the Rb rocket magnetometer can be reduced in a way similar to that described in section 2.1.1.4 for the reduction of data from the proton magnetometer. Since the data from the Rb magnetometer is continuous, the use of a dual preset will not be necessary. The method described in 2.1.1.4 however does not result in full utilisation of the continuous data available from the Rb magnetometer. The reasons are:

- a) The digital printer used can print only ten lines per second, hence it limits the sampling rate to 10 per second. Since the output from the Rb magnetometer is continuous, sampling of the data at a fast rate for obtaining good time resolution for fluctuations is possible.
- b) The rocket magnetometer data may contain large loops of modulation due to the heading error and frequent patches of data with poor signal to noise ratio due to the dead zones. The data from the proton magnetometer is free from such effects. To recover all the good data from the Rb rocket magnetometer, a different data reduction set up will be necessary.

One of the methods is to use very fast sampling technique and eliminate the bad data during the data analysis with the help of a computer. Since a fast sampling and digitising facility was not available, it was decided to develop a system with available equipments, to recover the data with reasonably good time resolution. The details of this system are shown in Fig. 2.6 and 2.7.

The magnetometer data is recovered from the data tape by passing it through a band-pass filter with a pass-band of 130-200 KHz. This data will be amplitude modulated due to the dead zones. The output of the filter is divided into two channels. In the first channel, a control pulse is derived from the data itself, which operates the counter

RUBIDIUM MAGNETOMETER DATA REDUCTION SYSTEM



BLOCK DIAGRAM

FIG. 2.6. Block diagram of the Rb. magnetometer data reduction system.

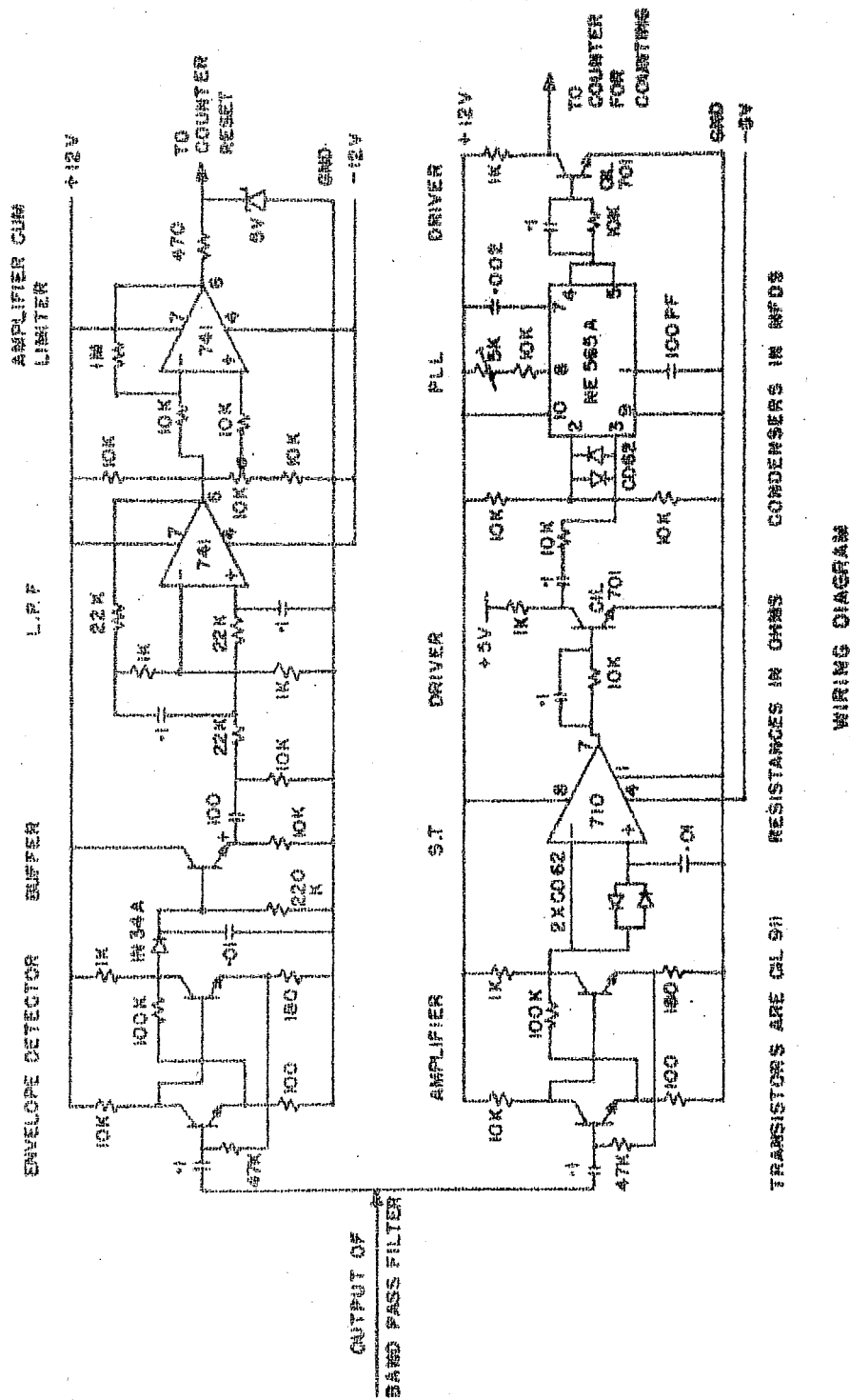


FIG. 2.7. Circuit details of the data reduction system shown in fig. 2.6.

only when there is good data. In the second channel, the signal is cleaned and fed to the counter for counting.

In the first channel, the envelope of the signal waveform is detected and the detected output is passed through a low pass filter with a cut off frequency of 100 Hz. The low pass filter eliminates spurious high frequency modulations from the detected output. The output of the low pass filter is passed through an overdriven amplifier. The output of this amplifier will be a series of pulses. The duration of these pulses correspond to the portions of good data. The raw data and these pulses are examined on a dual beam oscilloscope to check that there is no phase lag or lead between the pulses and the patches of good data. The d.c. reference of the amplifier can be changed by the help of a potentiometer. Increasing the reference voltage will narrow the pulse width and will select only data with very good S/N.. This potentiometer has to be set after examining the quality of the data. The amplifier output is clamped at 5 volts using a Zener diode, and given to the reset terminal of the 10 MHz counter. (The clamping at 5 volts is necessary for TTL compatibility). By this way, the counter will operate only when a pulse is present and at other times the reset terminal will be grounded and the counter will not operate. The sampling rate of the counter can be set such that all

the ten prints per second on the printer will be good data points.

In the second channel, the raw data is amplified and given to a Schmitt Trigger. This Schmitt Trigger is built around a 710 comparator. The reference for the comparator is derived from the raw data itself as shown in the Fig. 2.7. The output of the comparator will be square waves corresponding to the input data. This is now given to a phase lock loop that locks in the range of 130-200 KHz. This is constructed using a NE565A PLL chip. The output of the PLL goes to the input of the counter for counting the frequency or time interval.

The 10 MHz reference for the counter is derived from the standard 100 KHz reference recorded in the data tape along with the flight data. This 100 KHz is phase lock multiplied by 100 times to get the 10 MHz. This multiplier is built using a NE562B integrated circuit.

This system was used to reduce the flight data. It works satisfactorily when the heading error is small and the dead zones are few per second.

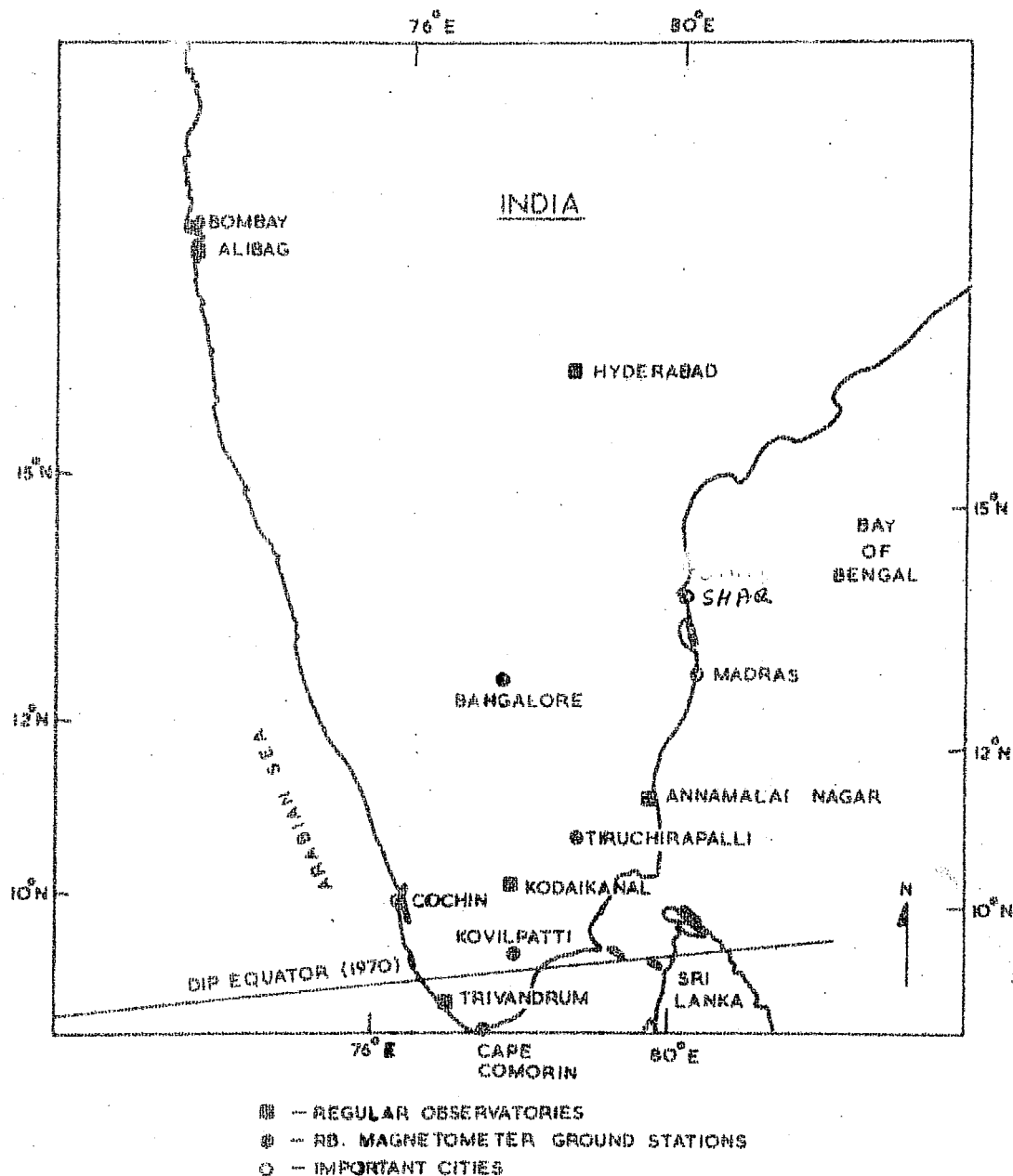
2.1.3 Ground Magnetometer Stations - Set Up:

Four ground magnetometer stations were set up in the equatorial electrojet region in India, as ground support

stations for the rocket magnetometer launchings conducted from Thumba during the early period of 1972. The stations were set up at Cape comorin, Kovilpatti, Tiruchirapalli and Bangalore and run during the period December 1971 to April 1972. The location of the dip equator (Shanker Narayan and Chari 1971) and the latitudinal distribution of these stations are shown in Fig. 2.8. The coordinates of the standard observatories and the temporary Rb magnetometer stations are given in table 2.1. The data from these stations and those from regular observatories (also shown in Fig. 2.8) were used to get the latitudinal profile of the electrojet intensity. These profiles were used to deduce the width of the electrojet at the time of in-situ measurements of electrojet parameters.

The experimental set up at all the four stations mentioned above, were similar. A typical installation at Tiruchirapalli is described here.

Single cell, self-oscillating Rubidium magnetometers were used at all the ground stations. It was planned to measure only the variations in the H component of the geomagnetic field. A Helmholtz coil system was used to nullify the vertical component of the field at Tiruchirapalli and Bangalore, which are far away from the dip equator.



LATITUDINAL DISTRIBUTION OF GROUND
MAGNETOMETER STATIONS

FIG. 2.8. The latitudinal distribution of the standard magnetic observatories and the temporary ground Rb. magnetometer stations set up in 1972 for the study of the equatorial electrojet. The dip equator determined from the latest magnetic survey in the region (Shankar Narayan and Chary 1970) is also shown. The coordinates marked are Geographic.

Stations	Geographic		Dip latitude		Magnetometer type
	Lat.	Long.			
Cape Comorin	8.083	77.55	-1.25		Rubidium
Trivandrum	8.48	76.95	-0.50		Variometers (Observatory)
+Kovilpatti	9.167	77.88	0.167		Rubidium
Kodaikanal	10.23	77.48	1.5		Variometers (Observatory)
Tiruchirapalli	10.83	78.83	2.4		Rubidium
Annamalainagar	11.40	79.68	2.75		Variometers (Observatory)
Bangalore	12.967	77.58	4.57		Rubidium
Hyderabad	17.45	78.46	10.13		Variometers (Observatory)
Alibag	18.63	72.87	12.5		Variometers (Observatory)

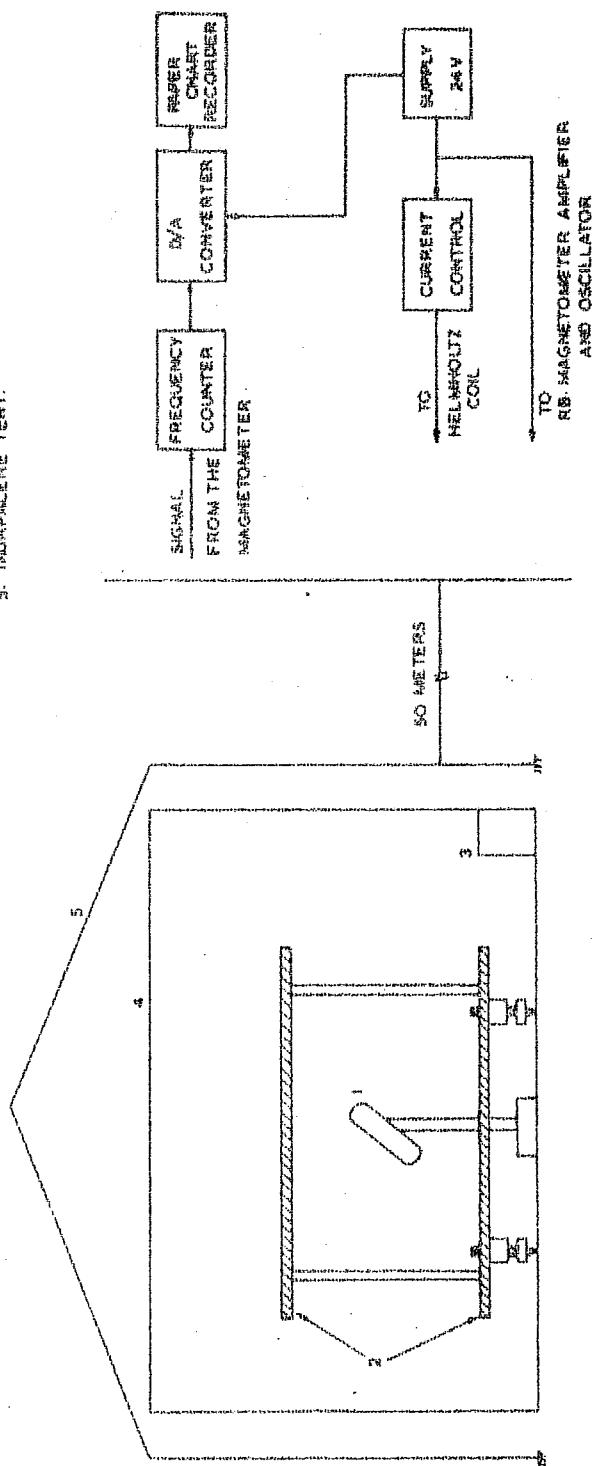
TABLE 2.1. Geographic coordinates and the dip latitudes of regular magnetic observatories and temporary magnetic stations in the southern part of India are given in the table.

+Note:- A new regular magnetic observatory has been recently established at Ettayapuram, near Kovilpatti, close to the dip equator. It was not there at the time of the present investigation.

The block diagram of the set up is shown in Fig. 2.9. The Rb sensor was kept at the center of the Helmholtz coil system and the sensor position was adjusted to get the maximum signal, as monitored on an oscilloscope. When there is no current through Helmholtz coil, the magnetometer measures the total field. The magnetometer signal was put to a frequency counter, and the signal frequency was noted. Then, current was passed through the Helmholtz coil and adjusted till the counter reading was a minimum. In this position, the magnetometer measures the H component only. The current control was left undisturbed in that position. It should be noted that this adjustment compensates the steady vertical field and it does not however compensate its variations.

The last two digits displayed in the counter were D/A converted using the BCD output of the counter and given to a paper chart recorder. By changing the sampling time of the counter, the sensitivity of the recording can be changed. A full scale sensitivity of 200 nT was used at all the stations except Bangalore. The smallest division on the paper chart for the above sensitivity corresponds to 4 nT. At Bangalore, the diurnal variation is expected to be small, being outside the electrojet region. A full scale sensitivity of 20 nT was used here. The smallest division on the paper chart here corresponds to 0.4 nT.

1. RB SENSOR
2. HELMHOLTZ COILS
3. MAGNETOMETER OSCILLATOR & AMPLIFIER ASSEMBLY
4. PLYWOOD CASE
5. TARPALINE TENT



GROUND MAGNETOMETER SET UP

FIG. 2.9. Schematic of the ground Rb. magnetometer station at Tiruchirapalli. The set up at the other ground stations were similar to the one shown here. The electronic accessories were kept in a nearby building. The detailed electrical connections are not shown in the figure.

A small room adjoining a large open space was chosen as the site for installing the magnetometer. The Rb sensor and the Helmholtz coil were kept inside a plywood case. The magnetometer amplifier and the lamp oscillator were kept in one corner of the case. This case was placed in the open space. A taurpalene tent protected this case from stray cattles and the vagaries of weather. The counter, the paper chart recorder, D/A converter and other accessories were kept in the adjoining room. Power to the Helmholtz coil and the magnetometer was supplied from lead acid accumulators in the room. The magnetometer signal was taken to the room through shielded cables. The signal cables and the power lines were laid underground. The counter and the paper chart recorder were operated on 220V, 50Hz mains. Time marks were put on the paper chart at least twice a day. The complete reading on the face of the counter at the time of these time markings were also recorded on the chart for calibration purposes.

The following precautions were taken in installing and running these ground stations.

1. A magnetically clean site with least interference from electrical noise and vehicular traffic was chosen for the installation.
2. The plywood case, the taurpalene tent and the other accessories used in the set up were made of non-magnetic materials.

3. The time markings were synchronised with the Indian Standard Time (82.5° EMT), at all these stations, to facilitate data reduction and analysis.
4. All the digits displayed in the counter were noted down on the chart near each time mark. This would enable the calibration of the data and also checking of the normal functioning of the system.
5. The batteries were kept on floating charge and their voltages were checked periodically.

Excellent and continuous records were obtained on days when there were no power failures. Sample records of the daily variations recorded at Tiruchirapalli and Bangalore are shown in Fig. 2.10 to indicate the quality of the data from these stations.

2.2 Electric Field Measurements in the Ionosphere:

The methods of measurement of electric field in the ionosphere so far used may be classified into two broad groups. The first method depends on the measurement of potential difference between pairs of conductors inserted in the plasma, and the second method depends on the measurement of parameters of bulk flow of the ionospheric plasma. The second method includes the measurement of back scatter by radar technique, artificial ion cloud motion and the

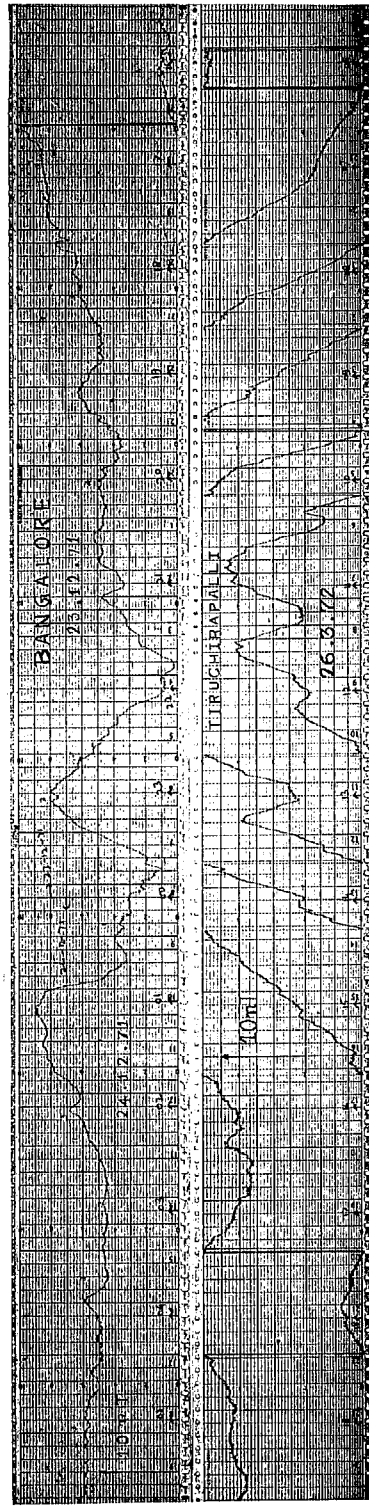


FIG. 2.10. Sample records of the magnetic variations recorded at the Rb. magnetometer ground stations Tiruchirapalli and Bangalore. The records show the quality of the geomagnetic variations data obtained from these stations.

effect of bulk flow on antenna impedance. The merits, errors of measurement and the uncertainties involved in each of these methods have been comprehensively discussed by Maynard (1971) and Mozer (1973). For the investigation of electric field fluctuations associated with the plasma instabilities in the E-region, the subject in which we are interested here, the only convenient and successful technique available at present is the Langmuir double probe technique.

2.1 The Langmuir double probe:

2.1.1 Principle:

This system consists of two identical metallic probes deployed into the plasma, well away from the main rocket body. The probes are separated from each other by a distance D such that the rocket sheath does not affect the measurements. The metallic probes must have dimensions larger than the Debye length of electrons in the region of measurement. The potential difference ΔV between the two probes is measured using a high input impedance differential amplifier, with a high common mode rejection. Then $\Delta V/D$ gives the electric field along the line joining the two probes. This method though appears simple, demands certain precautions to be taken concerning the distance between the probes, deployment symmetry, similarity of probe surfaces and the input impedance

of the amplifier as discussed by Fahleson (1967) and Mozer (1969). There is always the possibility of mistaking the rocket and wake generated fluctuation for genuine effects under investigation, Mozer (1973). Genuine data must be recovered by careful screening of the data for identification and elimination of the spurious effects.

The first set of experiments using the Langmuir double probe was conducted from Thumba on Indian centaure rockets. The design of the payload flown on these rockets is detailed below.

2.2.1.2 Design of the experiment:

The probes used were nickel spheres of 5 cm diameter. The probes were checked for low photoelectric emission and high sphericity. The probes were coated with colloidal graphite to have a uniform contact potential all over the surface of the probes. They were mounted on a fibreglass boom such that the distance of separation (D) is 2 meters. This separation distance is large enough for the measurement to be unaffected by the rocket sheath (Mozer 1973). The probes were deployed soon after the rocket leaves the dense atmosphere.

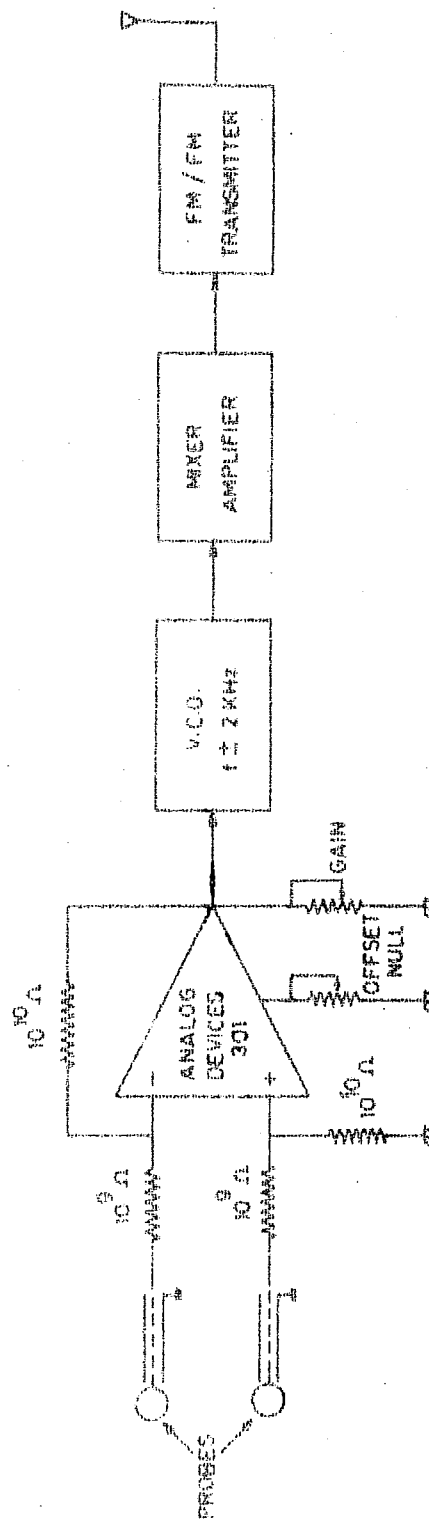
The two probes were connected to a high input impedance differential amplifier of the Analog Devices 301 model.

This has got a high input impedance and a high common mode rejection ratio. The frequency response of the amplifier was set from dc to 1 KHz so that fluctuations in the electric field upto a frequency of 1 KHz can be measured. The block diagram of the payload is shown in Fig. 2.11. The output of the amplifier goes to a V.C.O. and the V.C.O output is fed to a mixer amplifier. The output of the mixer amplifier modulates an FM/FM transmitter.

The experiment flown on Centaures carried multiple double probes to measure the components of d.c. electric field and the fluctuations in the electric field. To facilitate comparison between different channels, constant bandwidth (± 2 KHz) V.C.Os were used instead of the usual IRIG proportional bandwidth ones. This bandwidth of 4 KHz is sufficient to transmit fluctuations upto 1 KHz.

2.2.1.3 The Data Reduction System:

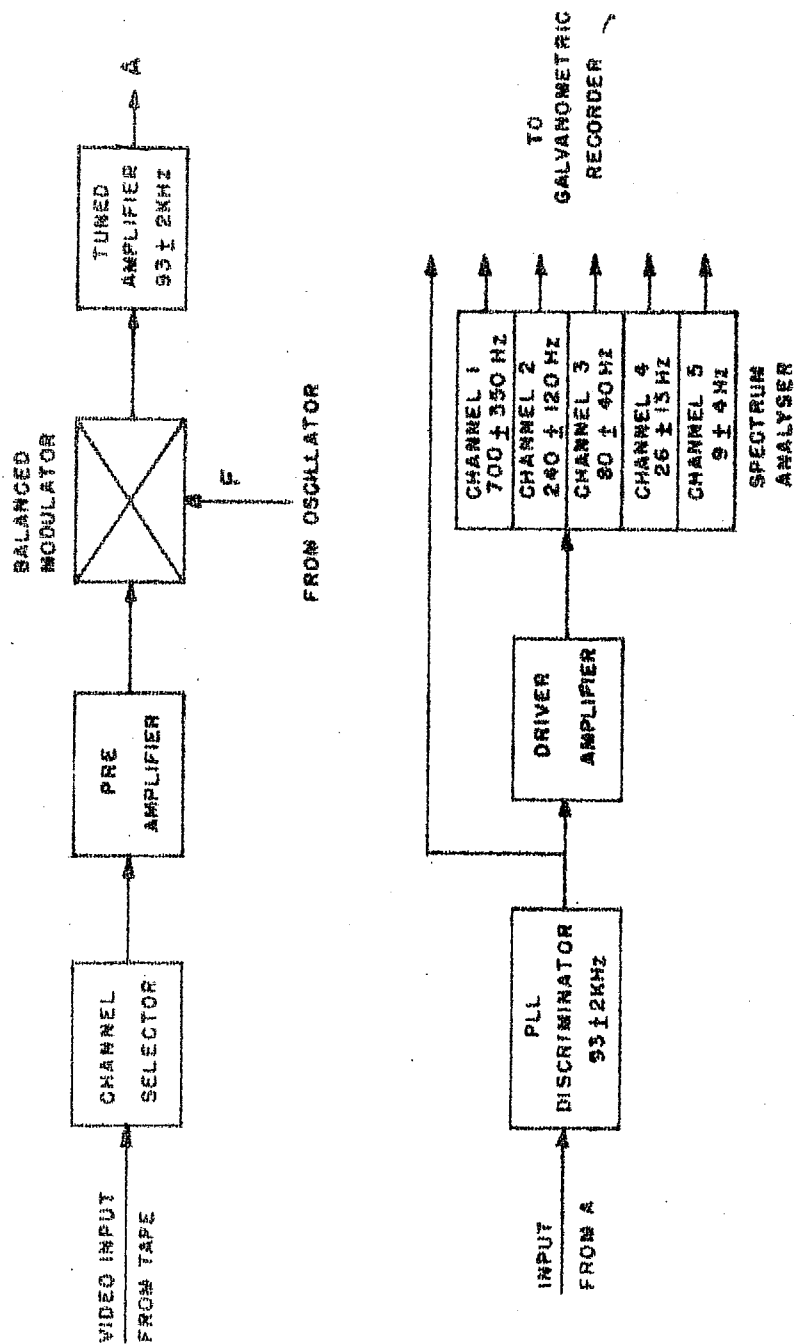
To reduce the data from these flights, constant bandwidth discriminators corresponding to the V.C.O's used in the payloads are necessary. Since such discriminators were not available a suitable data reduction system had to be designed. The system designed is shown in the block diagram of Fig. 2.12. The video output from the data tape is given to a channel selector, to select any desired channel. The



BLOCK DIAGRAM OF THE ELECTRIC FIELD PAYLOAD

FIG. 2.11. Block diagram of the Langmuir double probe electric field detector payload flown on Centaure rockets from Thumba. The V.C.O.s used are of constant band width type.

DATA REDUCTION SYSTEM FOR ELECTRIC FIELD FLUCTUATIONS



BLOCK DIAGRAM

FIG. 2.12. Block diagram of the data reduction system developed for the reduction and analysis of the electric field fluctuations obtained from the rocket-borne Langmuir double probe detector system of fig. 2.11.

output of the channel selector is amplified and fed to a balanced modulator. The local oscillator of the balanced modulator is a standard crystal controlled signal generator. The balanced modulator output is fed to a tuned amplifier. The local oscillator frequency is precisely adjusted for each channel, so that the difference in frequency between the local oscillator and the signal from the pre-amplifier, is always within the band pass range of the tuned amplifier. The output of the discriminator is given to a 5 channel spectrum analyser through a driver amplifier. The spectrum analyser has 5 constant Q, equal gain, band pass filters that cover the frequency range of 5 Hz to 1 KHz. The output of the spectrum analyser and the raw data from PLL discriminator are recorded using a fast galvanometric recorder. The resulting records are shown in Figures 7.5 to 7.8 of chapter 7.

The detailed circuit diagram of the system is shown in Figures 2.13 and 2.14. The channel selector is a simple parallel LC circuit. By switching different capacitors in place of "C", the channels are selected. The pre-amplifier is a transistor amplifier. The balanced modulator is constructed out of two CA 3028 A Op. amps. The Op. amp. CA 3028 A contains a differential pair with a constant current source within it. The signal from the pre-amplifier is given to

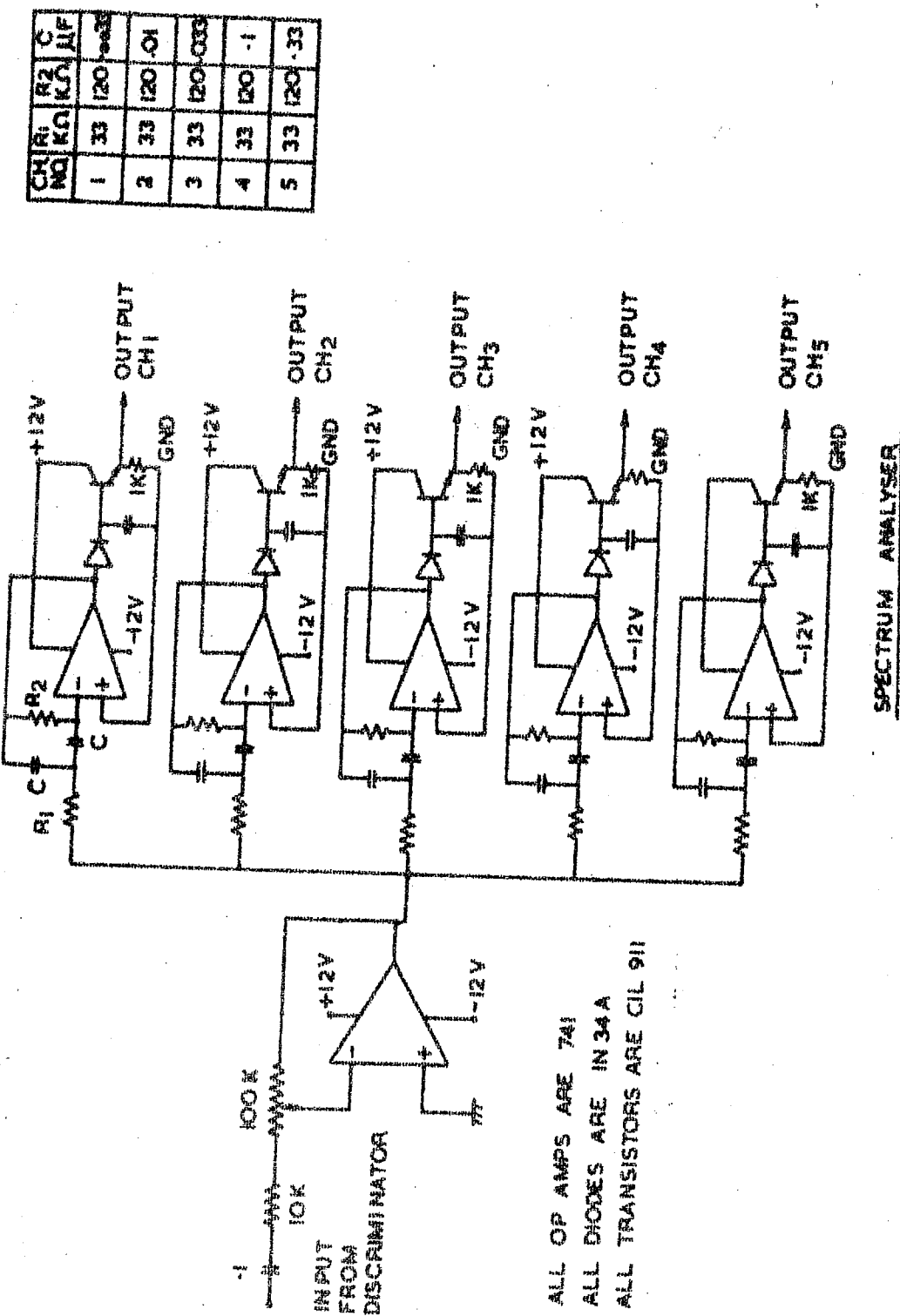


FIG. 2.14. Circuit details of the five channel spectrum analyser used in the data reduction system shown in fig. 2.12.

the base of the one of the differential pair of op. amp. 1 (pin 1) and the local oscillator output (F) is connected to the base of the constant current source (pin 2) of the same op. amp. The second op. amp. (CA 3028A) of the balanced modulator is connected to the first op. amp. in such a way that there will be an output from the modulator, only when the signals from both the pre amplifier and the local oscillator are simultaneously present, at the inputs of op. amp. 1 (pin 1 and 2 respectively of first CA 3028A).

The tuned amplifier uses a parallel LC circuit in the feedback loop of a multistage transistor amplifier. The PLL discriminator is made out of a NE 565A PLL I.C. and a 741 Op. amp. which functions as a differential amplifier. The center frequency of the tuned amplifier and the PLL discriminator is set at 93 KHz. When 93 KHz is chosen as the center frequency, the local oscillator frequency F must be adjusted to $(93 \text{ KHz} + f_{ch})$ where f_{ch} is the center frequency of the channel selected. This results in the balanced modulator, always delivering the standard output of 93 KHz to the tuned amplifier PL discriminator system. For a clean output from the discriminator, this center frequency must be carefully chosen; the criterion being that there should be no information in the original signal within $\pm 2 \text{ KHz}$ of the

center frequency. The discriminator output goes to the five channel spectrum analyser. The spectrum analyser is built out of 741 Op. amps. The band pass filters used are second order active filters. A common driver at the input, controls the overall gain of the system (Fig. 2.14).

In this chapter, the method of deriving the vertical profile of the electrojet current density from the rocket-borne magnetic field measurements is described. Further, various errors and uncertainties associated with the magnetic field measurements by rocket-borne magnetometers are discussed.

The rocket magnetometer data, after reduction finally comes out in the form of digital print-outs, as described in chapter 2, sections 2.1.1.4 and 2.1.2.4. This is the raw data with which the analysis begins. The procedure of deriving the altitude profile of the current density from the raw data will be described below.

3.1 Determination of the profile of field intensity (F) versus the flight time (T):

The digital print-outs will contain the Larmor frequency or its time interval printed out against the time at which the sample is made. The first step in the data analysis is to convert the magnetometer frequency into the total field intensity F . In the case of the proton

magnetometer, 0.0426 Hz of precession frequency corresponds to 1 nT field and for the Rb^{85} magnetometer, 4.66744 Hz of the magnetometer frequency corresponds to 1 nT. These conversion factors are used to convert the frequency or the time interval to the total field intensity.

As discussed in the sections dealing with the data reduction system in chapter 2, the flight data tape is first run for a few times to check the stability and the consistency of the data reduction system. After establishing the consistency of the data reduction system, the flight tape is run several times and the reduced data which is in the form of print-outs is analysed to get a statistical picture of the scatter in the data. In the case of the proton magnetometer, the flight tapes are normally run atleast twenty times. The frequency values for each sample obtained from these runs are plotted as histograms. When the signal to noise ratio is high for the sample, the number of concurrent values are high and therefore the histogram will show a prominent peak. In the case of samples with poor signal to noise ratio, the number of non-concurrent values will be high. This gives a flat histogram, and the data point will appear as a noise point, because of the large uncertainty in determining the exact value of the field. The most concurrent value

obtained for each sample, is then converted to the total field F , using the above said conversion factors. The field value thus obtained is plotted against the flight time. One such curve obtained from the flight Fl. 20.09 is shown in Figure 3.1. It can be seen that there is not much scatter in the data, which indicates the good performance of the magnetometer.

In the case of the Rb. magnetometer, the signal to noise ratio is quite high compared to the proton magnetometer, except at and near the dead zones. As the signal is continuous in the case of the Rb. magnetometer, the number of samples per second can be quite high. Using this high density data, the noise points at and near the dead zones can be eliminated, as they fall significantly away from the correct trend of the data. The heading error, which appears as a modulation with spin frequency can be averaged out. Sampling at a high rate is resorted to, when time resolution is important for the study of rapid fluctuations in the magnetic field and also to recover useful data to the maximum. But, since sampling at high rate does not permit averaging over a long period, the scatter in the data will be more and also the error in the determination of the exact field value will be high. Both the methods are

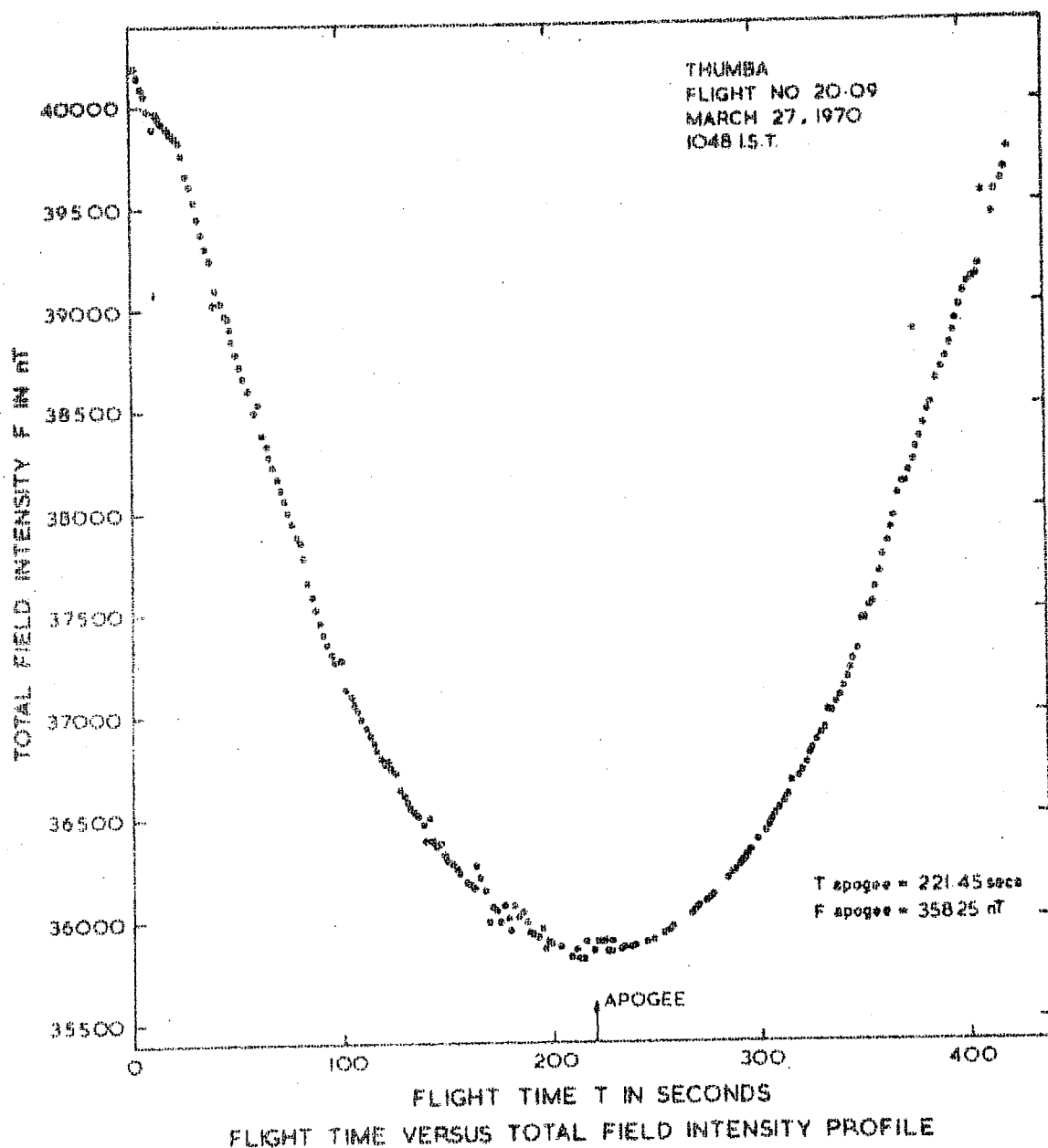


FIG. 3.1. A typical plot of the rocket measured total field intensity F , over Thumba, near local noon, against rocket flight time, T . It is seen that the scatter in the data points is low, hence, the flight is good. F is minimum at the apogee. Such plots have been used to derive the apogee time accurately. The F_{min} value at the apogee and the corresponding apogee time are shown in the figure.

used to keep a check on each other, so that no useful information is lost. The Rb. data tapes are run only two or three times and these runs are analysed individually and the final results are compared to check the consistency of the data.

The next step in the analysis is to convert the flight time versus total field information into altitude versus total field profile. This requires information regarding the rocket trajectory.

3.2 The Trajectory determination:

The information regarding the rocket trajectory is obtained with the help of four systems, the radar, the tone-range system, the alphasatron pressure gauge and calibrated pressure switches and the on-board magnetometer itself.

The radar operates either on the transponder mode or on the skin-track mode. When a transponder is flown in the rocket, the vehicle is tracked by the radar in the transponder mode. In this case, the trajectory information of the complete flight is obtained. When there is no onboard transponder, the rocket is tracked on the skin mode. The range radar could track the vehicle in this mode upto an

altitude of 60 km during the ascent only. The rest of the trajectory information had to be obtained by theoretical means.

In the case of the tone-range system again, complete trajectory information is obtained when a tone-range receiver is flown on-board along with the experimental payloads. When there is no on-board receiver, the ground tone-range system gives information concerning the elevation and azimuth of the vehicle during the flight. In this case, the ground tone-range system records continuously the variation in the relative phase of the telemetry carrier received by a pair of mutually perpendicular interferometer antennas. From this, the elevation and azimuth of the vehicle are computed. The different techniques and methods used for the trajectory determination have been detailed by Gruenberg (1967).

The rocket magnetometer data is used to determine the rocket apogee time, which is essential to compute the trajectory when the rocket is tracked on the skin-track mode. The apogee time corresponds to the time at which the lowest magnetic field is measured, near the apogee. In actual practice, a parabola is fitted to the points near the apogee, where the effect of ionospheric currents are negligible,

and from this parabola, the apogee time is determined. The apogee time thus obtained and the corresponding field value are indicated in fig. 3.1.

The Alphanatron pressure gauge developed by Sastry et. al., (1975), (see reprint attached), has proved to be an useful instrument for obtaining time versus altitude information of a rocket flight during both the ascent and the descent. It gives atmospheric pressure measurements upto an altitude of 50 km. Calibrated pressure switches, set to go off at 5000, 7000 and 11000 ft. are usually flown along with the Alphanatron as a means of in-flight calibration. Comparing the pressures measured by the Alphanatron gauge with the values given by a standard atmospheric model, the altitude values can be obtained against time. This information is supplementary to the radar skin-track data, in deriving the complete trajectory. The Alphanatron gauge is very useful since it gives the altitude information both during the ascent and the descent while the range radar at Thumba, operating on skin-track mode can track only in the ascent. Even when both the tone-range system and the radar on the range were operating well, the Alphanatron was included in many payloads as a good redundancy aid for trajectory determination.

The complete trajectory information for the rockets that were tracked by the radar on the skin-track mode is derived in the following way.

The rocket is assumed to fall freely from the apogee under the varying force of gravity. The effect of atmospheric drag, above 60 km altitude has been considered negligible. The apogee time, that is the time at which the vertical velocity of the rocket becomes zero, is used in solving the equation of motion of such a body. The apogee time is obtained from the on-board magnetometer as described earlier. The flight times corresponding to a particular altitude is evaluated for upward and downward legs at regular intervals of 0.5 km altitude. The trajectory thus obtained is compared with the radar skin-track trajectory. The difference in these two trajectories is minimised and the final trajectory is obtained. The altitudes corresponding to the sample times are obtained by interpolation.

Using the trajectory thus obtained, the azimuth and elevation of the rocket are computed. These values should agree with the values got from the ground tone-range system. In cases where these values are very close but differ slightly, the trajectory is adjusted to match the

azimuth and elevation values obtained from both methods.

As the ground tone-range system gives the azimuth and elevation values throughout the flight, matching the azimuth and elevation values obtained from the trajectory with those got from tone-range, gives a good fit for the whole flight trajectory.

The trajectory information thus obtained is used to convert the time versus field profile into altitude versus field profile. The next step is to determine the altitude profile of the perturbation field (ΔF) due to the electro-jet current flow.

3.3 Derivation of the perturbation field ΔF :

In the absence of any over head current system, the earth's field will decrease with altitude in a smooth way without any discontinuity. The field due to the flow of ionospheric currents will introduce an observable discontinuity in the smooth decrease of the earth's field. The resultant field will be a vectorial addition of the earth's unperturbed field and the field due to the currents. It is this resultant field that is measured by a rocket magnetometer, as it traverses the current layer. In the case of the equatorial

electrojet that flows eastwards, its magnetic field will add to the earth's field below the layer, and subtract from it above the current layer. Over the dip equator, the earth's field and the field due to the electrojet currents are in the same direction, in the magnetic meridian plane. Hence, a mere algebraic subtraction of the earth's field from the rocket measured field, will give the field due to the electrojet currents. The earth's field for any given altitude can be evaluated theoretically. If ΔF is the field due to the currents, F , the rocket measured field and F_T the theoretically computed earth's field, then

$$\Delta F = F - F_T$$

ΔF is referred as the difference field and F_T as the theoretical field.

3.4 Evaluation of the theoretical field F_T :

The magnetic data from the ground-based observatories are spherical harmonically analysed, and the coefficients obtained are used to deduce the earth's field as a function of altitude at a given location (geographic coordinates), for any epoch. A detailed summary of the method of spherical harmonic analysis has been given by Chapman and Bartels (1940) and a method of computing the earth's field using the

spherical harmonic coefficients, using digital computers is given by Cain et. al., (1964). Here, the coefficients of Jensen and Cain (1962) for the epoch 1960 have been used, after applying the necessary corrections for secular variation, to derive the theoretical field for the rocket launchings from Thumba.

To check whether the Jensen and Cain field truly represents the field over Thumba or not, it was compared with the actually measured field by a rocket magnetometer flown from Thumba around a quiet midnight, when the field due to the ionospheric currents and magnetospheric disturbances are negligible. In Figure 3.2, the field measured by a night-time flight FL. 20.08 is shown along with Jensen and Cain field F_T . The 20.08 field and F_T run parallel indicating that the slopes of these two profiles are nearly the same. A shift of about 60 nT in 20.08 (1968) and F_T (1970) is due to secular variation which is about 50 nT for the period 1968 to 1970, as given in the yearly "Indian Magnetic data", bulletin of 1972.

In Figure 3.2 the measured field of FL. 20.09, a magnetometer flight conducted near noon on March 27, 1970 is also shown. It can be seen that the theoretical Jensen

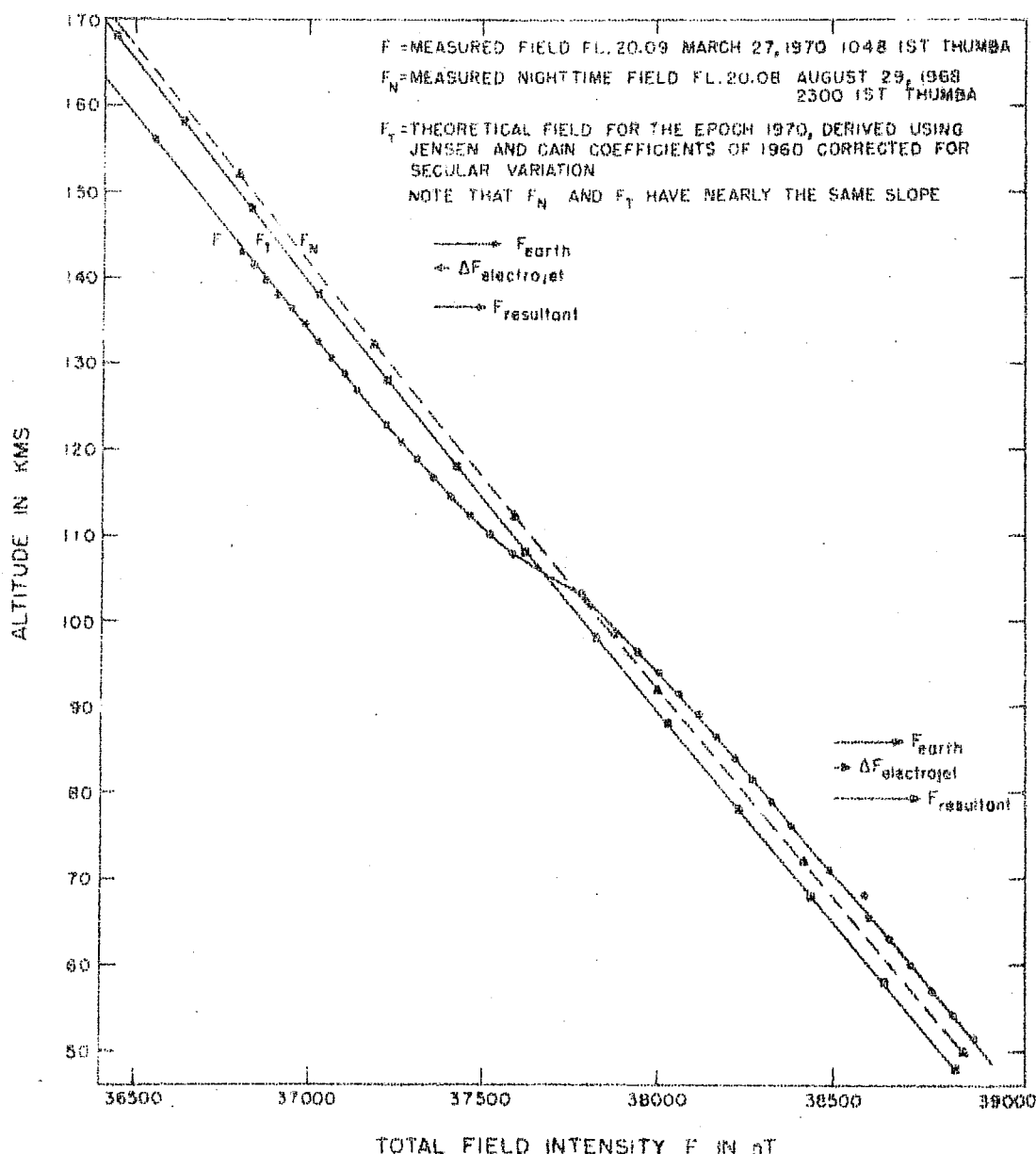


FIG. 3.2. F , the rocket measured field during the noon time, F_T , the theoretically computed field for this flight epoch and F_N , the rocket measured field at the night-time are shown against altitude, for comparison. It is seen that F_N and F_T have nearly the same slope. The difference in F_N and F_T is due to the secular variation. F_T passes through the center of the discontinuity in the F curve as expected. This discontinuity in F is due to the electrojet currents, whose field adds to the earth's field below the current layer and subtracts from it above the current layer, as shown schematically.

and Cain field F_T evaluated for this flight epoch, passes through the center of the discontinuity due to the electrojet, indicating that the theoretically evaluated field is a good representation of the earth's field over Thumba.

Having obtained the altitude profile of ΔF , by using $\Delta F = F - F_T$, the altitude profile of the current density J of the electrojet is derived as follows.

3.5 Derivation of the electrojet current density J :

The current density J and the magnetic field H due to the flow of this current are related by the Maxwell's equation,

$$\text{curl } H = \frac{4\pi J}{c} + \frac{1}{c} \frac{\partial D}{\partial t}$$

where $\frac{1}{c} \frac{\partial D}{\partial t}$ is the displacement current. Under the assumption that the current remains steady during the measurement, the displacement current term in the equation may be ignored. Then,

$$\text{curl } H = \frac{4\pi J}{c}$$

Consider a coordinate system, in which x axis is directed towards geographic south, y axis towards geographic east and z axis directed vertically upwards. If J_y is the

eastward electrojet current density, then evaluating $\text{curl } H$ and equating the y components on both sides, we get,

$$\frac{4\pi}{c} J_y = \frac{\partial H_x}{\partial z} - \frac{\partial H_z}{\partial x}$$

The distance travelled by the rocket in the x direction within the current layer is very small and also the field H_z due to the electrojet is very small at the center of the electrojet. Normally the rockets from Thumba for the study of electrojet are launched at an azimuth of 270° and elevation of 85° . In these cases, the rockets travel westwards parallel and close to the center of the electrojet. Hence the contribution to J_y from the term $\frac{\partial H_z}{\partial x}$ is negligible compared to $\frac{\partial H_x}{\partial z}$.

$$\therefore \frac{4\pi}{c} J_y = \frac{\partial H_x}{\partial z} = \frac{dH_x}{dz}$$

H_x , which is the field due to the electrojet current is denoted here as ΔF .

$$J_y = \frac{c}{4\pi} \frac{d}{dz} (\Delta F)$$

This shows that the vertical distribution of the current density J_y can be obtained from the slope of the altitude profile of ΔF . In other words, if ΔF_1 is the difference field at an altitude h_1 and ΔF_2 at h_2 , then

J_y at an altitude of $\frac{h_1 + h_2}{2}$ can be written as

$$J_y = \frac{10}{4\pi} \left[\frac{\Delta F_1 - \Delta F_2}{h_2 - h_1} \right]$$

If F is in nT, h in km, then the current density J_y is obtained in amp/km². The factor 10 is to convert abampere to ampere. (The factor c gets eliminated due to change in units).

3.6 Errors and uncertainties in the measurement and data analysis:

3.6.1 Error in the measurement of F :

In the case of the proton magnetometer, the magnetometer frequency f is related to the magnetic field F by the relation,

$$2\pi f = \gamma_p F$$

where γ_p is the gyromagnetic ratio of protons in water. The errors in the determination of F could arise due to two factors. The first, an error in the value of γ_p and the second an error in the measurement of frequency f . The value of γ_p has been measured by Driscoll and Bender (1958) as $\gamma_p = (2.67513 \pm 0.00002) \times 10^8$ radians/sec. tesla. An error of $\pm 2 \times 10^3$ radians/sec. tesla, in γ_p will give a constant error of ± 0.5 nT in the measurement of absolute field values.

In the frequency measurement, two kinds of errors occur, one in the counting of the frequency due to poor signal to noise ratio and the next one due to an uncertainty of ± 1 in the last digit counting by the counter. In the first case, the error $\pm dF$ in counting is given by Blacquire et. al., (1963) as,

$$dF = 1/\delta_p Rt$$

where R is the signal to noise ratio and t the sampling period. For the proton magnetometers flown from Thumba, the sampling period t is 0.5 second and the signal to noise ratio is about 8. In this case, when R, t and δ_p values are substituted in the above equation dF turns out to be 1 nT.

The counter counts 800 cycles of the precession frequency against the 10 MHz standard reference and displays the time period in micro seconds. The error due to ± 1 count uncertainty in the last digit counting, which is ± 1 micro second in the time interval mode, will be ± 0.2 nT.

Hence, the total probable error in the measurement of F by the proton magnetometer turns out to be $\sqrt{(0.5)^2 + 1 + (0.5)^2} = 1.14$ nT. This is the total error, provided the field F remains steady during the sampling period. In the case of the rocket-borne proton magnetometer,

during the time of 0.5 second, which is the sampling period selected for sampling the signal, the rocket travels a distance of about 0.5 km and the field does not remain steady during the measurement. But, if the field measured is an average value over this period, and the sample time is put at the center of this period, no additional error will be introduced into the measurement. This is especially true, if the sampling period is small enough to consider that the field F varies linearly within this period. In the technique of frequency counting used in the data reduction, the frequency is averaged by the counter over the sampling period, and the sample time is put at the center of the sampling period.

The proton data tape is run about 20 times and the frequency is selected by histogram, as discussed earlier. This will bring about an error in individual measurements due to the statistical distribution of values. For a very good sample, the typical error is about 1.5 nT. In the worst case, the histogram will be almost flat and the data point itself will appear as a noise point. The total probable error in the measurement of F by the rocket-borne proton magnetometer does not exceed 2 nT.

In the case of the Rb^{85} magnetometer, the magnetometer frequency f is related to the field F by

$$f(\text{in Hz}) = 466744 F + (K) 359 F^2$$

F is in Gauss and K is a constant, usually less than 0.5. The F^2 dependance is nothing but the heading error in the single cell system. This heading error appears as a modulation at the spin frequency, and can be eliminated during the data reduction.

In the case of counting the frequency, as the signal to noise ratio is quite high for Rb magnetometer, the choice of sampling period is the primary source for the inaccuracy. Counting ten samples per second against a reference of 5 MHz will give an accuracy of 0.1 nT, in the case of the Rb magnetometer. This may be taken as the over all accuracy. A detailed study of the Rb. magnetometer and the possible sources of errors are given by Grivet and Malnar (1967). The accuracy of the rocket magnetometer is discussed by Davis et. al., (1965, 1967), who also claim an accuracy of 0.1 nT for the field measurements.

3.6.2 Uncertainty in the trajectory determination:

As discussed earlier, the complete trajectory information is obtained, when a radar transponder is flown in

the rocket. The absolute error in the trajectory here is less than ± 0.5 km. When a tone-range receiver is flown in the rocket, then also complete trajectory information is obtained. The error here is less than ± 0.5 km. Hence, the error in the trajectory is very small when an on-board system for the trajectory determination is used.

In the case of rockets tracked by the radar on the skin track mode, the complete trajectory information is obtained by theoretical means. The correctness of the method used in this determination is checked by comparing the computed trajectory with the trajectory obtained by the tone-range system (using on board receiver), when both data are available. As for instance, the flight 20.09 had an on board tone-range receiver to give the complete trajectory information and the rocket was tracked by the radar on the skin-track mode. The trajectories obtained from both these methods agreed well within an error of ± 1 km. The ascent and descent ΔF profiles derived using these trajectories followed each other closely. The current density profiles derived from these ΔF curves peaked at the same altitude during ascent and descent. After thus establishing the correctness of the method, it was used to compute the trajectory of flights, where on-board systems could not be flown.

To demonstrate the effect of using incorrect trajectory on the ΔF profile, the ΔF profiles derived using the correct and an incorrect trajectory are shown in Figure 3.3 for the flight 20.09. In the case of incorrect trajectories, the ascent and descent ΔF profiles do not follow each other and this results in the currents peaking at different altitudes in ascent and descent. The determination of the apogee time correctly, using the on-board magnetometer data helps to resolve this problem.

3.6.3 Uncertainty in the theoretical field F_T :

If the field F_T evaluated using the spherical harmonic expansion is a true representation over the place of interest (Thumba), then the ΔF profiles will be symmetric with respect to $\Delta F = 0$. In other cases, the ΔF profiles will be asymmetric. In worst cases, all the ΔF values could be either positive or negative. It can be seen from Figure 3.2 that the Jensen and Cain coefficients represent the field over Thumba fairly accurately.

3.6.4 Rocket precession effect due to payload field:

Though every care is taken to minimise the payload field at the magnetometer sensor to be within a few nT, in

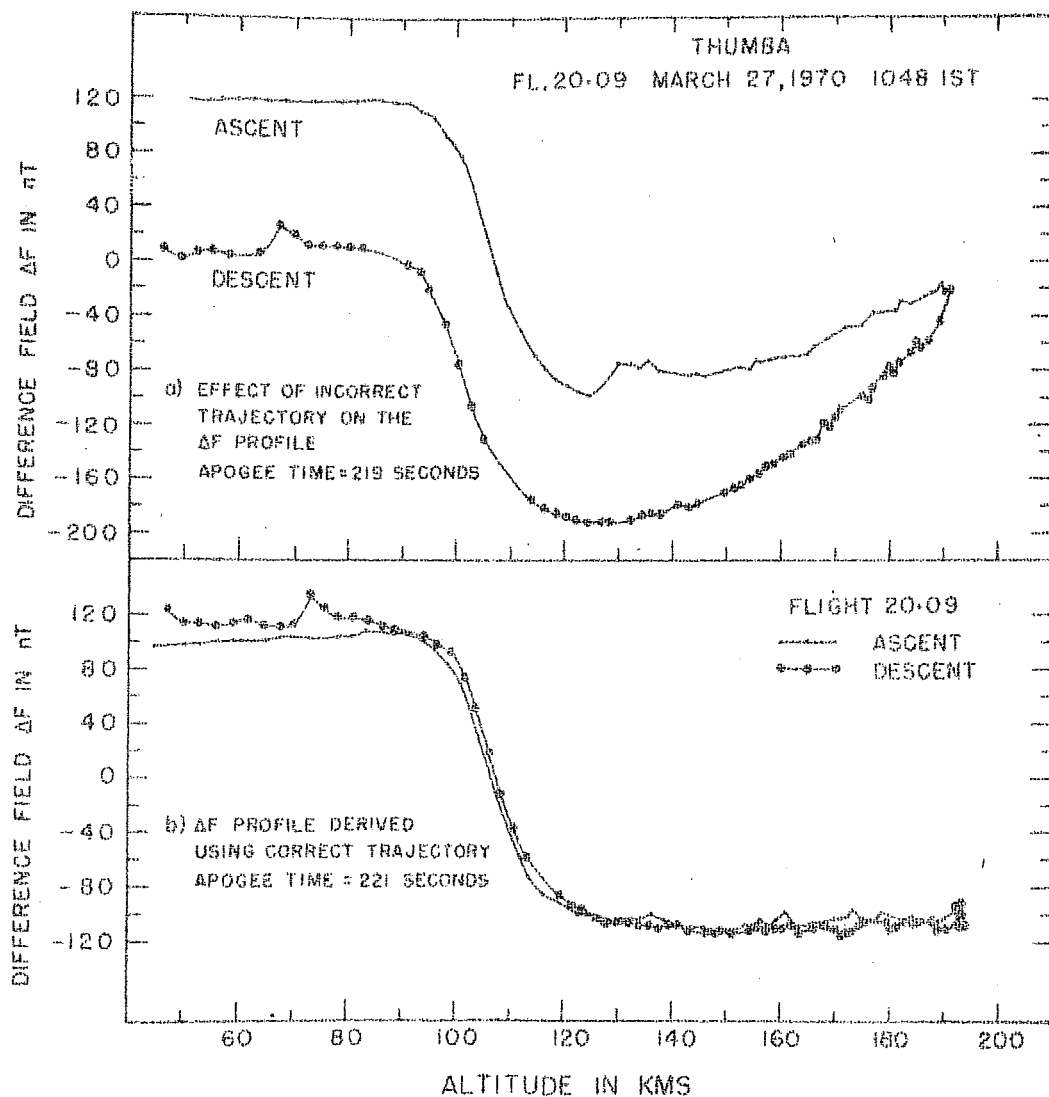


FIG. 3.3. The effect of incorrect trajectory on the ΔF profile is shown in the top figure. The ΔF profiles of the ascent and the descent of the rocket flight do not follow each other in this case. When the trajectory information is correct, the ΔF profiles follow each other closely as shown for the same flight in the bottom figure.

some cases it becomes appreciable. This field will add and subtract to the field being measured, due to the rocket precession. Under ideal conditions, this effect will appear as a sinusoidal modulation on the data. This can be removed by applying a correction of the form $A \sin \omega t$, as done by Davis et. al., (1967). In most of the cases, the amplitude and the period of this modulation vary during the course of the flight. Applying a general correction of the form $A \sin \omega t$ for the whole data will not be possible in such cases, as the data gets either under corrected or over corrected, which in turn will introduce some other modulations.

The modulation due to the precession effect is very distinct near the apogee, where the variation in the ambient field is very small as the vertical velocity of the rocket is small. When the ΔF values are plotted against time, this precessional modulation will occur at regular time interval and is easy to correct. One such curve is shown in Figure 3.4. The precession period for Nike-Apache rockets is around 32 seconds. In Figure 3.4, the amplitude is about 8 nT and the precession period on an average is about 35 seconds. When the ΔF profile is plotted against the altitude, the precession effect does not appear at regular altitude intervals as the rocket velocity is not constant with time.

Therefore, it is better to use the time versus ΔF profile for correcting the precession effects. The ΔF profile of FL. 20.06 which had negligible precession effect is also shown in Figure 3.4 for comparison.

In the case of the proton magnetometer, the ΔF curves are generally smoothed manually as the data point occur once in every 1.5 km. The current density profile derived from this ΔF curve is smoothed using a 3 point moving average. For Rb. magnetometer, the ΔF curves are plotted using the high density data and the smoothing is done with the help of the computer. The current density profiles are then derived from these ΔF profiles.

Because of the precession effects, the current density profiles might show subsidiary peaks above the main electrojet layer. Interpretation of these peaks is difficult without additional information from other independent supporting experiments, preferably from experiments whose results are not spin and precession dependant. These subsidiary peaks occur at regular time intervals than at altitude intervals indicating that they are due to the precession effect. Correct identification and correction of these effects are important as there is the possibility of these being mistaken for the effects of currents flowing in different layers and different directions.

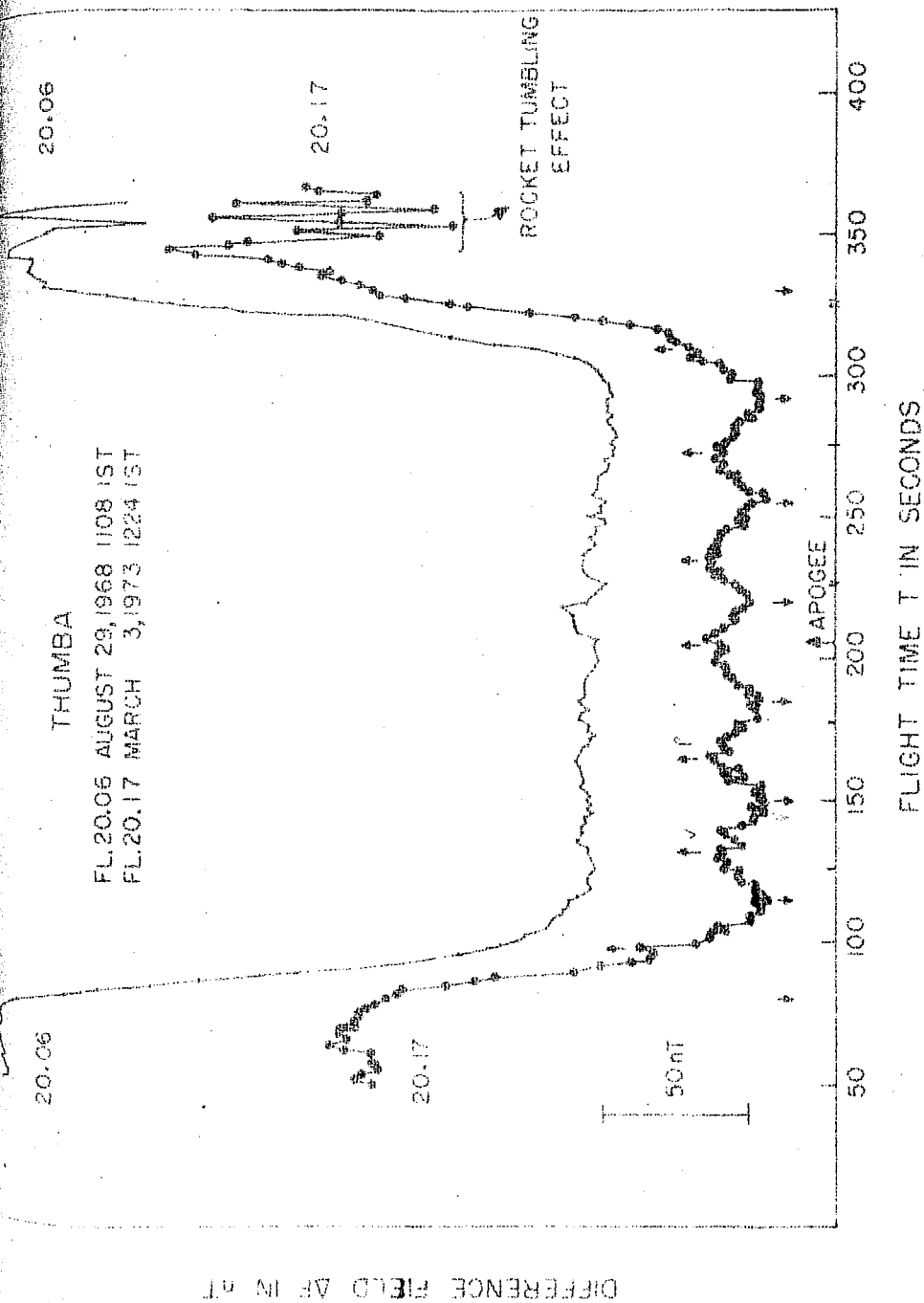


FIG. 3.4. The figure shows the modulation of ΔF profiles of Fl. 20.06 and 20.17, by the payload field due to rocket precession. Payload 20.06 was nearly magnetically clean, hence shows negligible precession effect, whereas Fl. 20.17 shows large precession effect due to larger pollution field from the payload. The modulation because of precession, if any, is removed from the ΔF profiles and the precession free ΔF profiles are used for evaluating the J profiles.

As was explained in Chapter 1, the two important aspects of the quiet day geomagnetic variations viz. the diurnal variation and its day-to-day variability, have been studied extensively by various investigators using ground magnetic data. A preliminary study of these two aspects by in-situ measurements has been done by Sastry (1970) and Sampath and Sastry (1976). In order to understand the nature and the reason for the observed large diurnal and day-to-day variations of the geomagnetic field, it is necessary to study the diurnal and day-to-day variability of the electrojet parameters and the relationships of the variations of these parameters to the observed magnetic variations at the ground. A detailed study involving both the rocket-borne and the ground based magnetic measurements is the subject matter of this chapter. The rocket experiments were conducted from Thumba on magnetically quiet days. A chain of ground magnetic stations was set up in the electrojet region to support the rocket measurements. The results of these experiments are discussed in this chapter in the following manner.

Section 4.1 deals with the study of the diurnal variation of the electrojet parameters and in section 4.2 the day-to-day variability of the electrojet parameters is discussed. With the availability of large amount of rocket data from a single station, Thumba, and based on the results of section 4.1 and 4.2, the possibility of predicting the vertical distribution of current density in the electrojet, at any instant on a magnetically quiet day, given the day's magnetogram has been examined in section 4.3. In this connection, the effect of the stabilisation of the two stream instability on the vertical distribution of current density is also discussed.

A simple Chapman-McNish type induction model has been used to relate the ground magnetic field change at the time of rocket launch, with the rocket measured electrojet strength. From this the ratio, $H(\text{internal})/H(\text{external})$ is obtained for the region around Thumba. These results are presented in section 4.4.

4.1 Diurnal variation:

To study the diurnal variation in the electrojet parameters, three rocket magnetometer flights were conducted during the course of a single day, from Thumba. The day was magnetically quiet. This helps in relating the rocket

measured electrojet strength and the ground ΔH without much ambiguity, since the non-ionospheric contribution to ground ΔH on quiet days is expected to be negligible.

4.1.1 Flight details:

Three Nike-Apache rockets (FL. 20.06, 20.07 and 20.08) carrying proton precession magnetometers were launched from Thumba, on August 29, 1968. The rockets were launched at an azimuth of 270° and an elevation of 85° . The rockets carried similar payloads and reached an apogee of about 173 km. The vehicles were tracked by the radar on the skin-track mode upto an altitude of 60 km. The trajectory for these flights were computed by theoretical means, as discussed in chapter 3. The day was magnetically quiet with an A_p index of 1.

The first flight 20.06, was launched at 1108 hrs IST, near the maximum of H variation observed at the ground and when the ground ΔH was 110 nT, from the mid-night level of H variation. The second flight 20.07 was conducted at 1415 hrs IST, during the decay phase of the diurnal variation. The ground ΔH was 58 nT, at the time of launch. The third flight 20.08 was conducted an hour before local mid-night, at 2300 hrs IST. There was no appreciable ΔH at the time of launch of this flight. The magnetogram of the Trivandrum observatory for the day of these flights is shown in Fig. 4.1. The launch timings are indicated in the figure.

TRIVANDRUM MAGNETOGRAM
1968 AUGUST. 29⁰ 06⁰ 33⁰⁰ TO 30⁰ 08⁰ 30⁰⁰ IST.

H: BASE LINE VALUE = 38500 nT
FLIGHT 20.06 11.08 15T.
" 20.07 14.15 15T.
" 20.08 23.00 "

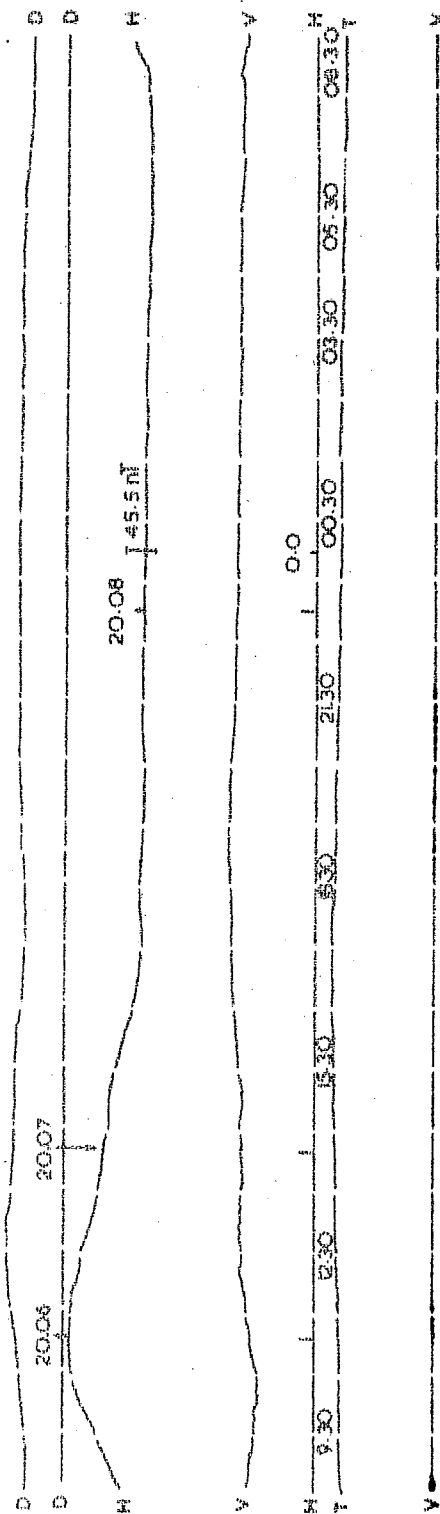


FIG. 4.1. The H, Z and D variations recorded at the Trivandrum observatory, from 0833 hrs IST on 29 August 1968 to 0830 hrs IST on 30 August 1968. The launch times of Fl. 20.06, 20.07 and 20.08 are indicated in the figure.

4.1.2 Flight results:

Good data was recovered from all these three flights during ascent as well as descent. The difference field (ΔF) profiles derived from these flights during the ascent and the descent are shown in Fig. 4.2. From this figure it can be noted that the data from flights 20.06 and 20.08 are quite good with negligible precessional modulations. The data from the flight 20.07 is modulated due to the payload field and the coning of the rocket. The large modulations seen in the descent curves below 80 km are due to the rocket tumbling during reentry. The three ΔF profiles of the ascent, cross each other at $\Delta F = 0$ but not the descent ones. This is due to a slight difference between the trajectory obtained by theoretical computation and the actual descent path followed by the rocket. The current density profiles derived from the ΔF curves of Fig. 4.2., are shown in Fig. 4.3.

Flight 20.06 magnetometer detected a departure field of 210 nT between 90 and 130 km ($\Delta F = \pm 105$), as the magnetometer traversed the electrojet. As the magnetic field below an idealised current sheet is of the same magnitude but opposite in sign, to the field above the sheet, the field just below the sheet will be half of 210 nT, i.e. equal to 105 nT. The current density curves of Fig. 4.3 show that appreciable currents flow between 90 and 130 km with a peak

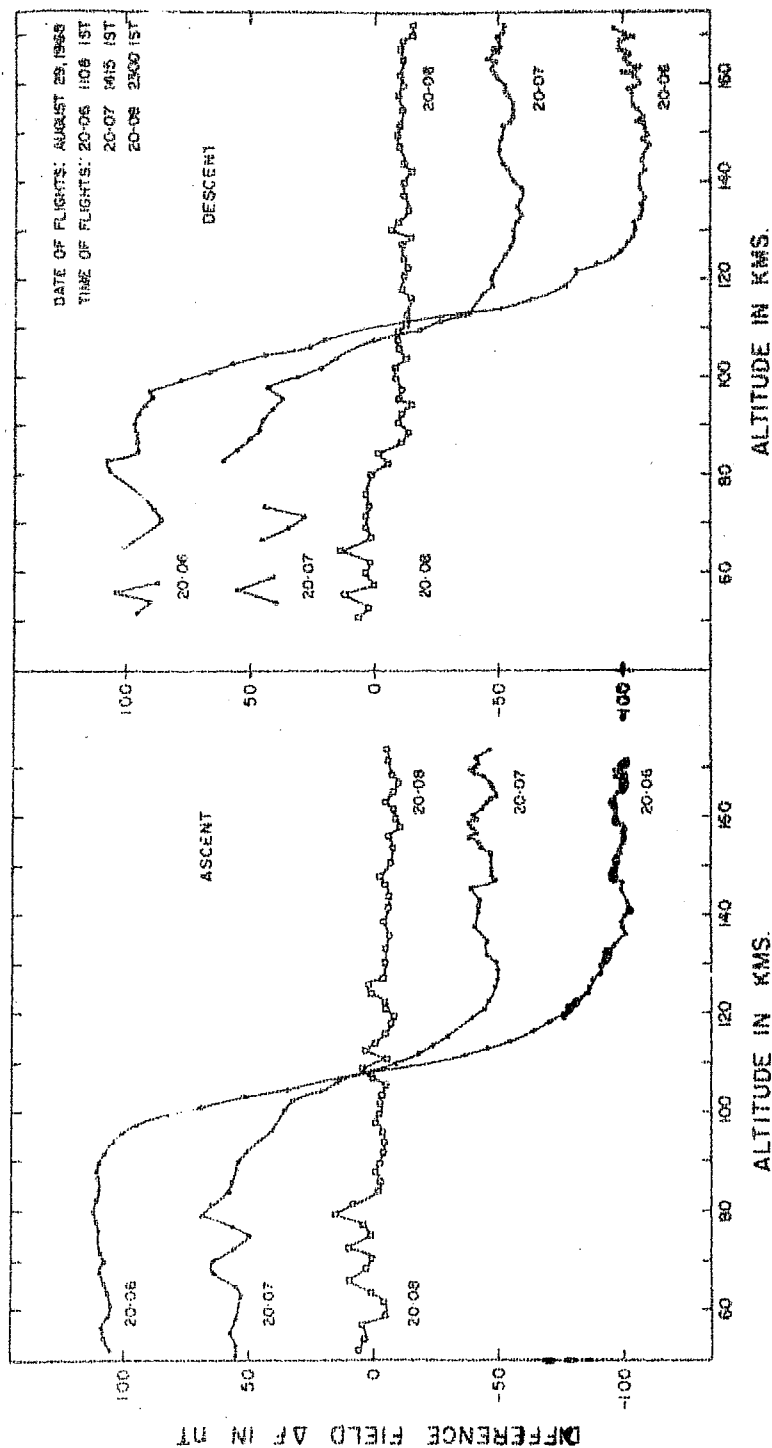


FIG. 4.2. The difference field $\Delta F = (F - F_T)$ as a function of altitude is shown for the three flights 20-06, 20-07 and 20-08. F is the rocket measured field in these flights and F_T is the theoretically computed field using Jensen and Cain (1962) coefficients of 1960 corrected for secular variation for the flight epoch. The ΔF profiles for the ascent and the descent portion of the flights are shown separately. The large modulations in the ΔF curves below 80 km in the descent are due to rocket tumbling during re-entry.

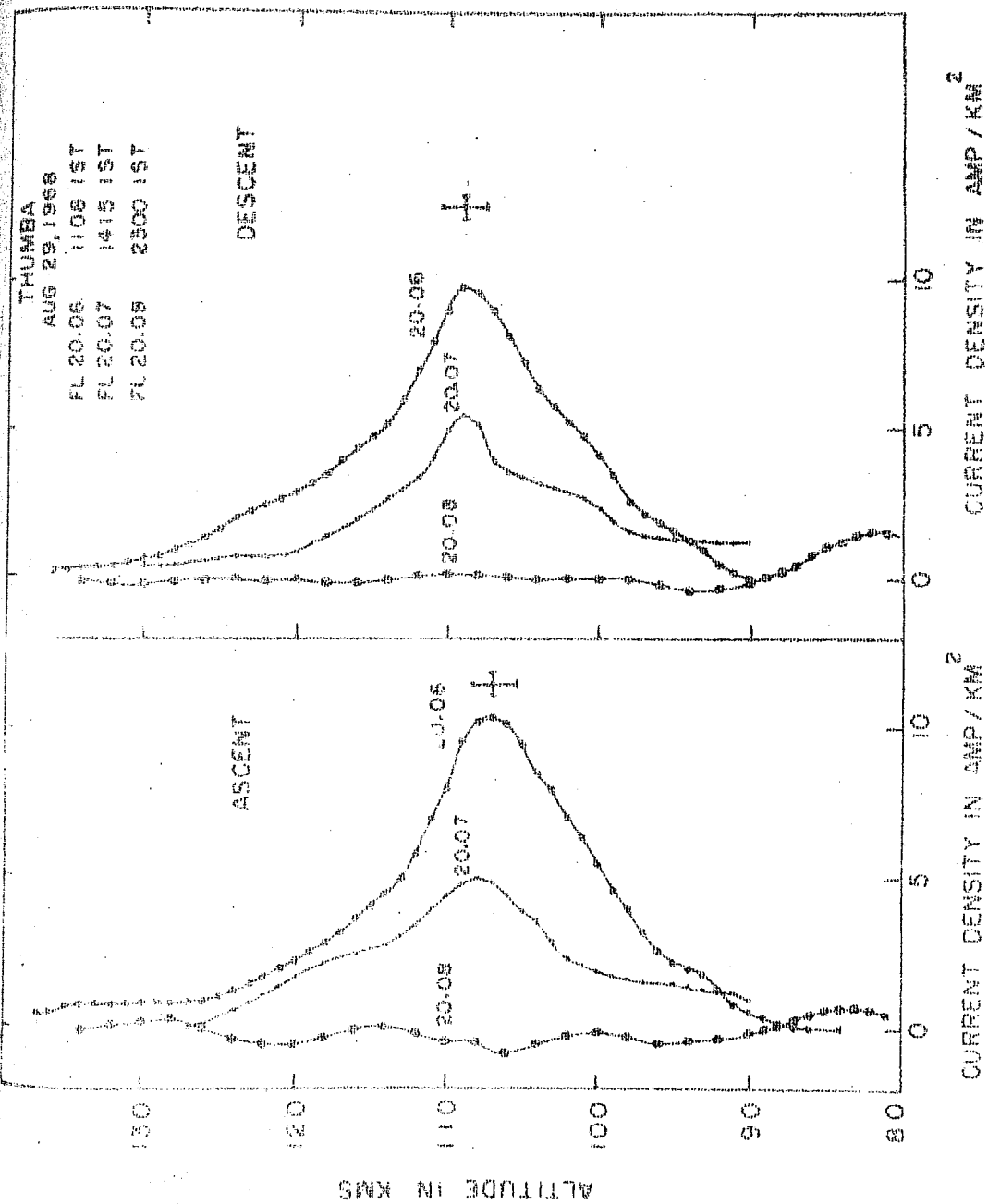


FIG. 4.3. The vertical distribution of electrojet current density measured during the magnetometer flights 20.06, 20.07 and 20.08. The current density curves are derived from the respective AP profiles of fig. 4.2.

at 107 ± 1.5 km altitude. The maximum current density measured during this flight is 10.4 ± 0.4 Amp/km². The half thickness of the current layer is about 12 ± 1 km.

Flight 20.07 magnetometer detected a departure field of 100 nT between 90 and 130 km. Appreciable currents were detected between 90 and 130 km with a peak at 108 ± 1.5 km altitude. The maximum current density measured is 5 ± 0.4 Amp/km², with a half thickness of the current layer equal to 15 ± 1 km.

Flight 20.08 did not detect any significant departure between 90 and 130 km.

4.1.3 Discussion of flight results:

From the Trivandrum magnetogram (Fig. 4.1) it can be seen that the ground ΔH decayed from 110 nT at the launch time of FL. 20.06 to 58 nT at the launch time of FL. 20.07. The rocket measured electrojet strength decayed from 105 nT to 50 nT in the same interval. The change in the ground ΔH is about $58/110 = 53\%$, while in the electrojet strength is about $50/105 = 47.6\%$. Assuming that the width of the jet did not change significantly in this small interval of time, this result shows that the electrojet currents decayed a little faster than the ground ΔH . This could be probably due to a small phase difference between the electrojet current

and the decay of its induced image currents underground. This phase difference is however small. Hence, it can be safely concluded that the electrojet strength on a quiet day, follows the ground magnetic variation, rather closely.

The current density curves of FL. 20.06 and 20.07 in Fig. 4.3, show that in the noon as well as in the afternoon, measurable currents flow only between 90 and 130 km, indicating that the vertical extent of the current layer does not change significantly during the course of a day.

The half thickness of the current layer, deduced from Fig. 4.3 shows that the electrojet in the afternoon was $(15 \pm 1 \text{ km})$ broader, compared to the noon time electrojet layer $(12 \pm 1 \text{ km})$. This could be due to the fact that the data of flight 20.07 was modulated by precessional effects. It can be clearly seen that due to the same effect the descent current density curve of 20.07 appears much narrower. Taking the average of the ascent and the descent current density curves of 20.07 and normalising the peak of the average curve to the peak current density of FL. 20.06, shows that the afternoon profile follows the noon profile closely. This shows that the thickness of the layer and the current distribution in the layer does not change significantly from noon to afternoon.

It can also be seen from the current density profiles of Fig. 4.3 that the altitude at which the current density maximises does not change significantly from noon to afternoon. Incidentally, it is significant, that the experimentally measured current density peaks at an altitude (106 km) distinctly above that of cowling conductivity σ_3 peak (100 km), calculated by using ionospheric parameters from models, as has been done by several workers. This is evident from the comparison of Fig. 1.2 of chapter 1 with Fig. 4.11 b of this chapter.

The night time flight 20.08 did not detect any significant departure field, between 90 and 130 km. The current density distribution measured in FL. 20.08, (in Fig. 4.3) exhibits small fluctuations about the zero value from 90 and 136 km altitude. This indicates the absence of any current in either direction eastward or westward, in this region. Evidences for the westward flow of electrojet currents in the night time E-region are available from the rocket measurement of Davis et. al., (1967) and from the ground based back scatter studies of Balsley (1965). No significant currents in the night time E-region were detected by Maynard and Cahill (1965) and Shuman (1970). The experimental result from flight 20.08 also indicates that no significant current flows in the night-time E-region, on a magnetically quiet day. A departure of about 10 nT was detected between 80 and

90 km, in this flight 20.08, Sastry (1971). However, there was no corresponding departure in H variation record at the ground to support this change and also there is no independent supporting evidence to prove that the observed departure is due to nighttime currents in this low altitude region. The diurnal variation of electrojet parameters, as observed by the rocket-borne magnetometers is summarised in table 4.1.

4.2 Day-to-day variability:

The diurnal variation of geomagnetic field exhibits large changes of amplitude from one day to another, even on apparently quiet days. A number of causes of ionospheric origin and magnetospheric origin have been attributed to this day-to-day variability. The investigation, the details of which are presented here, is particularly directed towards understanding the relative importance of these two factors in causing the day-to-day variability. For this investigation, two rocket magnetometer flights were conducted near local noon, from Thumba, on two closely spaced days in April 1971. On one of the days, the diurnal amplitude of H variation was small and on the other, it was unusually large. This experiment was repeated in February 1972.

4.2.1 Experimental details and results:

The details of launching of the April '71 and February '72 series of experiments are shown in Table (4.1). The variations of the horizontal component of the magnetic field recorded at different ground support stations for April '71 launching is shown in Fig. 4.4 and for February '72 launchings in Fig. 4.5. The time of launchings are indicated in the figures. The H variation on February 2, 1972 was quiet before and during the flight. The three hourly K_p index for the interval of actual flight was only 3+. Two hours after the launch, the day became slightly disturbed. Due to this, the overall A_p index for the day increased to 13. Hence, it can be said that the periods during which the four experiments were conducted were exceptionally quiet.

Good data was obtained from the two April '71 flights, during both the ascent and the descent. The difference field (ΔF) profiles obtained from FL. 20.11 and 20.12 are shown in Fig. 4.6. It can be seen that the data from 20.11 is modulated due to rocket precession. The 20.12 data is not modulated to the same extent, because this payload was magnetically clean compared to the payload of FL. 20.11. The current density curves derived from the mean of ascent and descent ΔF curves are shown in Fig. 4.8.

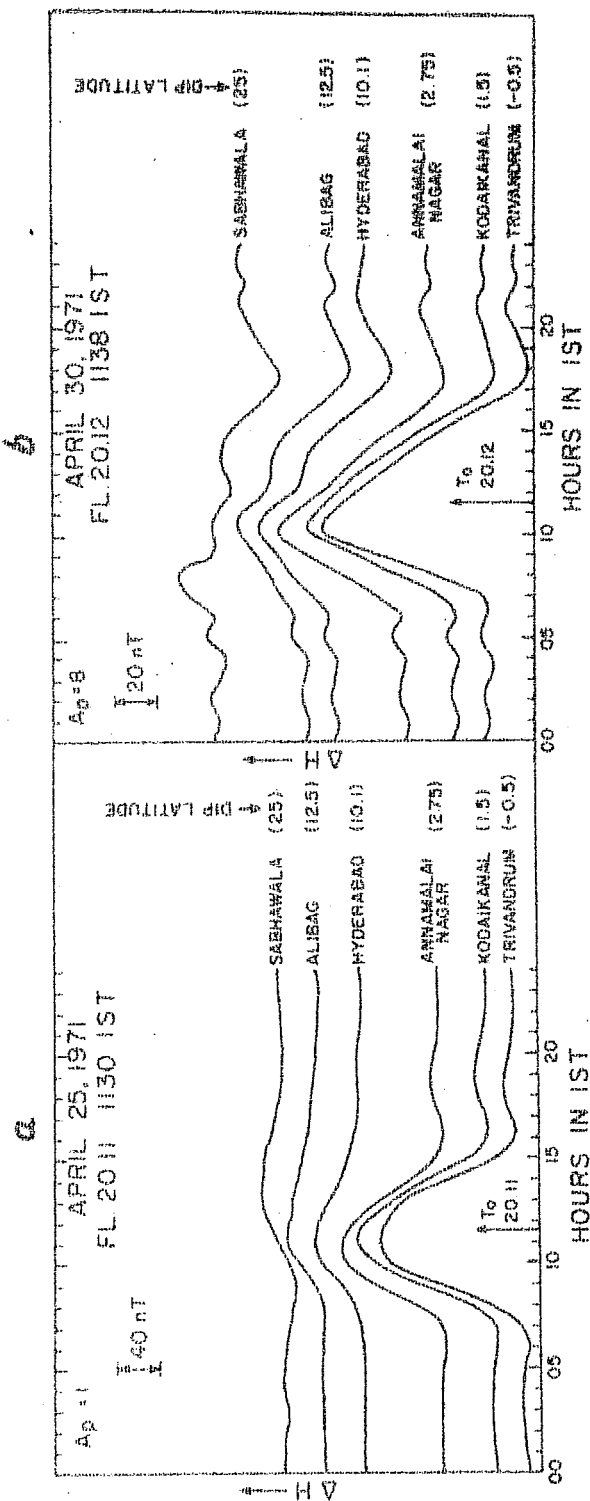


FIG. 4.4. The H variations recorded at the magnetic observatories in the Indian zone on April 25, 1971 and April 30, 1971. The launch time (T_0) of the flights 20.11 on April 25, 1971 and 20.12 on April 30, 1971 are indicated in the figure. Hourly values are used in these plots. The dip latitudes of the observatories are shown in the brackets. Note that the ΔH scale for the curves (a) is double of that for (b).

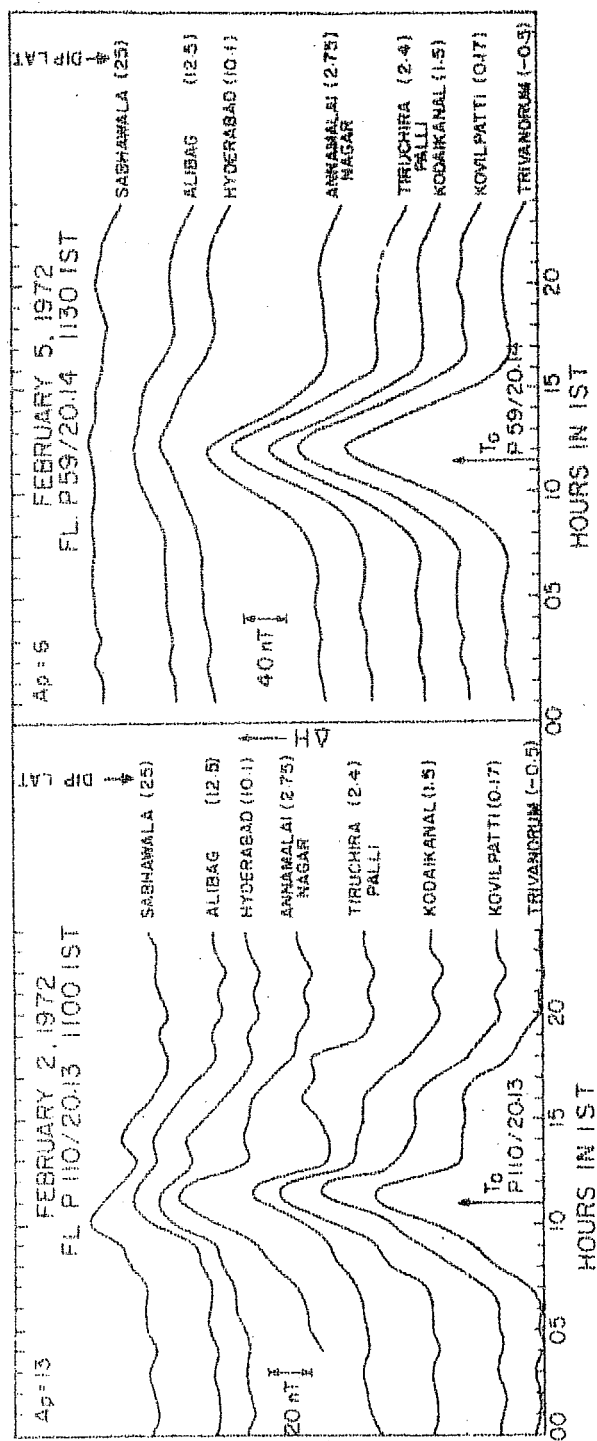


FIG. 4.5. The H variations recorded at the standard magnetic observatories and at the temporary ground magnetometer stations (Kovilpatti and Tiruchirappalli) in the Indian zone on February 2, 1972 and February 5, 1972. The launch time (T_0) of the flight P110/20.13 on February 2, 1972 and P59/20.14 on February 5, 1972 are shown in the figure. Hourly values are used in these plots. The scale for February 5 curves are twice that for February 2 curves.

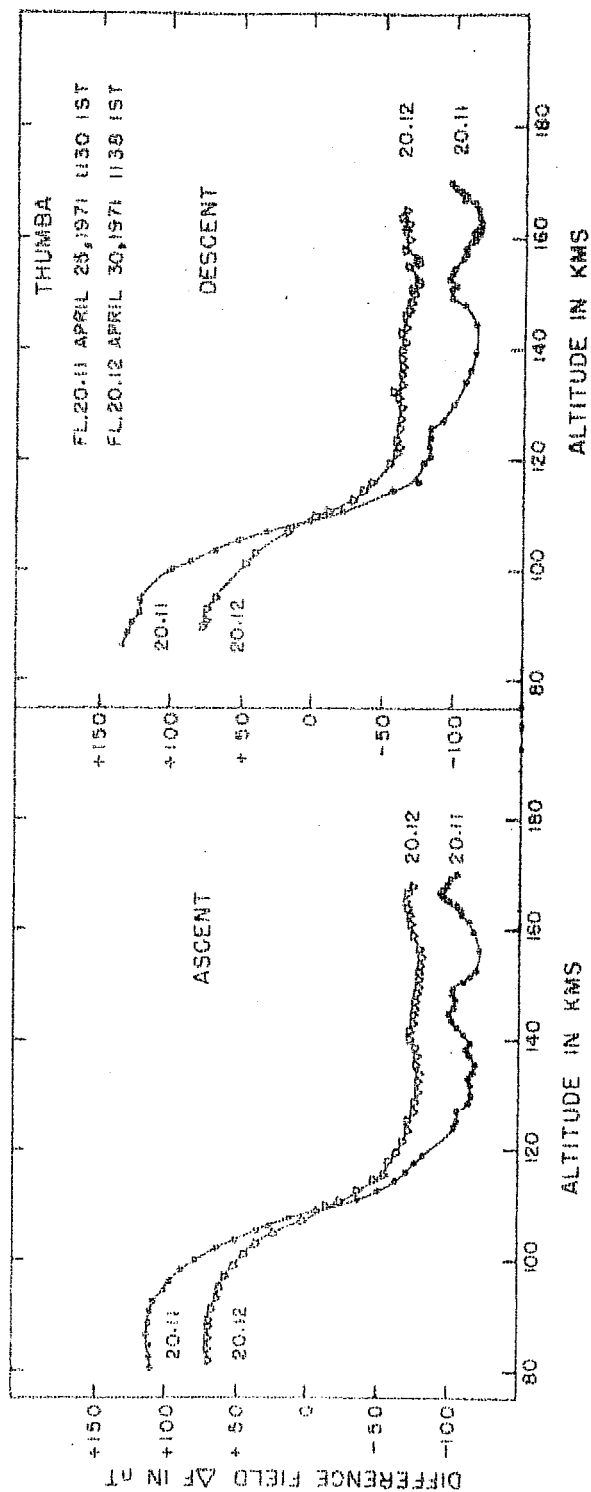


FIG. 4.6. The difference field $\Delta F = (F - F_T)$ profiles as a function of altitude, derived from the F measurements of Fl. 20.11 and 20.12. Jensen and Cain (1962) coefficient of 1960 are used to derive the F_T values, after correcting for secular variation for the flight epoch.

As regards the February 1972 flights, P110/20.13 gave intermittent data during both the ascent and the descent, due to the rocket magnetometer entering the dead zones during the rocket precession period. However, it can be seen from the ΔF profiles of this flight, P110/20.13 (Fig. 4.7) that the dead zones during the ascent coincides with the good data periods in the descent and vice versa. This helped in the recovery of good data throughout the flight. Fl.P59/20.14 did not have this problem. It gave good data during both the ascent and the descent. The ΔF profiles obtained during this flight are shown in Fig.4.7 along with that of Fl. P110/20.13. The current density curves for these two flights derived from the average of the ascent and descent ΔF curves of Fig. 4.7 are shown in Fig. 4.8 separately.

4.2.2 Discussion of Results:

The important parameters of equatorial electrojet (EEJ) measured during the two series of experiments have been summarised in table 4.1. It can be seen from the integrated current density measured during these flights, that the flights 20.11 and 20.14 encountered strong electrojets whereas flights 20.12 and 20.13 encountered comparatively weaker electrojets. Neither the layer thickness nor the altitude of J_{\max} changed significantly from low jet day to the high

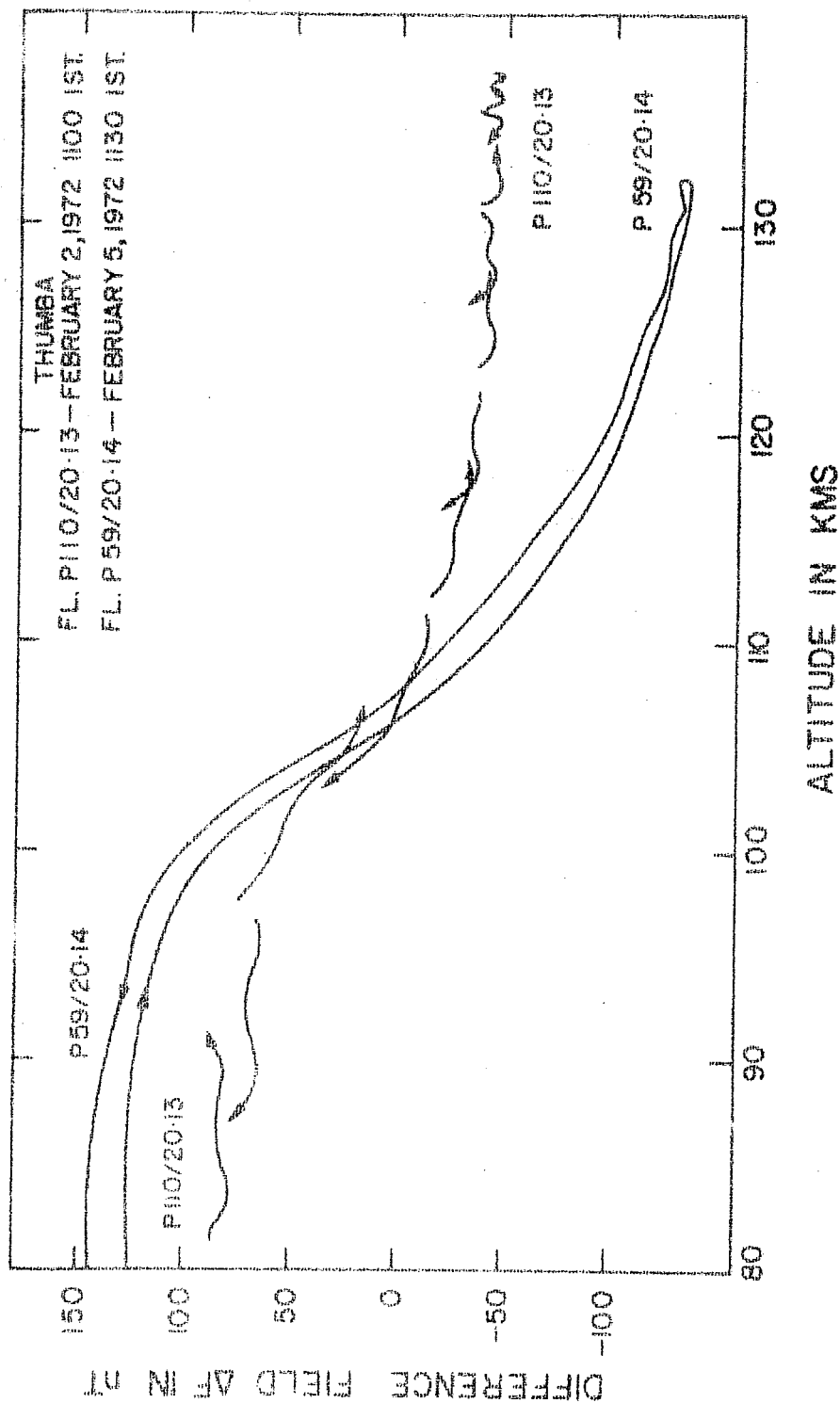


FIG. 4.7. The difference field $\Delta F = (F - F_T)$ profiles as a function of altitude, derived from the F measurements of Fl. P110/20.13 and P59/20.14. Jensen and Cain (1962) coefficients of 1960 are used to derive the F_T values, after correcting for secular variation for the flight epoch. Note that the loss of data in the ascent portion of the flight P110/20.13 coincides with the presence of good data in the descent and vice versa.

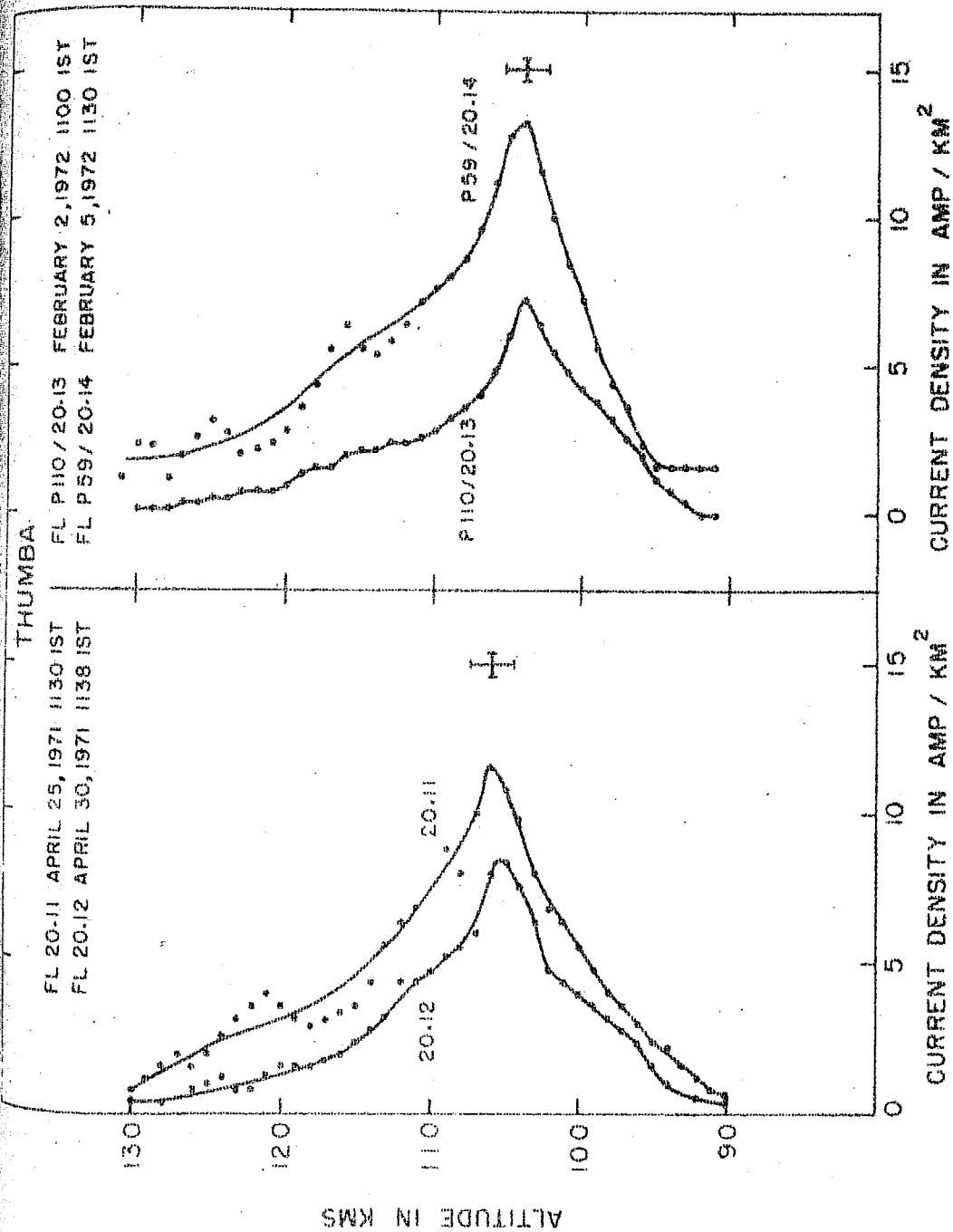


FIG. 4.5. The vertical distribution of electrojet current density derived from the slopes of the ΔF curves in figs. 4.6 and 4.7. These current curves are derived from the mean of the ascent and the descent curves. The modulations seen in the current curves are due to rocket precession and are smoothed out as shown.

jet day. The current density curves of Figure 4.8 show that the vertical extent of the current layer does not change appreciably from one day to another and remains within 90 and 130 km. Normalising the peak current density of Fl.20.11 to that of Fl. 20.12, it is seen that the two current density profiles follow each other within the limits of experimental error. Same is the case with the J profiles of Fl.20.13 and 20.14. This shows that the vertical distribution of current density in the EEJ does not change significantly from the low jet day to a high jet day. Further it is seen from the table 4.1 that the width of the jet on the low jet day of Fl. 20.12 was somewhat larger than that in the high jet day of 20.11, but the reverse is the case with flights 20.13 and 20.14. This observation and some other observations concerning the effect of variation of the width of EEJ, that will be discussed later in this chapter (section 4.4), show that the observed changes in the width of EEJ cannot account for the large enhancement of ΔH observed on high jet days.

The above observations show that change in the parameters of the EEJ such as the altitude of J_{\max} , EEJ layer thickness, the width of the jet, the vertical extent of the current layer and the distribution of the current in the layer cannot account for the large day-to-day changes of the amplitude of H variation observed at the ground on quiet days.

Fl.No.	Launch Date	Time IST	A_p	ΔH_{Tri} nT	F_R nT	J_p A/km ²	$\int J dh$ A/km	h km	t km	W km
20.06	29.8.68	1108	1	110	210	10.4 ± 0.4	160	107 ± 1.5	12	307
20.07	"	1415	1	58	100	5 ± 0.4	80	108 ± 1.5	~ 12	275
20.08	"	2300	1	-	-	-	-	-	-	-
20.11	25.4.71	1130	1	120	220	11.6 ± 0.4	164	106 ± 1.5	12	300
20.12	30.4.71	1138	8	80	145	8 ± 0.4	104	106 ± 1.5	12	317
20.13	2.2.72	1100	13	75	135	7.2 ± 0.4	92	104 ± 2	12	300
20.14	5.2.72	1130	6	135	260	13.2 ± 0.4	172	104 ± 2	12	340

TABLE 4.1. Diurnal and day-to-day variability of the electrojet parameters, as observed by rocket-borne magnetometers over Thumba.

F_R is (ΔF_{90} km - ΔF_{130} km); J_p is the peak current density in amp/km²; $\int J dh$ is the height integrated current density in amp/km; h is the altitude of (J_p) the current density peak t is the half-thickness of the electrojet layer and W is the half width of the electrojet.

Again, from table 4.1, it is seen that the ground ΔH_{Tri} at the time of launch of Fl. 20.11 was 1.5 times the ground ΔH_{Tri} at the time of launch of Fl. 20.12. The electrojet strength measured by 20.11 as given by ΔF value is also 1.5 times the electrojet strength measured by Fl. 20.12. The height integrated current densities measured during these flights also bear the same ratio 1.5. This means that the strength of the electrojet actually measured during these flights was proportional to the ground ΔH observed at the time of the flights. The data from Fl. P110/20.13 and P59/20.14 further confirm these findings. It can be seen that the ratio of the ground ΔH_{Tri} at the time of launch of P110/20.13 to that of P59/20.14 is 1.8 and the ratio of rocket measured electrojet strength is 1.9. Corresponding height integrated current density ratio is 1.87 which is not very much different from the ground ΔH_{Tri} ratio of 1.8.

It can be seen further that though the A_p index changes from high jet day to the low jet day, (from 1 to 8 in the case of 20.11 and 20.12 and from 6 to 13 in the case of P59/20.14 and P110/20.13), the ratio of electrojet strength of high jet day to the low jet day is the same as the ratio of corresponding ground ΔH . This shows that non-ionospheric factors did not affect the current density in the EEJ on these days. Hence the large ΔH seen at the time of launch

of Fl. 20.11 and P59/20.14 must be due to increased strength of the EEJ itself. Also, since the current density profiles of the high jet days as well as the low jet days of Figure 4.8 show single layer structure, the day-to-day variability of the EEJ intensity and consequently the variability of H component at the ground should be fully explainable by a single layer EEJ alone. In other words, at least, as far as the results from the above four flights are concerned, there is no need to postulate the formation and disappearance of additional current layers to explain the observed large day-to-day variability of the H amplitude.

Since from the above discussions it is evident that on magnetically quiet days, the electrojet is the only source of day-to-day variability of H amplitude and since this variability cannot be accounted for by the apparent changes the EEJ parameters already mentioned, the important ionospheric parameters that can cause the large changes in the EEJ strength from one day to another must be identified. The two known sources that can bring about large changes in EEJ current density are (1) the winds (both global and local) that control the electric fields in the region of the electrojet and (2) the electron density that controls the ionospheric conductivities. Day-to-day changes in the electron density in the region of the electrojet is well understood,

but it is known from ground based investigations, for instance Kane (1972), that day-to-day electron density changes are not well correlated with the day-to-day changes in the amplitude of H variation. Thus, the day-to-day variability of the ionospheric conductivities controlled by electron density changes may not be the major source of day-to-day variability of H variation. This leads us to investigate the winds and electric fields as the primary source of H variability, as suggested by Dunford (1967), Akasofu et. al., (1969), Matsushita (1973) and many others. Since our results show that certain parameters of EEJ such as, the vertical distribution of current density, altitude of J_{\max} and vertical extent of current layer do not change drastically from a low jet day to a high jet day, the electric fields responsible for the day-to-day variability may exhibit large day-to-day variability in intensity but not in its vertical distribution. To test this hypothesis and to establish that winds and electric fields alone are responsible for large day-to-day variability of ground H variation amplitude, what is needed is the simultaneous measurement of the EEJ current density, electron density, electric field and day time winds over the equator on normal, low and high jet days.

4.3 Prediction of vertical profile of current density on a quiet day:

From the results presented in Sec. 4.1 and 4.2, it is seen that on quiet days, irrespective of the strength of EEJ,

the lower and upper boundaries of the electrojet layer remain at 90 and 130 km respectively and the peak of current density stays at 106 ± 1.5 km altitude. Further, the strength of EEJ is proportional to the ground ΔH and the vertical distribution of current density remains unaltered. These results and the data from several other quiet day measurements on the EEJ presented in this section and summarised in Figures 4.11a and 4.11b suggest that it is possible to predict the vertical distribution of current density in the EEJ for any time of a quiet day, given the H variation data from a station under the jet.

Fig. 4.11a shows the relation between ground ΔH_{Tri} and the peak current density measured in 9 rocket flights conducted from Thumba. It can be seen that there is a linear relationship between ΔH and J_{max} . Most of the flights were conducted on magnetically quiet days ($A_p < 10$). The line of least square fit giving the relation between ΔH and J_{max} passes through the origin showing that the non-ionospheric contribution to ΔH changes was negligible on these days.

Figure 4.11b shows the current density distributions obtained from all the noon time rocket magnetometer experiments from Thumba, after normalising their peak current density values to 10 amp/km^2 . It can be seen from the mean curve, that the electrojet current density maximises at 106 km

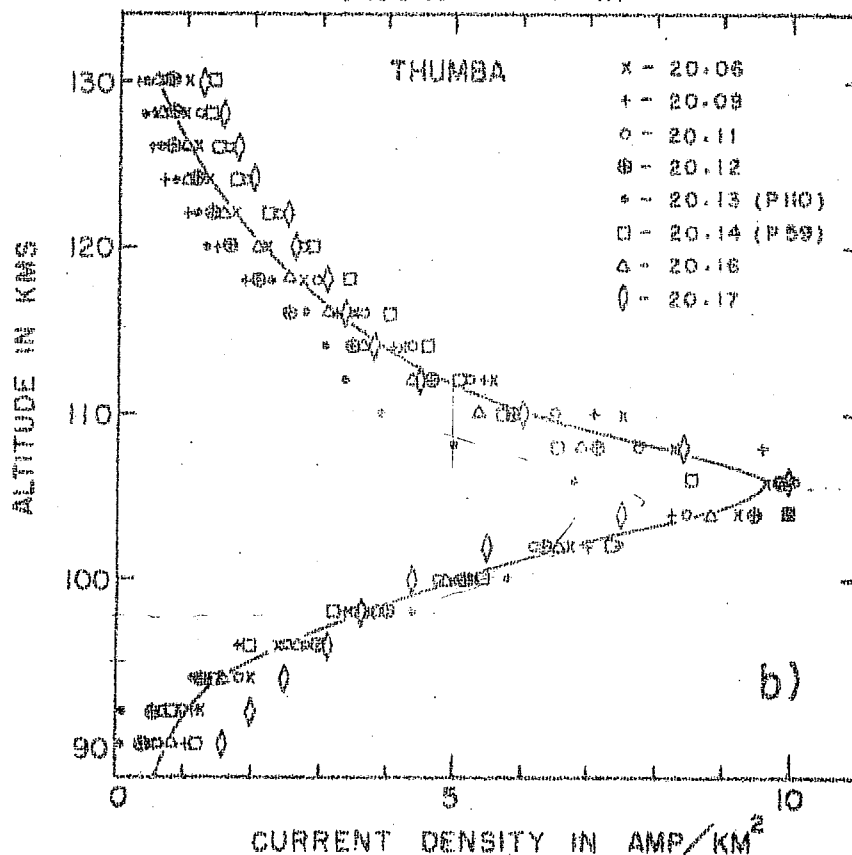
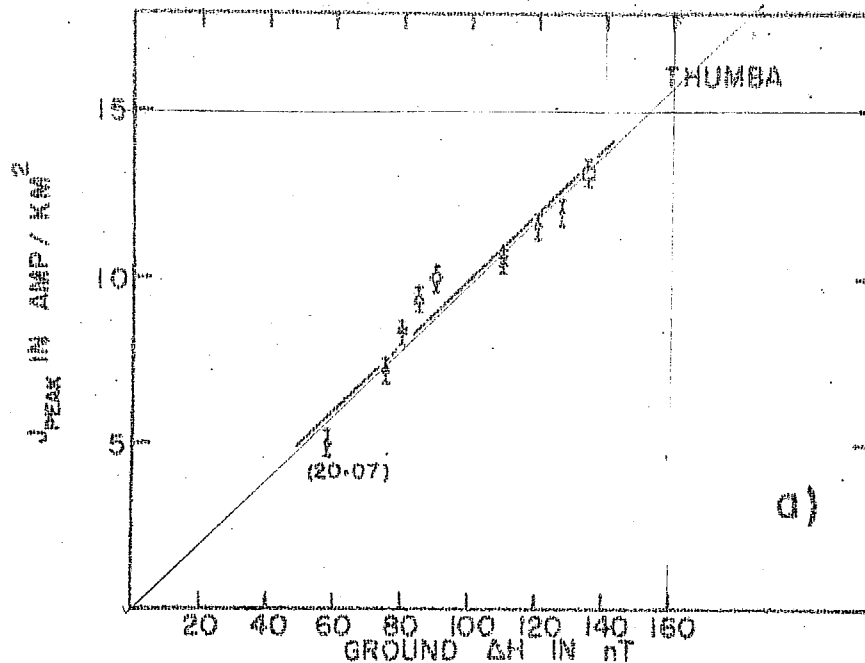


FIG. 4.11. a) The maximum current density measured (J_{peak}) during the rocket magnetometer flight is shown against the ground ΔH at the launch time of the rocket, for several flights conducted from Thumba. They show a linear relation, with a positive slope of 0.1.

b) The vertical distribution of current density measured during eight noontime flights from Thumba, after

altitude and the current layer has a thickness of 12 km (100-112 km) at half power points. The peak current density of 10 amp/km^2 corresponds to a ΔH of 100 nT at the ground, as can be seen from Fig. 4.11a. The current density values, for the mean curve (J^*) shown in Fig. 4.11b for the altitude range of 90 to 130 km, are listed in table 4.2, together with the standard error. From the tabulated values of J^* , the current density value for any given ΔH can be obtained from the relation,

$$J(h) = J^*(h) \frac{\Delta H}{100} \quad (\text{where } h \text{ is the altitude}).$$

The scatter around this curve is less than $\pm 1 \text{ amp/km}^2$. The curve represents fairly accurately the current distribution in the jet on magnetically quiet days. The scatter is mainly due to the experimental errors involved in the measurement of current density, the behaviour of the rocket in each experiment whose data has been used here and small changes in the parameters of electrojet. In the next section 4.4, the changes in the width of the electrojet during these experiments have been examined. The width appears to have remained within $300 \pm 40 \text{ km}$ in all the cases except Fl. 20.09. The width varying within these limits might have contributed to the scatter, but has not significantly affected the vertical profile of current density. This means that changes in jet

Altitude (h) km	J^* amp/km ²	σ	Altitude (h) km	J^* amp/km ²	σ
90	0.73	0.48	112	4.84	0.76
92	1.04	0.58	114	3.91	0.46
94	1.58	0.45	116	3.30	0.47
96	2.53	0.45	118	2.62	0.54
98	3.74	0.35	120	2.10	0.56
100	5.08	0.40	122	1.73	0.56
102	6.68	0.67	124	1.37	0.55
104	8.93	0.83	126	1.07	0.51
106	9.34	1.13	128	0.77	0.43
108	7.52	1.47	130	0.87	0.45
110	6.11	1.24			

TABLE 4.2. Tabulated values of current density J^* in the electrojet for different altitudes, based on the mean curve of Fig. 4.11b. The standard error σ , showing the possible departure of the tabulated values from actually measured current density values are also shown. The current density (J) for any given ΔH can be obtained from these J^* values using the relation,

$J(h) = J^*(h) \cdot \Delta H/100$. The J^* values are normalised for $\Delta H = 100$ nT and hence the division by 100 on the R.H.S.

Note:- In normalising the J profiles, only the peak values of J are normalised and not the altitude at which they peak. This gives more scatter near and around the peak (as seen from the σ values), as the J profiles peak at slightly different altitudes between 104 and 108 km. More number of flights peak at 106 km and hence the pronounced peak at this altitude.

width might change the intensity of the jet but not the vertical profile of current density distribution in the jet.

Rogister (1971) and Sato (1972) have suggested that the current density distribution in the EEJ will be modified on high jet days due to stabilisation of the two stream instability. If the mechanism suggested by Rogister and Sato does operate, then the prediction of the vertical profile of current density proposed here by invoking the proportionality between ΔH and J_{\max} will not be valid. We have examined this problem with the available data from in-situ measurements. It may be recalled that type I irregularities are generated in the electrojet region when the electron drift velocity V_d exceeds the threshold, which is the ion acoustic velocity C_s in the medium. C_s is about 360 meters/sec in the E region. The ground based radar studies show that the drift velocities of the irregularities, as obtained from doppler shift of backscatter radar echo from the type I irregularities, remain close to the C_s value even when the electrojet strength is quite high, as seen from large diurnal amplitudes of the geomagnetic field variation at the ground. Rogister and Sato have explained this observation by suggesting that the stabilisation of two stream instability will restrict the peak current density in the electrojet to such a value that electron drift velocity does not exceed the threshold, and

at the same time the height integrated current density in the electrojet remains unaltered, so that the total current in the EEJ can account for the magnetic field variation observed at the ground. If this mechanism is operative, one would expect redistribution of current density in the jet on high jet days in such a way that the J profile will show a reduced but broader maximum and larger thickness for the current layer. Whether this mechanism really becomes operative or not, cannot be tested by ground based observations. It needs in-situ measurements.

The flight P59/20.14 measured the highest peak current density of all the magnetometer flights from Thumba so far. The peak current density measured in this flight is 13.2 amp/km². The ΔH value at the time of this flight was 135 nT. The current density profile for this flight is shown in Fig.4.9 together with a noon time, rocket measured electron density profile. The drift velocity derived using the relation $V_d = J/N_e e$, where V_d is the electron drift velocity, J is the current density, N_e is the electron density and 'e' the electronics charge, is also shown in the Figure 4.9. It can be seen that the drift velocity V_d exceeded the threshold velocity 360 m/sec, between 100 and 106 km altitude and reached a peak value of 500 m/sec. Neither the flattening due to reduction of peak current density nor signs of

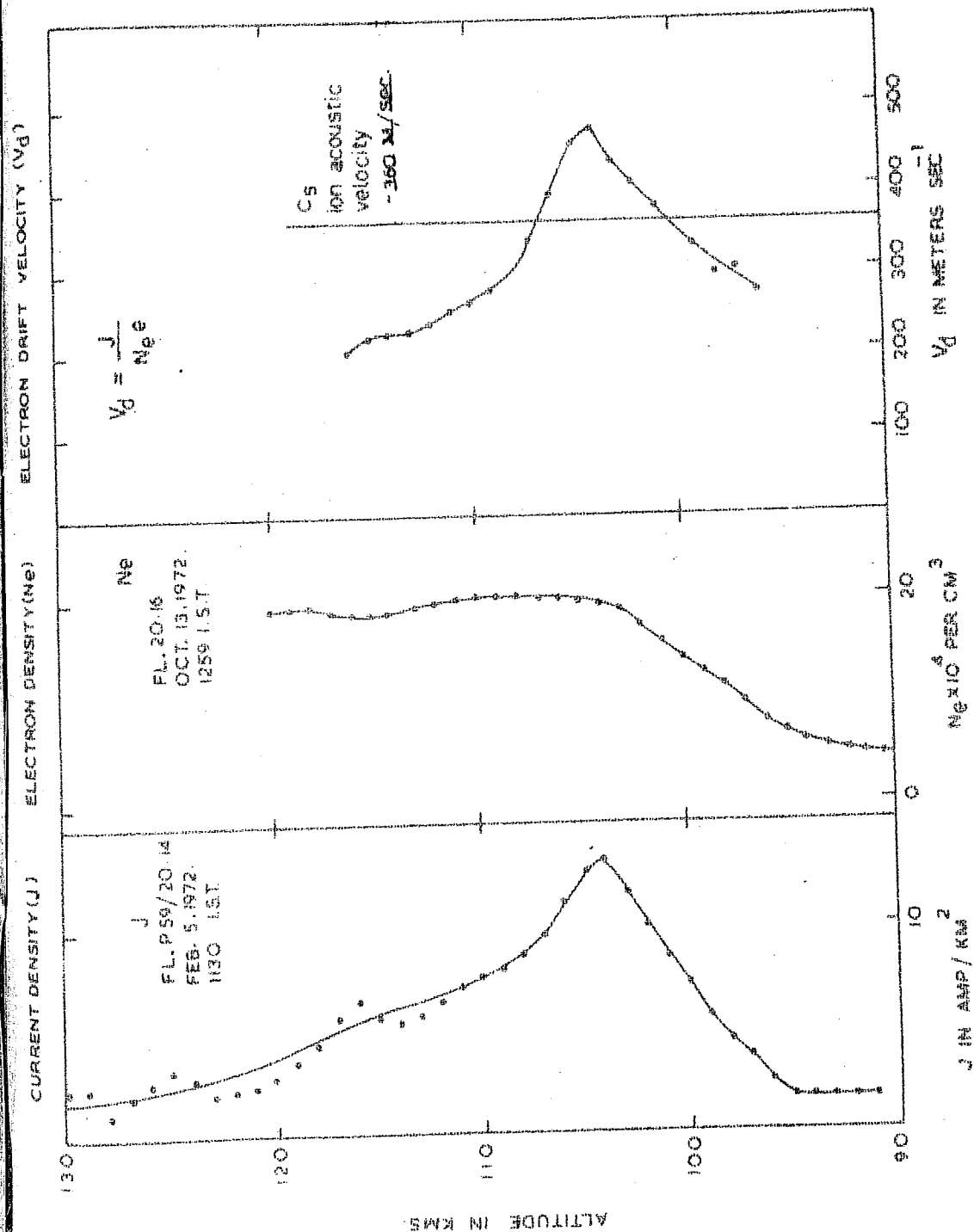


FIG. 4.9. The electron drift velocity V_d derived from the J measurements of Fl. P59/20.14 and N_e measurements of Fl. 20.16, over Thumba. V_d values exceeded the threshold Cs, between 100 and 106 km altitude. The effect of stabilisation of two-stream instability, should be noticeable in this region, on the J profile. However, no such effect is seen in the J profile.

redistribution of excess current that should have given the current layer a larger thickness is evident in the J profile.

Recently Kato (1973) has examined the problem of ionospheric irregularities. He finds that the stabilisation of two stream instability sets-in, not when electron drift velocity V_d exceeds the threshold ion-acoustic velocity C_s but when V_d exceeds 1.4 times C_s . But the results from Fl. P59/20.14 presented in Fig. 4.9 shows that V_d reached a value nearly 1.4 times C_s , still no effect attributable to stabilisation of two stream instability is seen. Hence, the mechanism suggested by Rogister and Sato does not become effective at least upto $\Delta H \leq 135$ nT and $V_d \leq 500$ m/sec. The question whether the stabilisation becomes effective beyond these values, is open for investigation. In any case, the number of quiet days with $\Delta H > 135$ nT, may not exceed 1 to 2% in an year. Hence, we can conclude that the stabilisation of two stream instability does not affect the prediction of vertical profile of current density as presented here. However determination of vertical distribution of current density on abnormally strong jet days may need in-situ measurements.

4.4 Relation between J, ΔH and $H_{induced}$:

It may be pointed out that in the exercise of deriving conclusions for the prediction of distribution of current

density in the electrojet, presented in section 4.3, the dependence was entirely on the data available from in-situ as well as ground measurements. No model was invoked. Also, while examining the causes of day-to-day variability of H amplitude, ionospheric and non-ionospheric causes were examined. The effect of currents induced in the ground by the electrojet was taken as part and parcel of ionospheric effect. In this section 4.4, we will examine how well a simple EEJ model such as the one proposed by Chapman and McNish can explain the experimental data available to us from ground magnetic stations and rocket experiments. In the process, we will re-examine the relation between the H variation observed at the ground and the electrojet strength measured by the rocket magnetometers and establish the ratio H_{nt}/H_{ext} for the Indian region around Thumba.

4.4.1 The Model:

In Chapman-McNish model, the EEJ is considered as symmetric with respect to the dip equator and having a thickness that is negligible compared to the altitude of the center of EEJ from the ground. The horizontal component of the magnetic field due to the jet of width $2W$ and current intensity i , at a distance h from the current layer is written as,

$$H = \frac{i}{W} \arctan \left(\frac{2Wh}{h^2 + x^2 - W^2} \right) \quad (1)$$

where X is the latitudinal distance of the station from the dip equator. Quantities h and i are obtained from rocket measurements and W is determined from H variation data obtained from the ground stations in the electrojet region.

4.4.2 Determination of width:

The half width W of the electrojet is defined as the distance from the dip equator where the ground ΔH becomes 0.7 of that at the dip equator. The ground ΔH values at the launch time of the rocket flight, are obtained from the ground observatory magnetograms. The base line for evaluating the ΔH is chosen as the average of the H values at 2300, 0000 and 0100 hrs IST on the previous night and the following night of the day of launch. For most of the flights, the ΔH values are available from the three regular observatories Trivandrum, Kodaikanal and Annamalainagar only. For the two flights P110/20.13 and P59/20.14 data from two more ground Rb magnetometer stations, one at Kovilpatti and another at Tiruchirapalli are also available.

The ΔH values at the time of the rocket launch are taken from the ground stations and a curve of the form $Y = A + B X^2$ is fitted to these points. Y is the ΔH value corresponding to the latitudinal distance X of the ground station. From this fitting, the value of X at which Y is 0.7

of A is obtained. This value gives the half width W of the electrojet. The square of the multiple correlation coefficient or the coefficient of determination, R^2 is evaluated for each of these curves fitted, to check whether the fitting is good or not. When R^2 is 1, the fit is good and zero indicates a misfit. In most of the cases, here, the value of R^2 was better than 0.9 and in few cases they were around 0.87. This indicated that the curves fitted are correct and that the assumption that the ground ΔH falls off with latitude in a parabolic manner in the region of interest that must be considered for determining the width of the jet is valid.

4.4.3 Ground induced image of the electrojet:

The contribution from the induced currents in the earth to the H variation at the surface level is estimated using the "image method" suggested first by McNish (1938) which has been later discussed by Chapman (1951). The image method assumes that the overhead electrojet currents produce an image current equal in intensity but flowing in the opposite direction. Figure 4.10 shows schematically the EEJ and its image underground. The direction of flow of currents and magnetic effects due to these currents are also shown. It can be seen from this diagram that the H component of the electrojet field and that of its image add at the earth's

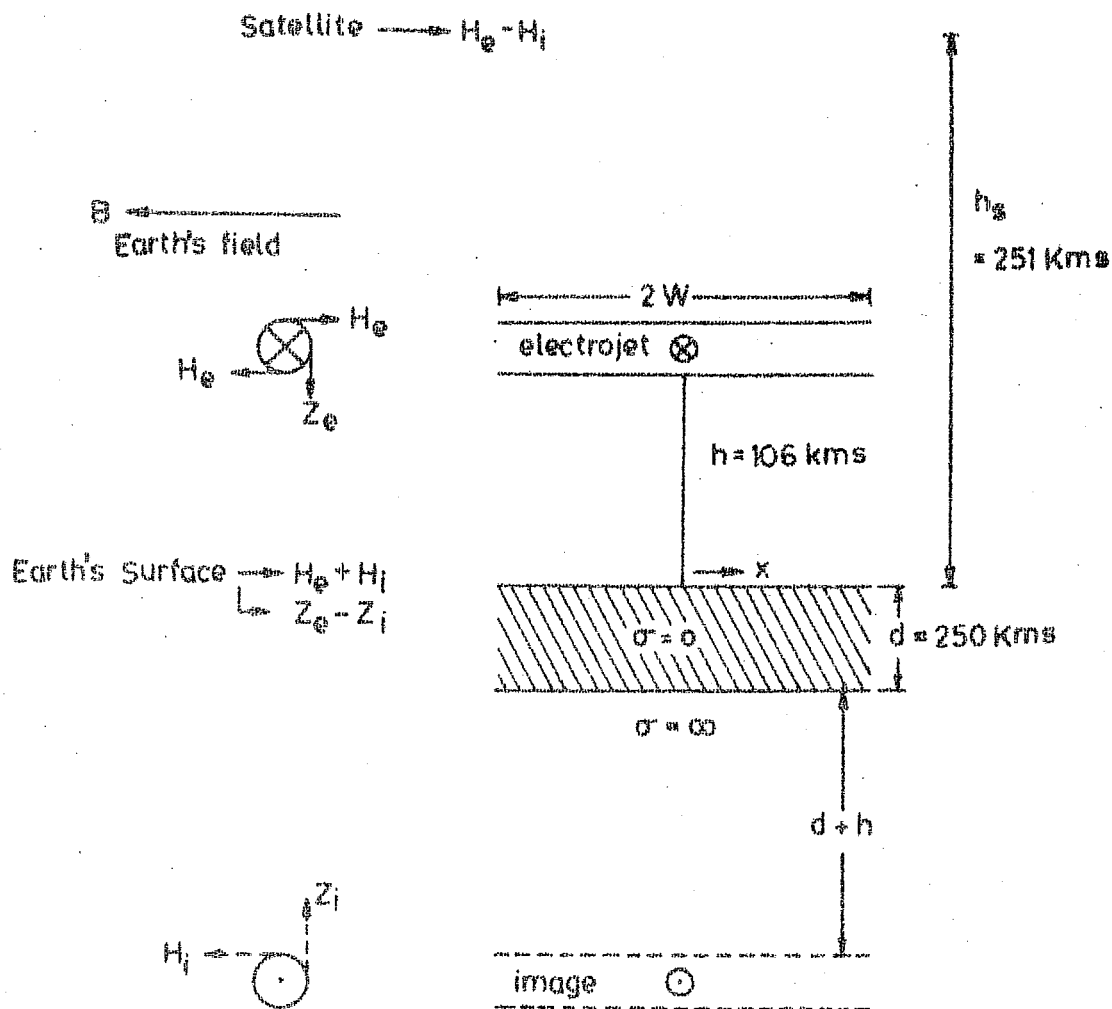


FIG. 4.10. SCHEMATICS OF THE ELECTROJET AND ITS GROUND INDUCED IMAGE. THE H COMPONENT OF THE FIELD DUE TO THE ELECTROJET AND ITS IMAGE ADD AT THE EARTH'S SURFACE AND SUBTRACT AT SATELLITE ALTITUDE.

- \otimes CURRENT FLOWS INTO THE PLANE OF THE PAPER
- \odot CURRENT FLOWS OUT OF THE PLANE OF THE PAPER

surface. The layer just below the earth's surface is a bad conductor. The conducting layer below the earth's surface is often estimated by deep earth sounding. Rokitiyanskiy (1969) has analysed the magnetic sounding data from the Indian Ocean Survey. He finds that the conducting layer is at a depth (d) of about 250 km, below the earth's surface, in the south Indian zone. Here, this value of d has been used. The image of the electrojet will be formed at a depth of (d+h) from this conducting layer or $2d+h = D$ from the surface of the earth. h is the altitude of the electrojet from the ground. Replacing $2d+h$ in the place of h in equation (1), the contribution of the image currents is calculated.

4.4.4 Evaluation of H due to the currents:

The field H due to the overhead electrojet can be written from equation (1) as,

$$H = H_{\text{ext}} = \frac{i}{W} \arctan \left(\frac{2Wh}{h^2 + X^2 - W^2} \right) \quad (2)$$

where h is the altitude of the electrojet from the ground.

The contribution due to the image currents can be written by replacing h in equation (2) by $D (=2d+h)$,

$$H = H_{\text{int}} = \frac{i}{W} \arctan \left(\frac{2WD}{D^2 + X^2 - W^2} \right) \quad (3)$$

It can be seen that the rocket magnetometer measures the total magnetic field due to the electrojet as it traverses the current layer. The difference in ΔF between 90 km (below the current layer) and 130 km (above the current layer) is the total field due to the electrojet. As, we have assumed that the electrojet is a band of uniform current, the magnetic field below the current layer is of the same magnitude but of opposite sign to that above it. Therefore, the field due to the electrojet just below the current layer is half of the total departure $(\Delta F_{90} - \Delta F_{130})$. This field is denoted as F_R .

$$F_R = \frac{\Delta F(90 \text{ km}) - \Delta F(130 \text{ km})}{2} \quad (4)$$

This F_R is nothing but H in equation (1) at $h = 0$ and $X = 0$. As the rocket is launched towards the center of the electrojet, X can be taken as zero. Putting this in equation (1)

$$\begin{aligned} F_R = H_{h=0} &= \frac{i}{W} \arctan \left(\frac{2Wh}{h^2 + X^2 - W^2} \right) \\ &= \frac{i}{W} \arctan (0) \end{aligned}$$

The function $\arctan (0)$ can take any value $n\pi$ where n is an integer and varies from 0 to ∞ . Here n can take only 1. This is because, the other values of n will introduce sharp discontinuities in the H values when evaluated with various h values. The field H will increase steadily as h decreases

and will be a maximum just below the current layer where h equals zero.

$$F_R = \frac{i}{W} \pi \quad \text{or} \quad \frac{i}{W} = \frac{F_R}{\pi} \quad (5)$$

substituting this value of $\frac{i}{W}$ in equation (2) and (3)

$$H_{\text{ext}} = \frac{F_R}{\pi} \arctan \left(\frac{2Wh}{h^2 + X^2 - W^2} \right) \quad (2')$$

$$H_{\text{int}} = \frac{F_R}{\pi} \arctan \left(\frac{2WD}{D^2 + X^2 - W^2} \right) \quad (3')$$

In equations 2' and 3', F_R and h are obtained from the rocket flights, D from Rokitiyanskiy's results and W is derived from the ground data.

The H_{ext} and H_{int} values are evaluated for all the three regular observatories, Trivandrum, Kodaikanal and Annamalainagar which are situated at different X values. From H_{ext} and H_{int} values, the field produced at the ground due to the electrojet and its image ($H_{\text{ext}} + H_{\text{int}}$) is obtained and compared with the ground ΔH value. The ratio $H_{\text{int}}/H_{\text{ext}}$ for the region around Thumba is also evaluated.

4.4.5 Errors and uncertainties in the estimation of H_{int} and H_{ext} :

Uncertainties in the determination of parameters h , F_R , W and d will introduce errors in the final H_{ext} and H_{int}

values. As pointed out in Chapter 3, the uncertainty in h is about ± 1.5 km. The experimental accuracy of determining F_R is about ± 2 nT. These uncertainties introduce no significant errors in the estimation of H_{int} and H_{ext} . The value of d is taken as 250 km on the basis of experimental result obtained after an extensive survey of the Indian Ocean region by Rokitiyanskiy as stated earlier. Also, there is evidence from POGO satellite survey, the results of which have been discussed by Cain and Sweeney (1973), that the depth of conducting layer cannot be less than 250 km in the Indian region. Their results (Fig. 16 of their paper) show significantly low ground conductivity for the region between 50° and 100° longitude. Based on the POGO results, Cain and Sweeney suggest a depth for the image plane for this region, that is about one third more than the value for Huancayo and South American region. This means that d is about 270 to 300 km for the Indian and Southeast Indian Ocean region, which agrees with the value of d assumed by us.

The major error that enters the calculations of H_{int} and H_{ext} , could be from the uncertainties in the determination of W , the width of the jet. Lack of closely spaced stations between 1° and 5° dip latitude where the magnetic effect of the jet falls off rapidly, and also the absence of stations to the south of the dip equator in the Indian region, contribute

to the uncertainty in the correct determination of W . However, the error due to an uncertainty in the evaluation of W can be estimated. If the jet has a half width of 300 km and if the uncertainty in determining this width is as large as ± 50 km, the error in determining $(H_{\text{ext}} + H_{\text{int}})$ value is only $\pm 5\text{nT}$.

In table 4.3, the results of measurements from nine magnetometer experiments conducted over the period between 1966 and 1973 and the estimated values of $(H_{\text{int}}$ and $H_{\text{ext}})$ and the ratio $H_{\text{int}}/H_{\text{ext}}$ are shown. It can be seen, that the estimated value of $(H_{\text{int}} + H_{\text{ext}})$ using the simple Chapman-McNish model agrees fairly well, within ± 5 nT, with the ΔH observed at the ground. It can also be seen that the ratio $H_{\text{int}}/H_{\text{ext}}$ is about 0.4 for the Indian region.

4.5 Conclusions:

4.5.1 The study of diurnal variation of electrojet parameters using rocket-borne magnetometers shows that,

- 1) The strength of the electrojet varies in accordance with the ground magnetic field variation during the course of a day.
- 2) Other parameters of the electrojet such as the thickness of the current layer, altitude of J_{max} , and the distribution of current density in the

Fl. No.	Fr nT	W km	H _{ext} nT	H _{int} nT	$\frac{H_{\text{ext}}}{H_{\text{ext}}}$	H _{ext} + H _{int} nT	ΔH_G nT	Observatory
20.06	105	307	81.6	32.9	0.38	114	110	TVM
			74.6	29.0	0.38	103.6	100	KOD
			60.5	27.0	0.45	87.4	82	ANN
20.07	51	275	39.0	13.9	0.35	53	58	TVM
			36.0	13.2	0.37	49	50	KOD
			26.1	12.3	0.47	38.4	41	ANN
20.09	105	440	89.4	42.4	0.47	132	127	TVM
			87.6	41.2	0.47	129	113	KOD
			83.4	39	0.47	122.4	109	ANN
20.11	110	300	86.2	32.2	0.37	118.4	120	TVM
			80.4	30.9	0.38	111.2	112	KOD
			63.8	28.7	0.45	92.4	87	ANN
20.12	72.5	317	57.3	22.1	0.39	79.8	80	TVM
			54.3	21.4	0.39	75.7	67	KOD
			45.0	20.0	0.44	65.0	58	ANN
20.13	67.5	300	50.9	19	0.37	70	75	TVM
P110			47.5	18.2	0.38	65.7	68	KOD
			37.7	17.0	0.45	54.0	52	ANN

contd... b...

...b...

20.14	115	341	92.6	37.4	0.4	131	135	TVM
P59			88.7	36.1	0.41	124.9	128	KOD
			77.1	33.8	0.44	110.9	110	ANN
20.16	75	265	56.8	19.6	0.35	76.5	85	TVM
			51.3	18.8	0.37	70.1	76	KOD
			36.0	17.5	0.45	53.4	52	ANN
20.17	71.5	297	55.9	20.7	0.37	76.6	88.5	TVM
			52.0	20.	0.38	72.0	76.0	KOD
			41.0	18.5	0.45	59.5	61.0	ANN

TABLE 4.3. The values of Hint and Hext computed using the data from rocket-borne magnetometer experiments and the data from ground magnetic stations. These computations are done using the Chapman-McNish model, as discussed in section 4.4.

Jet (or in other words the vertical profile of current density) do not change significantly from noon to afternoon hours during the course of a quiet day.

- 3) No significant current flows during the night on magnetically quiet days.
- 4) Experimentally measured current density peaks at a distinctly higher altitude compared to the altitude of \bar{U}_3 , calculated by using model values of ionospheric parameters (taken from CIRA 1965 model).

4.5.2 The study of day-to-day variability of electrojet parameters has shown that,

- 5) Large day-to-day changes in the amplitude of H variation observed on quiet days are due to changes in the strength of the electrojet itself. Changes in other electrojet parameters do not contribute significantly to the day-to-day variability of H amplitude.
- 6) Changes in the velocity of winds that control the electric fields in the region of the electrojet are the main source of day-to-day variability of the strength of the electrojet and consequently the variability in H variation amplitude.
- 7) Magnetospheric contribution to the day-to-day variability of the strength of the EEJ is negligible.

- 8) Given the magnetogram from a station under the electrojet, it is possible within certain limits to predict the vertical distribution of current density in the jet at any time of a magnetically quiet day.
- 9) Neither the reduction of peak current density nor the redistribution of current density in the jet, supposed to become effective on high jet days due to the stabilisation of two stream instability in the EEJ region is evident in the current density profiles obtained from in-situ measurements. The results show that the mechanism of stabilisation of two stream instability suggested by Rogister and Sato, to explain the back scatter radar echoes from type I irregularities on high jet days, does not become operative at least upto jet strengths equivalent to $\Delta H \leq 135$ nT.
- 10) A simple uniform current band EEJ model, that takes into account the earth induced currents can explain the ground magnetic variation in terms of rocket measured electrojet strength. The magnetic field values calculated from the EEJ model agrees with the observed field at the ground within ± 5 nT.
- 11) The depth of the conducting layer cannot be less than 250 km for the Indian Zone around Thumba. Based on this value of d , the ratio H_{int}/H_{ext} for the Indian Zone is 0.4.

5.1 Introduction:

The results of a study of the quiet day electrojet by in-situ measurements of magnetic field were presented in the previous chapter. In this chapter, the results from a unique rocket magnetometer flight conducted for the study of the equatorial electrojet during the main phase of a magnetic storm will be discussed.

It is now well known that just as the amplitude of the regular quiet time diurnal variation of geomagnetic field shows an enhancement in the equatorial region, some of the short duration disturbances also show such enhancements in this region. Ferraro and Unthank (1951), Sugiura (1953), Yamura (1954) and many others have studied the enhancement of storm time disturbance effects near the dip equator. Sugiura (1953) pointed out that the storm sudden commencements (SSC) during day time show considerable enhancements in the equatorial region. Enhancements of the amplitude of initial phase were observed by Vestine (1953) and Forbush and Vestine (1955), and the enhancement of negative SSCs was reported by Matsushita (1960). Vestine (1953) who studied the field

depression during the main phase of several storms found no enhancement in the main phase depression in the equatorial region. Obayashi (1969) has summarised the effects of extra-terrestrial origin observed in the electrojet region. He has discussed the origin of the DP2 associated fluctuations, occasionally seen in the electrojet region, during certain disturbed periods. The various storm time effects in the electrojet region have been reviewed by Bhargava (1969).

Kane (1973) has evaluated the DS component during the magnetic storm and has observed that the equatorial electrojet during the noon hours usually weakens during the main phase of a magnetic storm and sometimes during the recovery phase also. Some of the important features of disturbed day geomagnetic variations have been summarised and presented in a recent review by Kane (1976).

Taking the observed day time enhancement of disturbance variations in the equatorial region as mainly of ionospheric origin, mechanisms have been suggested by Akasofu and Chapman (1964), Closs (1967) and others to explain the augmentation of SSC and initial phase effects in the equatorial region.

The only in-situ measurement carried out so far for the study of mid latitude ionospheric currents during magnetic storm did not, according to Burrows (1976), show any modifi-

cation of the Sq currents during the storm. No results of in-situ investigation of equatorial electrojet during a magnetic storm have been reported so far except the one presented here. In this investigation, the effect of the storm on the equatorial electrojet has been studied using simultaneous measurements from a rocket-borne magnetometer and the data from a string of ground magnetometer stations spread in latitude across the electrojet region.

5.2 Details of the Experiment:

A Petrel rocket carrying a dual cell Rb. vapour magnetometer (FL. P60/20.15) was launched from Thumba, on February 13, 1972 at 1825 hrs. IST. The magnetometer sensor was mounted at an angle of 45° to the rocket spin axis. The rocket was launched at an azimuth of 266° and an elevation of 86° . As discussed in chapter 2, section 2.1.2, with this mounting and launch coordinates, the magnetometer will give good signal except during two narrow dead zones in a spin cycle. The rocket reached an apogee of about 143 km. The trajectory information was obtained using the radar skin-track data, the azimuth and elevation values from the ground tone-range system and the on-board magnetometer data.

Data from the rocket-borne magnetometer was obtained throughout the upward leg of the flight. Soon after the apogee, the data was lost due to telemetry failure. Signal appeared again just before the vehicle reentry and good data was obtained thereafter. The fore-body release mechanism used for separating the experimental payload from the second stage of the rocket did not function, which resulted in a modulation of the measured field by about ± 10 nT.

5.3 Ground Data:

The launch day, February 13, 1972 was characterised by a mild magnetic storm. The H variations recorded at Trivandrum, Kovilpatti, Kodaikanal, Tiruchirappalli and Annamalainagar stations which are under the equatorial electrojet, the records from Hyderabad and Alibag observatories which are away from the electrojet and the magnetic H variation at Sabhawala, an observatory near the Sq focus, on February 13, 1972 were examined to determine the effect of storm on the diurnal variation. Figure 5.1 shows the H variations observed at these stations on the day of launch. It is seen that the magnetic field variation was undisturbed as on quiet day until about 1600 hrs. IST. The field started decreasing rapidly after 1600 hrs and reached a minimum around 1830 hrs IST. Thereafter the field started recovering.

Ap = 22

FEBRUARY 13, 1972
FL P60/20.15, 1825 HRS IST

40 nT

DIP LAT

SABHAWALA (25)
ALIBAG (12.5)
HYDERABAD (10.1)
ANNAMALAI NAGAR (2.75)
TIRUCHIRA PALLI (2.4)
KODAIKANAL (1.5)
KOVILPATTI (0.17)
TRIVANDRUM (-0.5)

T₀
P60/20.15

20

HOURS IN IST

05

10

15

20

FIG. 5.1. The H variations recorded at the ground magnetic observatories and temporary magnetic stations, Kovilpatti and Tiruchirappalli, on Feb. 13, 1972. The launch time of the flight P60/20.15 is shown in the figure. The depression in H at the time of launch is due to the main phase of a weak magnetic storm. Hourly values of H have been used in preparing these plots.

The rapid decrease in the H field after 1600 hours IST was due to the main phase of a magnetic storm. The day was characterised with an Ap index of 22.

5.4 Discussion:

It is seen from the magnetograms of Figure 5.1 that the H variation level of the previous midnight was quiet, at all the stations. The depression from the previous midnight level in the H component at the launch time of the rocket, (1825 hrs IST) at different stations considered, is shown in table 5.1 . Careful examination of the data of Figure 5.1 and table 5.1 show that the depression is not the same at all the stations.

Station	Depression at 1830 hrs on February 13, 1972, in nT.
Trivandrum	29
Kovilpatti	30
Kodaikanal	30
Tiruchirapalli	32
Annamalainagar	14*
Hyderabad	39
Alibag	40
Sabhawala	55

Trivandrum	29
Kovilpatti	30
Kodaikanal	30
Tiruchirapalli	32
Annamalainagar	14*
Hyderabad	39
Alibag	40
Sabhawala	55

*The instrument did not function between 0900 to 1100 hrs IST and the ΔH at 1200 hrs IST is greater than that at Trivandrum which indicates that the magnetogram is in error).

TABLE 5.1 The depression in the horizontal component of the earth's field, below the previous midnight level at 1830 hrs IST on Feb. 13, 1972, recorded at the various ground stations

The rapid decrease in the H field after 1600 hours IST was due to the main phase of a magnetic storm. The day was characterised with an Ap index of 22.

5.4 Discussion:

It is seen from the magnetograms of Figure 5.1 that the H variation level of the previous midnight was quiet, at all the stations. The depression from the previous midnight level in the H component at the launch time of the rocket, (1825 hrs IST) at different stations considered, is shown in table 5.1 .

Careful examination of the data of Figure 5.1 and table 5.1 show that the depression is not the same at all the stations.

Station	Depression at 1830 hrs on February 13, 1972, in nT.
Trivandrum	29
Kovilpatti	30
Kodaikanal	30
Tiruchirapalli	32
Annamalainagar	14*
Hyderabad	39
Alibag	40
Sabhawala	55

*The instrument did not function between 0900 to 1100 hrs IST and the ΔH at 1200 hrs IST is greater than that at Trivandrum which indicates that the magnetogram is in error).

TABLE 5.1 The depression in the horizontal component of the earth's field, below the previous midnight level at 1830 hrs IST on Feb. 13, 1972, recorded at the various ground stations

The depression is minimum at Trivandrum and increases systematically with latitude. We will first examine, how this can happen.

As the depression in the magnetic field due to the main phase of the magnetic storm is caused by the magnetospheric ring currents, the depression can be expected to be the same at low latitude stations like Trivandrum and Alibag. The magnetic storm effect has a symmetric component D_{st} and an asymmetric component DS . The values of equatorial D_{st} are evaluated periodically and published by Sugiura and Poros (1971). The D_{st} is latitude dependant, and changes as $D_{st} \cos \theta$ where θ is the geomagnetic latitude of the station. $D_{st} \cos \theta$ is not very much different for the stations Trivandrum and Alibag, hence latitudinal dependence of D_{st} cannot explain the observed difference in depression at these two stations. DS effect is longitude dependant and is not evaluated regularly. The longitude difference between Alibag and Trivandrum is negligible to have any difference in DS effect. Therefore, the observed systematic decrease in depression with latitude must be of ionospheric origin. An estimate of this effect can be made as discussed below with the available data.

One method of evaluating the strength of the electrojet is to subtract the H variation at Alibag from that of Trivandrum. By this way the common magnetospheric effects are removed and the remainder will be mostly the ionospheric effect, specially that due to the electrojet. The $H_T - H_A$ curve for February 13, 1972 is shown in Figure 5.2a. It can be seen from this that a positive departure of about 10 nT persisted at this time at the ground, due to the electrojet flowing eastwards. To find whether such a positive variation of about 10 nT is normally expected at these hours (1830 hrs) on quiet days or not, the average of the H variation on five international quiet days for the months of January, February and March 1972 at Trivandrum was examined. This average variation is shown in Figure 5.2b. It can be seen here also, that on the average, a positive excursion of about 12 nT at 1830 hours is expected on quiet days in this season, indicating that the depression being less at Trivandrum at 1830 hrs on February 13, 1972 as compared to other stations is due to a positive contribution from the ionospheric currents. This means that the storm depression is counteracted by the normally present electrojet effect and what is actually observed at the ground is the resultant of storm depression and the positive effect of the electrojet. While the storm effect does not change appreciably with latitude, the electrojet effect falls off

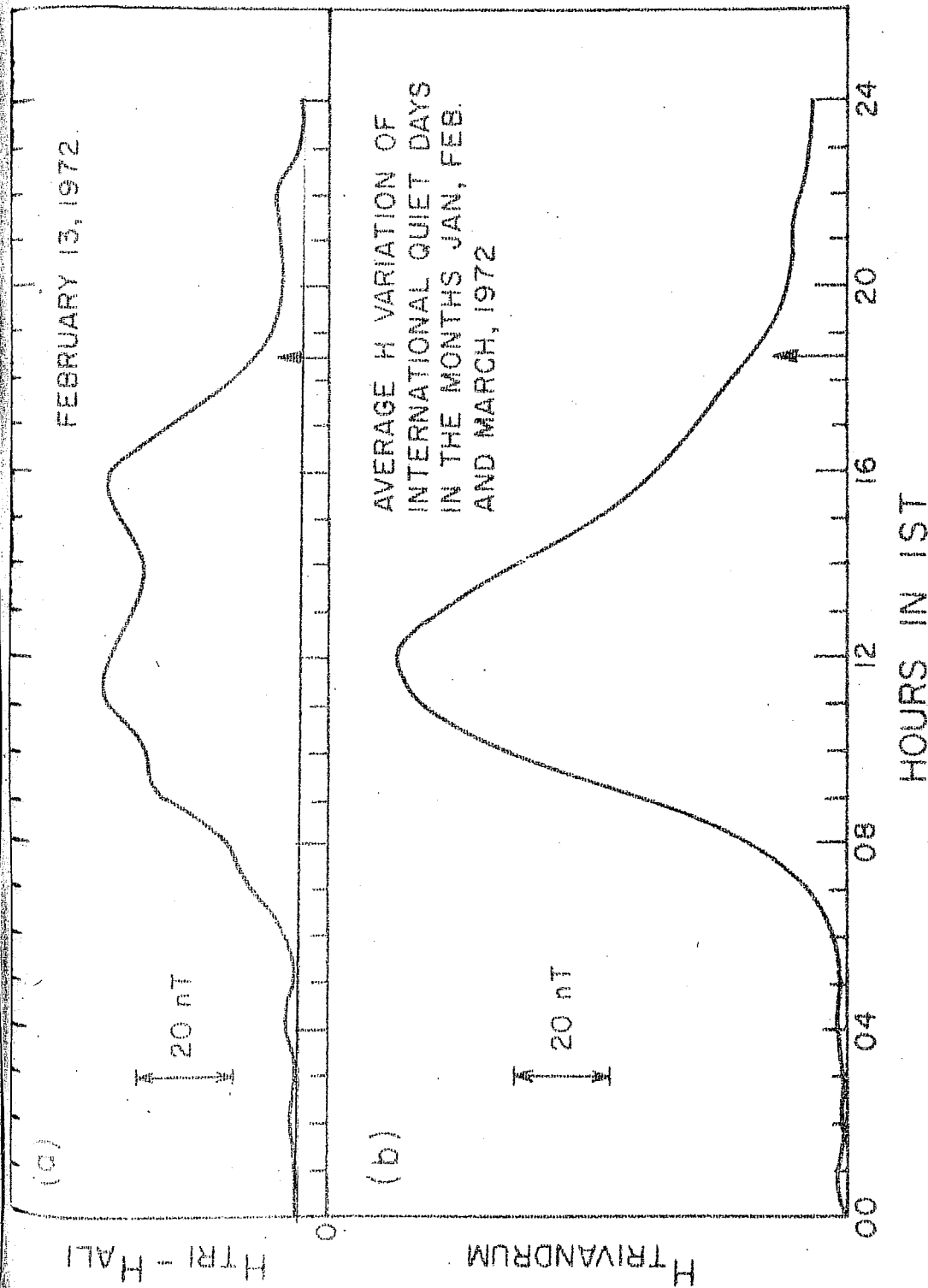


FIG. 5.2. a) The electrojet strength on Feb. 13, 1972, as obtained from subtracting the H variation at Alibag (H_{ALI}), a non-electrojet station from that at Trivandrum (H_{TRI}) an electrojet station. A positive ΔH of about 10 nT from the midnight levels is seen at the launch time of Fl. P60/20.15

b) The average of the H variations at Trivandrum on international quiet days in the months of Jan., Feb. and March 1972. A positive ΔH of about 12 nT from the mean night level is seen here also at the launch time of Fl. P60/20.15.

rapidly with latitude. This explains why the depression is minimum where the jet effect is maximum.

The evidence to show that both the storm effect and the jet effect were simultaneously present at the equatorial stations during the storm main phase comes from the rocket measurements of Flight P60/20.15. The result from this flight is shown in Figure 5.3, where the difference field ΔF is plotted against the altitude. It can be clearly seen from this figure that there is no indication of reversed currents at the time of this flight that can account for the field depression observed at Trivandrum and other low latitude stations. Further, there is an indication that the current flow, whatever its intensity be, was normal as on a normal quiet day. It can be seen from Figure 5.3 that the ΔF levels below 90 km and above 130 km are distinctly different and the first level is higher than the second, during both ascent and descent. Intensity of the current cannot be estimated correctly due to large modulation on the ΔF profile, but it can be said that the electrojet effect cannot be more than 20 nT, which is the peak to peak amplitude of the modulation. This is the electrojet effect that is expected corresponding to the ground variation of 10 nT observed at the time of the flight as discussed earlier, (Figure 5.2). Thus, the study of the data from the ground

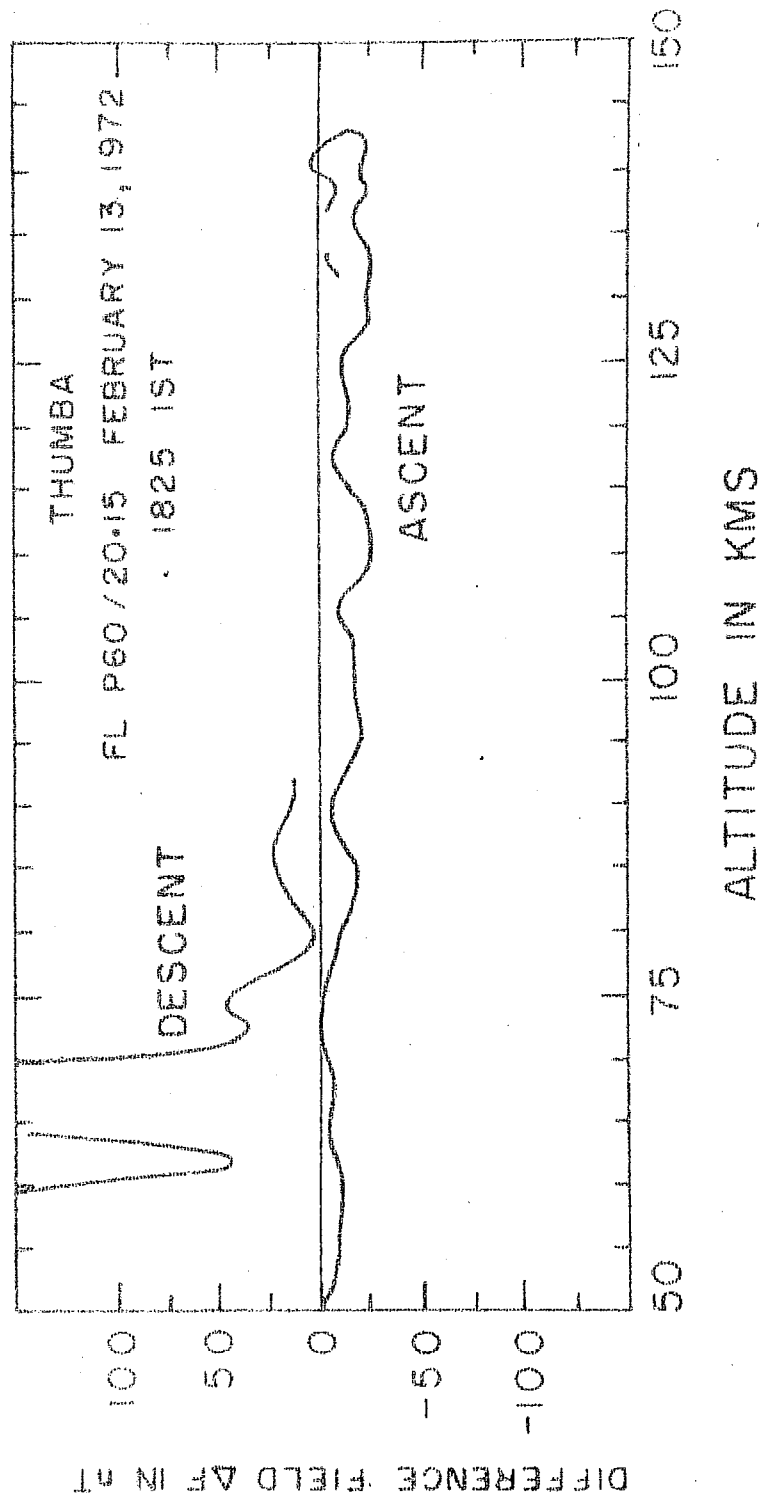


FIG. 5.3. The difference field $\Delta F = (F - F_T)$ plotted as a function of altitude. F is the rocket measured field from FL P60/20.15 and F_T is the theoretically computed field for this flight epoch.

stations and the data from in-situ measurements show that the main phase of the storm did not affect the electrojet.

5.5 Conclusions:

1. The rocket magnetometer launched during the main phase of a storm did not detect any reversed currents that could produce or could have enhanced the depression observed on the ground. This indicates that the observed depression is of magnetospheric origin.
2. There is an indication in the flight results of an east-ward electrojet at the time of the flight, whose magnetic effect is of the order of 10 nT. From an analysis of the ground station data, such an electrojet effect is expected on quiet days in this season. The magnitude of this current is sufficient to account for the systematic decrease in the depression of the magnetic field observed as the center of the electrojet is approached.

6.1 Introduction:

The electron temperature distribution, under equilibrium conditions, is determined by balancing the rate of heat input to the ambient electron gas and the rate of energy loss by various loss processes. Solar radiation is the dominant heat source for the atmosphere.

The process of heating by the solar radiation is as follows. When the solar radiation causes an ionization reaction, the photoelectron produced generally has kinetic energy much greater than the energy of the ambient particles. These photoelectrons lose energy by collisions with the neutral atmosphere, mostly by excitation process, or in coulomb collisions with the ambient electrons. The former process is important at lower altitudes, but becomes ineffective once the photoelectron energy drops below 1.5 eV. The remainder of the energy then goes to the electron gas. The electron-electron collision rate is sufficiently great relative to the others that the energy gained is randomised, resulting in a Maxwellian energy distribution, characterised

by the temperature T_e . The loss due to elastic collisions with the positive ions become the dominant loss mechanism above 300 km. The ions and neutrals, except in the upper F-region, attain equilibrium amongst themselves and are considered to have a common temperature T_g .

Based on these considerations, theoretical electron temperature profiles have been derived by Hanson and Johnson (1961) and Hanson (1962). The work of these authors have been extended by Dalgarno et. al., (1963), Willmore (1964), Geisler and Bowhill (1965), Banks (1966) and Walker (1968) amongst others. Basic results of these theoretical calculations are:

- a) The electron temperature increases with the altitude throughout the ionosphere. There is a thermal disequilibrium above 120 km, where the electron temperature T_e is greater than the neutral gas temperature T_g . Below this altitude $T_e \approx T_g$.
- b) The energy that maintains T_e above T_g comes from the solar radiation. The energy absorption from the solar radiation is maximum around 160 km. Due to this $(T_e - T_g)$ increases upto this altitude, and above this altitude, $(T_e - T_g)$ still continues to increase for a few kilometers due to increasing

heating efficiency of the photoelectrons at these altitudes. Above this, the difference ($T_e - T_g$) is expected to fall.

c) In the upper F-region, the ion temperature T_i always lies between T_e and T_g , because ions gain energy by elastic collisions with the electrons and lose it by collisions with neutrals. Below 250 km, where the neutral density is much greater than the electron density, $T_i = T_g$ and at greater heights where the neutral density falls faster than the electron density, T_i is greater than T_g .

d) Below 120 km, the collisional cooling is so large in comparison with the solar EUV input, that $T_e = T_g = T_i$. Walker (1968) has suggested that electrons in this region, may be in thermal equilibrium with the vibrational levels of N_2 .

Though the temperature distribution is often derived by assuming the solar EUV radiation as the only source, Harris and Priester (1962) pointed out that, unless the heating efficiency of EUV absorption is unusually high, the magnitude of EUV heating is not sufficient to maintain a normal thermosphere. Roble and Dickinson (1973) showed that, on the basis of the observed temperature gradients at the lower thermosphere boundary, approximately two or three

times the computed EUV heat input is needed to maintain the mean thermosphere. To account for the additional energy source needed to explain this, several mechanisms have been suggested as sources of heat energy for the atmosphere. Some of these mechanisms are chemical reactions, absorption of energy from charged particles, hydromagnetic waves, joule heating by the electric currents and atmospheric gravity waves.

The joule heating by electric currents was recognised as an important heat source in the disturbed thermosphere by Cole (1962). Kato (1963) suggested that the joule heating due to the strong currents in the equatorial electrojet will increase the electron temperature over the neutrals in the Equatorial E-region. Recently, Ching and Chiu (1973) have considered the joule heating as an important contributory heat source in the maintenance of the mean thermosphere itself rather than treating it in a restricted sense as a transient heat source of the disturbed thermosphere or just as a local heat source such as the electrojet. This trend indicates that the joule heating due to electric currents in the upper atmosphere has gained recognition as a potential heat source for the maintenance of the normal thermosphere.

Here, the effect of joule heating in increasing the electron temperature over the neutrals in the equatorial E-region is studied by rocket-borne measurements of the electric currents and the electron temperature simultaneously. This is the first study in which an attempt has been made to understand the joule heating effect, by in-situ measurements. The results of this study has been discussed in detail by Sampath et. al., (1974). Here a brief summary is presented, without leaving the essence of this study, while the details are found in the attached reprint of the above said paper.

6.2 Flight details and flight data:

A Nike-Apache rocket (FL.20.11) carrying a proton precession magnetometer and an electron temperature probe was launched on April 25, 1971, at 1130 hrs. IST, from Thumba. The day was magnetically quiet. The ground ΔH was about 120 nT at the time of flight indicating a strong electrojet. The rocket reached an apogee of about 160 km. The electron temperature probe used is the same one as described by Hirao and Oyama (1970).

Good data was recovered from, both the magnetometer and the electron temperature probe. The electron temperatures T_e measured during this flight are shown together

with the neutral gas temperatures T_g taken from the CIRA 1965 model, in Figure 6.1a. The current density derived from the magnetometer data is shown in Figure 6.1b.

6.3 Discussion of the flight results:

From Figure 6.1a, it can be seen that the measured electron temperatures increase throughout in the E-region and were considerably higher than the model neutral temperatures T_g . To study whether the joule heating effect is present or not, the excess of T_e over T_g , obtained from Figure 6.1a, is shown in Figure 6.1b, together with the electrojet current density J . The $T_e - T_g$ profile shows a broad maximum around 106 km, corresponding to the electrojet layer. This qualitatively indicates that joule heating increases the electron temperature over that of the neutrals in the E-region around 106 km. To get a quantitative estimate of the joule heating, the energy delivered by the electrojet or the heating rate Q_H of the electrojet is estimated from the measured electrojet strength. This is compared with the energy needed to maintain the observed temperature difference or the cooling rate Q_T . The heating rate is obtained using the relation $Q_H = J^2 / \sigma_3$ where σ_3 is the cooling conductivity. In calculating the cooling rate, the only loss process considered is the loss due to collisions. Other loss processes such as conduction

THUMBA

FL.20.11 APRIL 25, 1971 1130 HRS IST

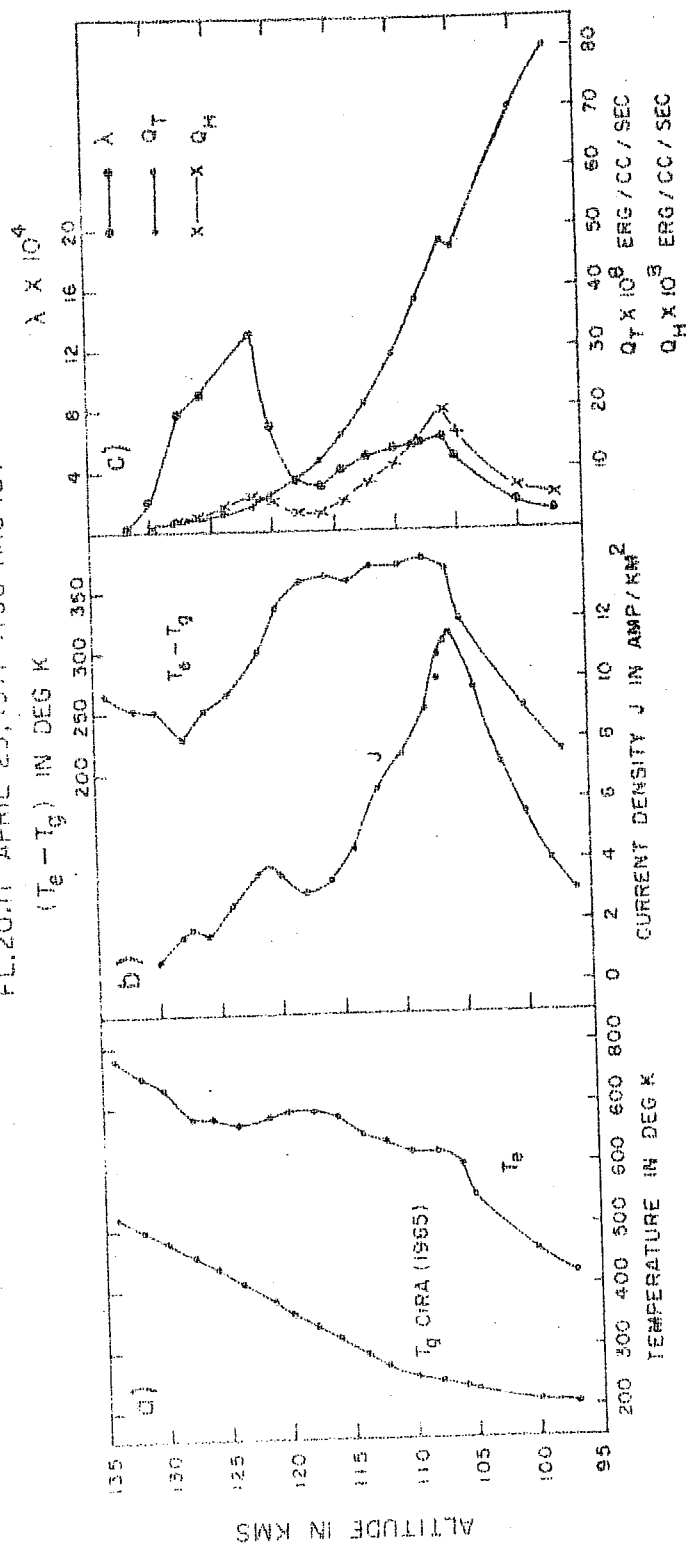


FIG. 6.1. STUDY OF JOULE HEATING EFFECT USING ELECTROJET CURRENT DENSITY AND ELECTRON TEMPERATURE MEASURED SIMULTANEOUSLY

FIG. 6.1. For figure caption, please see overleaf.

FIGURE CAPTION

FIG. 6.1. a) Altitude profile of electron temperature T_e measured by a rocket-borne temperature probe. The rocket was launched from Thumba, near noon when the electrojet was strong. T_g is the CIRA 1965 model neutral gas temperature.

b) Figure shows the results from simultaneous measurement of electrojet current density J and electron temperature. J profile shows the vertical distribution of current density in the jet and $T_e - T_g$ shows the profile of excess electron temperature over the neutral gas temperature. J shows a sharp maximum at 106 km. $T_e - T_g$ also increases in the same way as J to reach a maximum near 106 km but shows a broad maximum extending upto 120 km.

c) Q_H is the energy generated due to Joule heating by the observed electrojet current. Q_T is the theoretically calculated energy that is needed to maintain the observed temperature difference $T_e - T_g$. It can be seen that Q_H is roughly one third of Q_T near the center of the electrojet. λ is the mean fractional energy loss per collision of electron with neutrals. The values of λ around the center of the electrojet shows that collisions are inelastic in this region.

are neglected. This cooling rate Q_T is calculated according to a method followed by Dalgarno et. al., (1963). The observed temperature difference $(T_e - T_g)$ shown in Figure 6.1b is used in evaluating the cooling rate, Q_T . These two parameters Q_T and Q_H are shown as a function of altitude in Figure 6.1c. From this figure, it can be seen that the measured electrojet strength can account for only one third of the observed temperature difference, $(T_e - T_g)$.

This discrepancy could be partly due to the error in the measurement of electron temperature by the probe method. The main sources of error in the probe measurements are the contamination of the probe surface and the sheath effect. Hanson et. al., (1969) and Brace et. al., (1970) have shown that the electron temperatures measured by the probe method are always higher than the values obtained from back scatter methods. If this is true for the E-region measurements, then the observed discrepancy will be reduced.

Another contributing factor to the discrepancy could be that the model T_g values have been used here. No measurements of T_g over the equator are available at present.

The best solution to this problem, is to measure the electron temperature in the night-time at the equator,

when the electrojet current effects are negligible and compare it with the daytime measurements.

In the case of joule heating, an equilibrium will be soon established between the heating rate and the cooling rate due to collisions. Under such an equilibrium condition, the rate of energy loss per collision by an electron with the neutral, can be evaluated. This important parameter λ helps in understanding the nature of collisions between electrons and neutrals. Following Kato (1963), at equilibrium, the heating rate and the cooling rate can be equated as,

$$\frac{J^2}{63} = \frac{3}{2} k N_e \nu_{en} \lambda (T_e - T_g)$$

where k is Boltzmann's constant, N_e , the electron density and ν_{en} the electron neutral collision frequency. The collision frequency is calculated using the parameters given in CIRA 1965 model. The electron density profile is taken from a noon time flight, Prakash et. al., (1971). The λ values obtained from the above equation, are plotted as a function of altitude in Figure 6.1c.

The collision is inelastic if $\lambda > \frac{2m_e}{M}$ and elastic if $\lambda \sim \frac{2m_e}{M}$. m_e is the electronic mass and M is the mass of the neutral particle in collision. Here

$$\lambda = \frac{2m_e}{M} = \frac{2 \times 9.1 \times 10^{-28}}{5 \times 10^{-23}} = 4 \times 10^{-5}$$

From Figure 6.1c, it can be seen that the λ values are higher than 10^{-5} in the region around the main electrojet layer, indicating that the collisions are inelastic in this region.

6.4 Conclusions:

1. The measured electron temperature increases throughout the E-region and is considerably higher than the CIRA 1965 model neutral gas temperature.
2. The measured excess of electron temperature over the model neutral temperature, shows a pronounced peak corresponding to the main electrojet layer indicating the joule heating effect due to the electrojet.
3. The measured electrojet strength can account for only one third of the observed $T_e - T_g$.
4. The collisions between electrons and neutrals are inelastic in the electrojet region around 106 km.

7.1 Introduction:

Irregularities are generated in the ionosphere, due to a variety of plasma instabilities arising from different plasma conditions and the configurations of magnetic and electric fields. Some of the manifestations of these irregularities are, the equatorial sporadic E (Es-q), spread F, scintillation of radio stars and HF and VHF radio wave scattering.

A relation between the electrojet intensity and the Es-q was pointed out by Matsushita (1951). Cohen et. al., (1962) have shown that the irregularities that produce Es-q are embedded in the electrojet. Cohen and Bowles (1963) detected the presence of irregularities in the height range 95 to 110 km, using a VHF forward scatter radar. Using a VHF radar at Jicamarca, the nature and characteristics of these irregularities have been studied extensively and the results have been summarised by Cohen (1967). On the basis of the observed spectra of the echoes, Balsley (1969) classified the irregularities into type I and type II. The electron

density fluctuations associated with these irregularities have been investigated using rocket-borne Langmuir probes from Thumba and the results from these investigations have been summarised in a review by Prakash et. al., (1973).

Type I irregularities and the two-stream instability:

Farley (1963) and Buneman (1963) independently proposed that when there is a relative motion between electrons and ions in an ionised medium, the two stream instability is generated due to the streaming of electrons past the ions. For a magnetoactive, weakly ionized plasma, such as in the ionospheric E region, the two stream instability comes into play when the electron drift velocity reaches a critical velocity, the ion acoustic velocity in the medium.

The ground based radar studies have brought out the following E region irregularity characteristics; that the doppler shift due to the motion of the irregularities has a narrow spectrum; the doppler shift corresponds to a velocity close to the ion-acoustic velocity and that the doppler shift does not vary considerably with the angle of observation. These observations show that the type I irregularities are generated by the two-stream instability. Though the Farley-Buneman theory can account for some of the observed features of ionospheric irregularities and their motion, all

the features are not explained by this linear theory. Waldteufel (1965) and Kato and Hirata (1967) treated this problem using equations of fluid dynamics. It is found that their results are identical to those of Farley and Buneman. Skadron and Weinstock (1969) used a non-linear approach and discussed about the stabilisation of the instability by wave-wave coupling. However, this non-linear theory could not explain the observed velocity of type I irregularities being nearly equal to the ion-acoustic velocity irrespective of the electron drift velocity (as evaluated from the electrojet strength) being exceedingly high, even exceeding the ion-acoustic velocity in the medium. Rogister (1971) used the non-linear theory and showed that with the development of the instability, the large vertical Hall field decreases and hence, with it the drift velocity also decreases. Sato (1972) made a general approach to this problem and showed that the peak electron drift velocity will be reduced due to the stabilisation of the two stream instability. All these workers in common agree to the fact that the two stream instability or the type I irregularity is generated when the electron drift velocity reaches the threshold which is the ion-acoustic velocity.

The experimental confirmation for the existence of the threshold, for the generation of type I irregularities

was obtained from rocket experiments, conducted from Thumba. The electrojet current density, the electron density and its fluctuations were measured simultaneously on two occasions. On one occasion, the electron drift velocity, derived from the electrojet current density and the electron density, reached the threshold whereas in the second occasion the threshold was not reached. The fluctuations in the electron density corresponding to the type I irregularities were detected in the first case and were not detected in the second case. The results from these studies have been presented by Prakash et. al., (1975). The rocket measurements of electron density fluctuations show that these irregularities have vertical scale sizes of 1 to 15 meters. The fluctuations show a flat spectrum with spectral index nearly zero, and an amplitude of a few per cent (2 to 3%) of the ambient electron density.

Type II irregularities and cross field instability:

The cross field instability is generated in a weakly ionised plasma when there are crossed electric and magnetic fields in the medium and at the same time the electron density gradient is parallel to the electric field in the medium. The relevance of the cross field instability to the generation of irregularities in the ionosphere has been discussed by Maeda et. al., (1963), Whitehead (1967), Reid (1968),

Rogister and D'Angelo (1970) and Kato (1973). It is now agreed that the type II irregularities are generated due to the cross field instability in the medium.

The ground based back scatter radar studies indicate that the type II irregularities have a broad spectrum and have a variable doppler shift, the doppler shift varies as $\cos \chi$ where χ is the angle of observation.

After the initial theoretical work on the cross-field instability by workers mentioned above, Sato (1968) showed that type II echoes can be explained by non-linear cross-field instability. Analytical approaches to the non-linearity of the instability have been attempted by Sato (1971) and Rogister (1972). Sato (1973) has discussed a unified theory of type I and type II irregularities.

The rocket-borne Langmuir probes have detected the type II irregularities. Their vertical scale sizes vary from 30-300 meters, and they have varying amplitudes, from a few per cent to about 30% of the ambient electron density. During the day time, the type II irregularities of very large amplitudes, more than 20% of the ambient have been detected around 85 km altitude. In the height range of 85 to 105 km there is an upward gradient in the electron density.

During the day time, when there is an eastward electrojet, the polarisation field E_z is upwards and hence the cross field instability generated irregularities are seen in this height range of 85 to 105 km.

Electric field fluctuations associated with plasma instabilities in the magnetosphere and the auroral ionosphere, have been studied using satellite and rocket borne instruments. Mozer (1973) has summarised the results from these experiments. The study of electric field fluctuations is generally carried out by measuring the frequency dependence of power in all the three components of the electric field and the dispersion characteristics of the wave in the medium. There have been no investigations so far concerning the electric field fluctuations, (or to be more precise, the quasi static electric field fluctuations) generated by the two stream and the cross field instabilities in the equatorial electrojet. In this chapter the first results of the study of electric field fluctuations in the equatorial electrojet will be presented. The investigations were carried out at Thumba using Centaure and Petral rockets. The electric field fluctuations, the electrojet current density and the electron density were measured in near simultaneous launchings, on two occasions, the first one in October 1972 and the second in March 1973. These flights were conducted near local noon, when the electrojet strength was high.

A third experiment which had a simple Langmuir double probe detector was launched in February 1975, in the early morning hours when the electrojet was not yet developed.

The results from the first two flights give the power spectra and altitude of occurrence of the irregularities during noon time when the electrojet is strong and the morning flight of February 1975, gives the information concerning the altitude variation of the intensity of horizontal AC electric field in the E region, in different frequency bands when a weak or negligible electrojet was present.

7.2 Noon time experiments:

7.2.1 Flight details: The flight details are given in the table 7.1

Flight No.	Date	Time IST	Payload	Rocket	Apogee km.
05.17	13.10.72	1227	E-field	Centaure	120
20.16	-do-	1259	Magnetometer (J) Langmuir probe (N_e)	Nike Apache	160
05.19	03.03.73	1135	E-Field	Centaure	120
20.17	-do-	1224	Magnetometer (J) Langmuir probe (N_e)	Nike Apache	160

TABLE 7.1. Details of the rocket experiments conducted from Thumba, India, for the near simultaneous measurements of electrojet current density (J), electron density (N_e) and electric field, in October 1972 and March 1973.

The centaure rockets carried multiple probes to measure electric field components. The magnetometers used are of the proton precession type. The Centaure rockets carried a radar transponder to get complete trajectory information, while the Nike Apaches were tracked by the radar on the skin-track mode. The magnetograms of the Trivandrum observatory for the launch dates October 13, 1972 and March 3, 1973 are shown in figures 7.1 and 7.2 respectively. The launch times are indicated in the figures. The ground ΔH from the mean night level, at the time of launch of FL.20.16 was 85 nT and of 20.17 was 88 nT.

7.2.2 Flight results:

a) Magnetic field and electron density data:

The magnetometer and the electron density probe of flight 20.16 gave good data during both the ascent and the descent. The current density derived from the magnetometer and the electron density data obtained from the Langmuir probe of flight 20.16 are shown in Figure 7.3a. The current density profile shows a peak current density of 9.6 amp/km^2 , at the center of the electrojet near 105 km. The electron density shows an upward gradient in the altitude region 90 to 105 km. The eastward electrojet encountered by the magnetometer indicates an upward Hall field. Direction of

TRIVANDRUM MAGNETOGRAM

1972 OCTOBER 13^d 08^h 34^m TO 14^d 08^h 30^m IST

H BASE LINE VALUE = 39581 nT

Fl. 05.17 1227 IST

Fl. 20.16 1259 IST

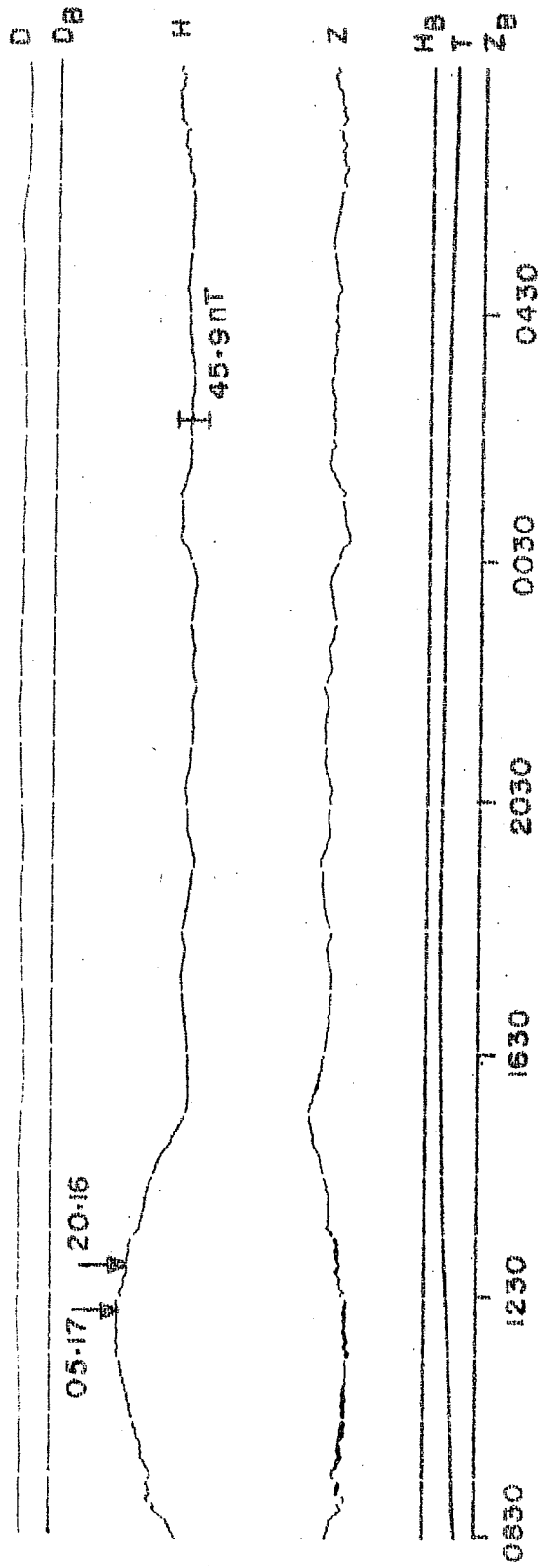


FIG. 7.1. The H, Z and D variations recorded at Trivandrum Observatory, from 0834 hrs IST on 13 October 1972 to 0830 hrs IST on 14 October 1972. The launch times of Fl. 05.17 and 20.16 are indicated in the figure.

TRIVANDRUM MAGNETOGRAM

1973 MARCH 03^d 08^h 33^m TO 04^d 08^h 30^m IST

H BASE LINE VALUE = 39562 nT

Fl. 05.19

1135 IST

Fl. 20.17

1224 IST

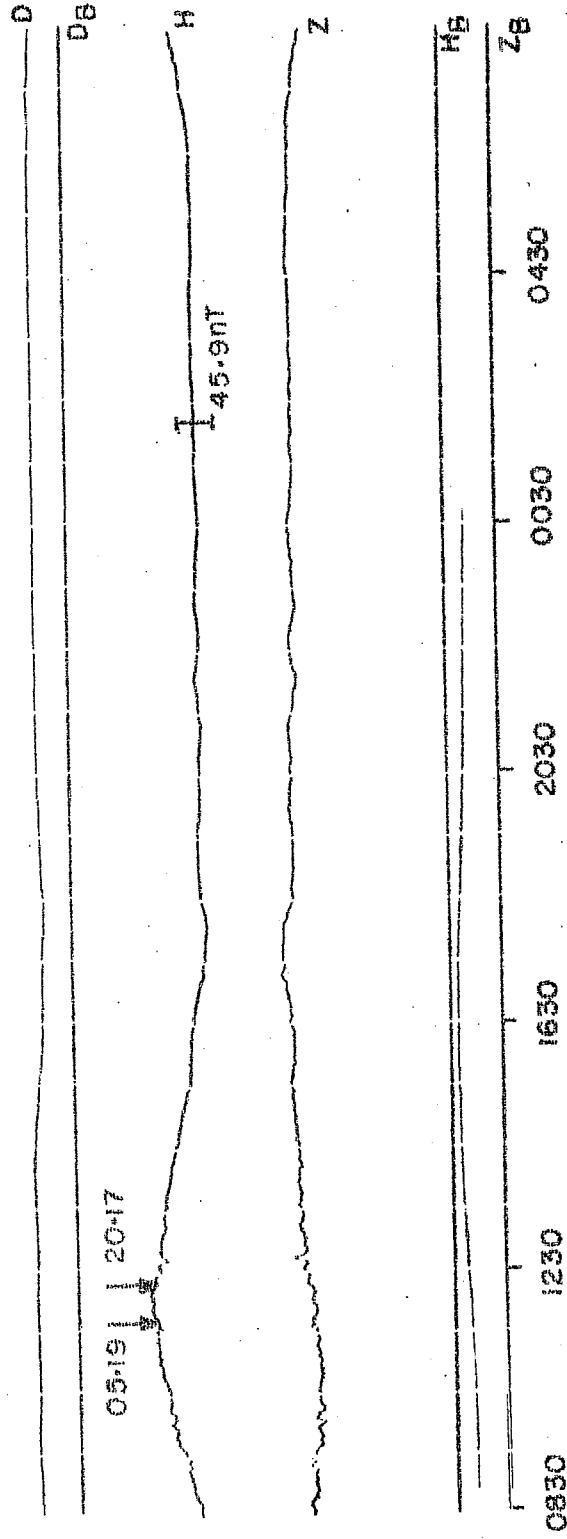


FIG. 7.2. The H, Z and D variations recorded at Trivandrum Observatory, from 0833 hrs IST on 3 March 1973 to 0830 hrs IST on 4 March 1973. The launch times of Fl. 05.19 and 20.17 are indicated in the figure.

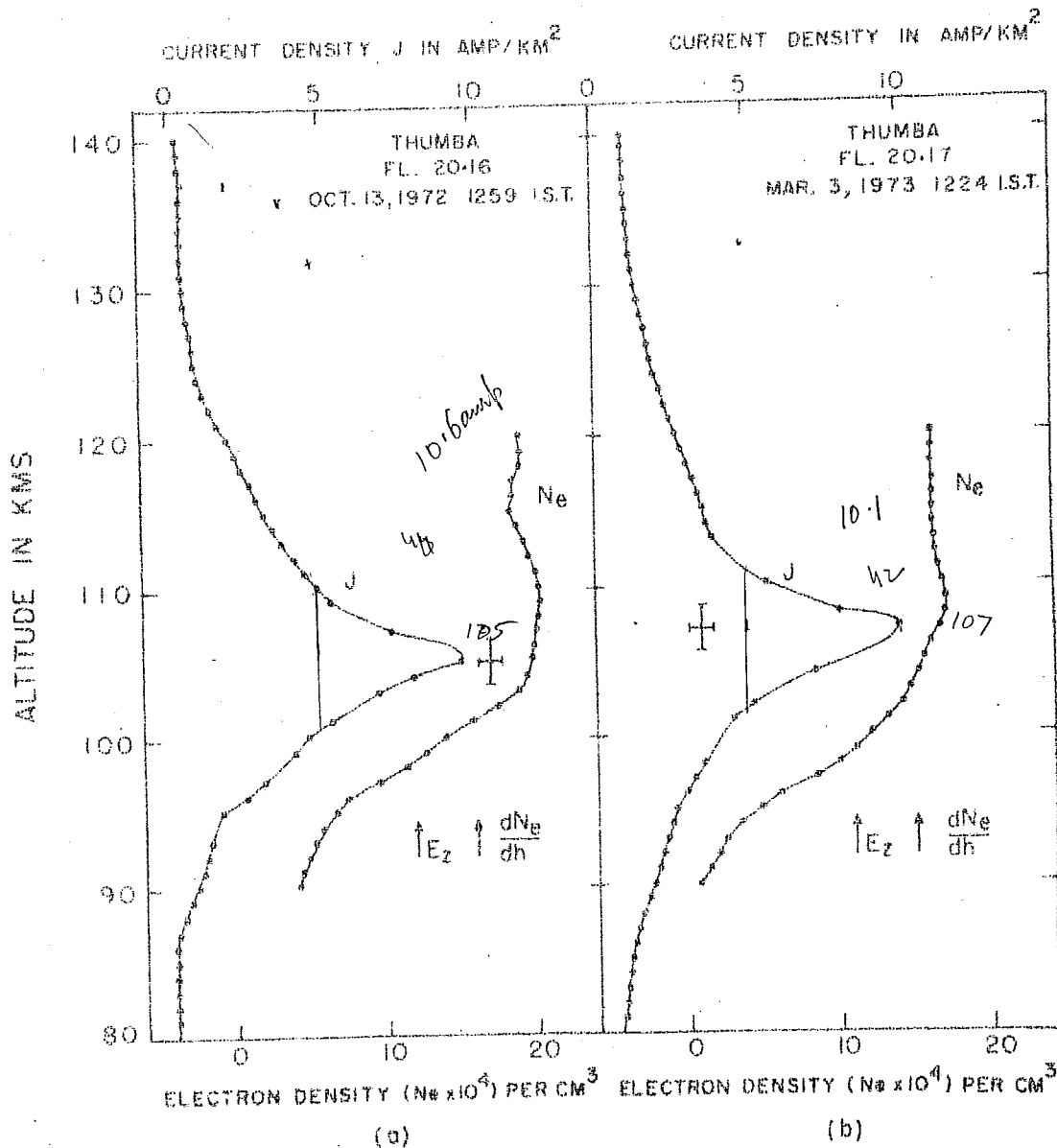
the Hall field and the electron density gradient are shown in the Figure 7.3a.

The flight 20.17 detected a similar electrojet as that encountered in the flight 20.16. The electrojet current density and the electron density profiles are shown together in Figure 7.3b. Here also, it can be seen that both the Hall field and the electron density gradient are upward in the altitude region of 90 to 105 km.

b) Electric field data:

The electric field probes on both the flights 05.17 and 05.19 gave good data from the time of deployment (about $t + 60$ seconds) till the end. The data from the flight 05.17 was a little noisy and was punctuated by a spurious noise at intervals of about 2 seconds. The noise frequency was around 300 Hz. Except for this disturbance, the data recovered in the flight was good throughout. The data from the flight 05.19 was particularly good being free from noise or interference throughout.

The frequency response of the electric field detector was kept from dc to 1 KHz so that the fluctuations in the electric field upto a frequency of about 1 KHz can be detected. This permitted the study of the power spectrum of the fluctuations upto 1 KHz. Though the payload carried multiple probes,



56

160
123.5
14858

1.15

FIG. 7.3. a) The electrojet current density J and the electron density N_e , measured during the flight 20.16. The gradient in the electron density and the Hall field point upward, between the altitudes 90 and 105 km.

b) The electrojet current density J and the electron density N_e , measured during the flight 20.17. The gradient in the electron density and the Hall field point upward between the altitudes 90 and 103 km.

the results from the horizontal electric field probes which give the fluctuations in the horizontal eastward electric field are only discussed here.

A sample telemetry chart record of the raw data of the horizontal component of the electric field obtained from the probes of flight 05.19 is shown in Figure 7.4. The data from the flight 05.19 is preferred to that of 05.17 simply because this data is clean and free from interference. In the Figure 7.4, sample data from both the ascent and the descent when the fluctuations were present are shown. The low frequency wave seen in this figure is due to the $V \times B$ induced electric field, due to the motion of the rocket with a velocity V , through the earth's magnetic field B . This $V \times B$ effect appears as a modulation with a frequency equal to the spin frequency of the rocket. When the probe system becomes parallel to the magnetic field during a spin cycle, $V \times B$ is zero and when the probe system is perpendicular to the magnetic field, $V \times B$ is maximum. The rockets are despun, before deploying the E field probes, such that the spin frequency is around 1 Hz. The higher frequency modulations seen on this low frequency wave, are due to the electric field fluctuations associated with the plasma instabilities. From Figure 7.4, it can be seen that the high frequency

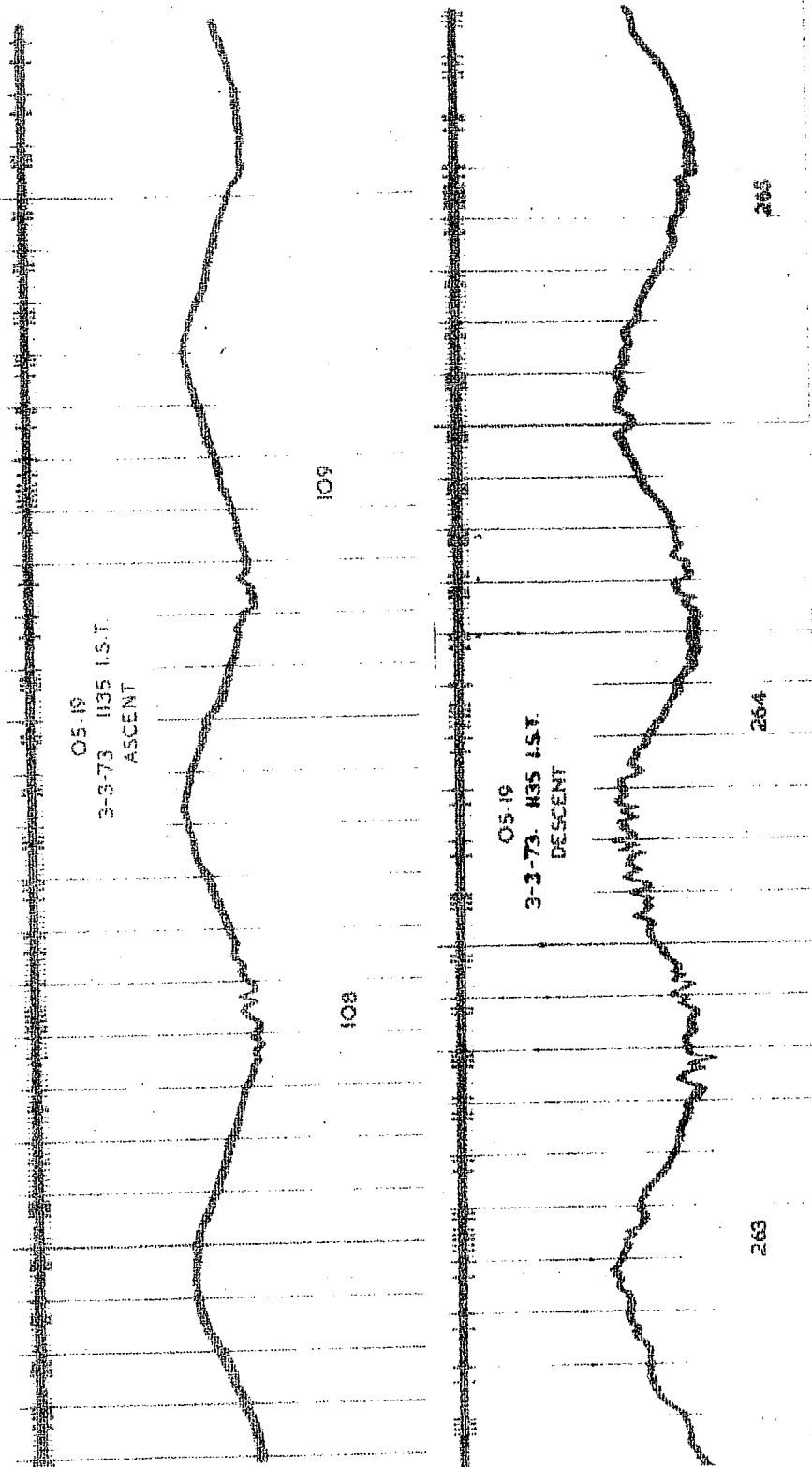


FIG. 7.4. Sample chart record of raw data, of horizontal electric field during portions of the ascent and the descent of Fl. 05.19. The low frequency wave, appearing at the spin frequency (~ 1 Hz), is due to the V X B induced electric field. The modulations seen on this low frequency wave, are due to the electric field fluctuations. Note that, these fluctuations are seen at the peaks and troughs of the low frequency wave. The numbers shown are, the time after launch, in seconds.

fluctuations are seen predominantly only at and near the peaks and troughs of the low frequency wave and not throughout. It can be noted from this figure, that the electric field fluctuations appear as modulations on the V X B induced electric field.

The raw, electric field data of the horizontal component of the electric field, is spectrum analysed on the ground using a five channel spectrum analyser, which has been discussed in chapter 2. The spectrum analyser outputs together with the raw data are recorded on a paper chart using a galvanometric recorder which has got a frequency response upto a few KHz. The five channels of the spectrum analyser are: Ch. 1 - 700 ± 350 Hz, Ch.2 - 240 ± 120 Hz, Ch.3 - 80 ± 40 Hz, Ch.4 - 26 ± 13 Hz and Ch. 5 - 9 ± 4 Hz. All the five channels are made, using constant Q and uniform gain band pass filters, so that the observed amplitudes of fluctuations in the different frequency bands are directly comparable. The raw data from the flights 05.17 and 05.19 and the channel outputs from the spectrum analyser are shown in Figures 7.5 to 7.8. Only the portions in the ascent and the descent where fluctuations were detected are shown in these figures.

The data from the ascent of the flight 05.17 between the flight times 88 seconds to 115 seconds is shown in

Figure 7.5. The raw data channel, the one shown below the Ch.5 output, shows the modulations starting at 93 seconds and continues till the end of the record upto 115 seconds. Channel 5 which is the lowest frequency channel, 4 Hz to 13 Hz, shows large amplitude fluctuations from 93 to 101 seconds and thereafter patches of fluctuations are seen at regular intervals. Channel 4, 26 ± 13 Hz, shows the presence of the fluctuations in the same time interval, much more clearly. Channel 3, 80 ± 40 Hz, indicates the presence of these fluctuations, but of lesser amplitude than channel 4. Channels 1, 700 ± 350 Hz, and 2, 240 ± 120 Hz, do not show any significant changes in the amplitudes of fluctuations in this time interval compared to the portions before the time 93 seconds. The large amplitude fluctuations seen in channel 2 at intervals of about 2 seconds are due to spurious noise which appeared throughout the ascent and in some portion of the descent. This figure, thus shows that the electric field fluctuation associated with the plasma instabilities were detected in the ascent portion between 93 and 115 seconds, corresponding to an altitude range of 87 to 103 km.

Figure 7.6 shows the electric field fluctuations recorded during the descent of the flight 05.17 between 232 and 260 seconds. Here, the data is noise free compared to

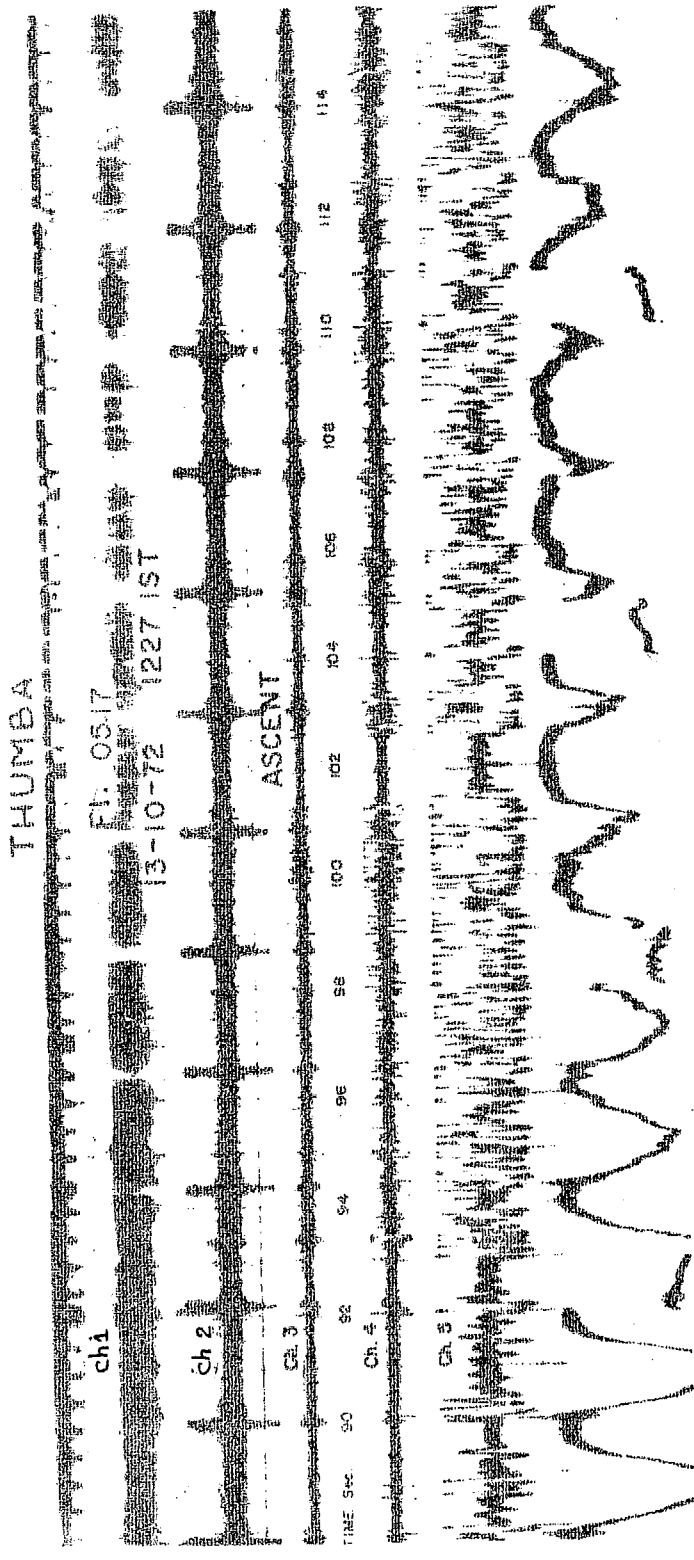


FIG. 7.5. Galvanometric chart record of the raw, horizontal electric field data, (bottommost channel), and the outputs of the five channel spectrum analyser are shown for a portion of the ascent of Fl. 05.17, between 88 and 115 seconds. Presence of AC electric field can be seen in channels 3, 4 and 5, from 93 to 115 seconds, corresponding to the altitude range of 87 to 103 km. The large pulses seen in Ch.2, at regular intervals of 2.2 seconds, are due to spurious oscillations.

THUMBA

F1. 0517

13-10-72 1227 IST

CH 2

CH 3

DESCENT

CH 4

CH 5

TIME Sec 235 237 239 241 243 245 247 249 251 253 255 257 259

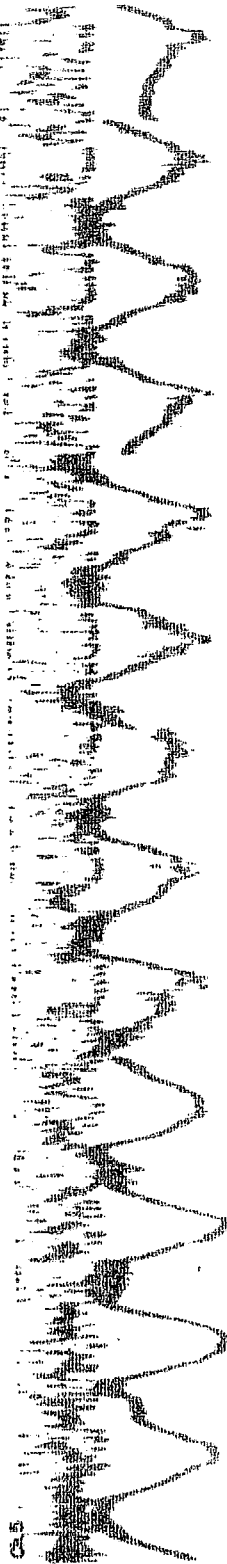


FIG. 7.6. The raw, horizontal electric field data, together with the spectrum analyser outputs are shown for a portion of the descent of F1. 05.17 between 232 and 260 seconds. The presence of AC electric field, can be seen in channels 3, 4 and 5 between 235 and 258 seconds, corresponding to the altitude range of 104 to 88 km. The interfering pulses seen during the ascent (FIG. 7.5) are absent here.

the ascent portion in Figure 7.5, and the spurious noise at 2.2 seconds interval is also absent. In the Figure 7.6, it can be seen that the channels 3, 4 and 5 have recorded electric field fluctuations between 235 and 258 seconds, corresponding to the altitude range of 104 to 88 km.

From Figures 7.5 and 7.6, it can be seen that electric field fluctuations have been detected during the flight 05.17 between 87 to 104 km during the ascent as well as the descent. The fluctuations being seen in the same altitude range in the ascent as well as in the descent confirms that these fluctuations are not spurious or rocket generated effects. No other significant fluctuations were detected in any of the channels at other portions of the flight 05.17.

The interesting findings of the flight 05.17 are confirmed by the results from the flight 05.19 of the second series conducted in March 1973. In the flight 05.19, the electric field fluctuations were detected between 92 and 108 seconds during the ascent and from 256 to 268 seconds in the descent.

The raw data of the horizontal electric field fluctuations and the channel outputs of the spectrum analyser for portions of the ascent and the descent of the flight 05.19 are shown in Figures 7.7 and 7.8. Since the payloads of

THUMBA

Pl. 0519

3-3-73 1135 15T

ASCENT

TIME Sec. 91 92 93 94 95 96 97 98 99 100 101 102 103 104 105

CH 1

CH 2

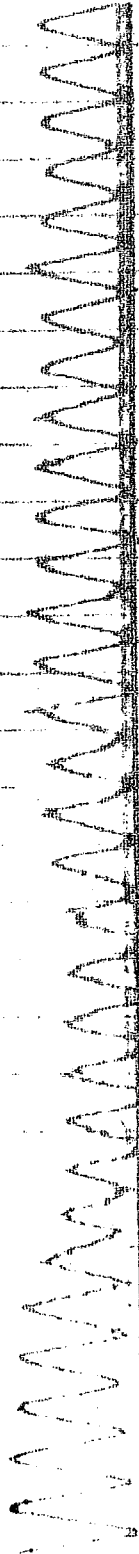


FIG. 7.7. The raw, horizontal electric field data and the outputs of the spectrum analyser are shown for a portion of the ascent of Pl. 05.19 between 88 and 115 seconds. The presence of AC electric field can be seen in channels 3, 4 and 5, between 92.5 and 109 seconds, corresponding to an altitude range of 88 to 102 km.

THUMBA

Fl. 05.19

3-3-75 113515T

DESCENT

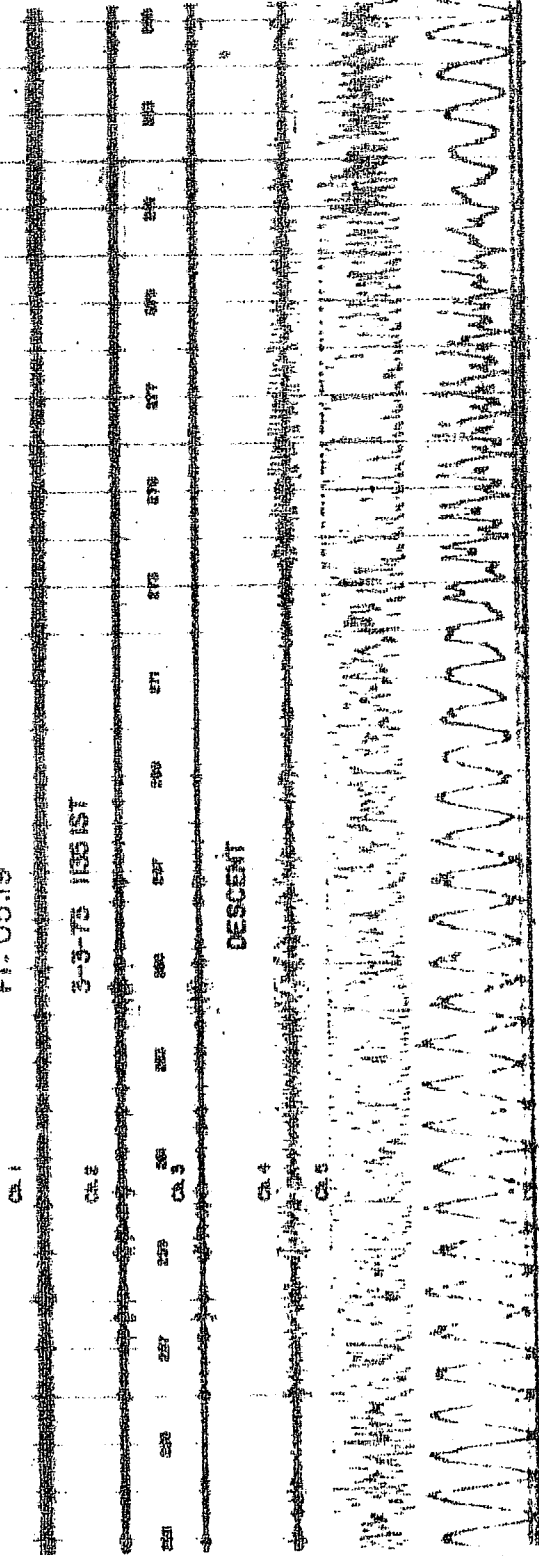


FIG. 7.8. The raw, horizontal electric field data and the outputs of the five channel spectrum analyser are shown for a portion of the descent of Fl. 05.19, between 253 and 280 seconds. The presence of AC electric field, can be seen in channels 3, 4 and 5, between 256 and 269 seconds, corresponding to an altitude range of 98 to 86 km. The large modulations in the raw data (bottom-most channel), between 273 and 280 seconds, are due to rocket tumbling, during reentry.

flight 05.17 and 05.19 were identical and since the data from the two flights have been analysed in the same manner, the results presented separately (in figures 7.5 to 7.8) for the two flights, are comparable.

In Figure 7.7, the data recorded during the ascent of 05.19 between 88 and 115 seconds is shown. Channels 3, 4 and 5 indicate the presence of fluctuations in the time interval of 92.5 seconds and 109 seconds. The record during the interval 88 to 92.5 seconds and 109 to 115 seconds, do not show the presence of the fluctuations. The time interval of 92.5 seconds to 109 seconds, during which fluctuations are seen, correspond to the altitude range of 88 to 102 km.

In Figure 7.8, the data recorded during the descent of 05.19 between 253 seconds and 285 seconds is shown. In this figure, channels 3, 4 and 5 show the presence of the fluctuations between 256 and 268 seconds, corresponding to an altitude range of 98 to 86 km, same as that region in the ascent where the irregularities are seen. The large modulations in the raw data (bottom most channel in the figure) between 273 and 280 seconds is due to the rocket tumbling and must be ignored.

It is clear from the Figures 7.7 and 7.8 that the electric field fluctuations are seen in the altitude region

of 86 to 102 km during both the ascent and the descent, without any ambiguity. No other fluctuations were detected in this flight also, apart from those detected in this altitude range.

7.2.3 Discussion of results:

The detection of electric field fluctuations during the noon time when the electrojet was strong, between the altitudes 86 and 104 km during both ascent and the descent, by two independent rocket experiments confirm that these fluctuations are associated with the plasma instabilities in this particular altitude region of the ionosphere. As pointed out in section 7.2.2a, the electron density gradient and the Hall polarisation field both are parallel and point upward in the altitude region of 90 to 105 km. This makes the altitude region 90 to 105 km particularly suitable for the generation of type II irregularities due to cross-field instability. Hence, the electric field fluctuations detected in the flights 05.17 and 05.19 in the altitude region of 88 to 104 km may be safely attributed to the cross-field instability. Further, from the Figure 7.4, it can be seen that these fluctuations are detected along the east-west direction (at the peaks and troughs of the spin modulated $V \times B$ induced electric field). The fluctuations being

seen in channels 3, 4 and 5 show the frequency of the fluctuations to be within the range of 5 Hz to 120 Hz, which are the lower limit of channel 5 and the upper limit of channel 3 respectively. A rough estimate of the peak to peak amplitude of the fluctuations, made from the raw data shows that the maximum peak to peak amplitude of the observed field fluctuations is of the order of a millivolt/meter.

In the flight 05.19, the drift velocity of electrons exceeded the threshold for the generation of type I irregularities near the electrojet peak. But no fluctuations in the electric field due to the type I irregularities were detected anywhere in this flight. The amplitude of E field fluctuations due to type I irregularities are expected to be smaller than the ones due to type II irregularities. Hence the non-detection of fluctuations attributable to type I irregularities in the flight could be due to the low gain of the electric field detector system used in the experiment. These results show that cross field generated fluctuations in the horizontal component of the electric field were detected in the noon time flights in the altitude range of 86 to 104 km. No fluctuations associated with the type I irregularities were detected, which could be due to the low gain of the system. Hence, detection and study of two-stream instability generated E field fluctuations need further investigation.

7.3 The early morning experiment:

7.3.1 Flight Details:

A Petrel rocket (P.158) carrying an electric field detector was launched from Thumba, on February 9, 1975 at 0559 hours IST. The ground ΔH was not significant at the time of launch, which indicates the presence of a weak or negligible electrojet. The rocket reached an apogee of about 140 km and was tracked by the radar on the skin-track mode. The rocket also carried a Langmuir probe to measure the electron density and its fluctuations.

7.3.2 Payload details and performance:

The electric field detector used in this flight is different from the ones used in the experiments described earlier. In this morning flight, a pair of Copper-Beryllium booms were deployed, 3 meters on either side of the rocket body. The first half portion of the booms of 1.5 meters on both sides from the rocket-body is coated with non-conducting paint so that the other half of the booms of 1.5 meters length from the tips act as the probes with an effective separation distance D of 4.5 meters. The payload was designed to measure the electric field fluctuations from 10 Hz to 100 KHz. Since such a wide frequency range cannot be

telemetered through any sub carrier channel, the data was spectrum analysed on-board. The on-board spectrum analyser had 4 channels. These are: Ch.1, 10 Hz to 100 Hz, Ch.2, 100 Hz to 1 KHz, Ch.3, 1 KHz to 10 KHz, and Ch.4, 10 KHz to 100 KHz. The outputs of these four channels were fast sampled by a commutator and telemetered to the ground. The channel outputs represent the average level of the electric field fluctuations within the pass band of each channel. The raw data of electric field fluctuations was not separately transmitted to the ground.

The electric field probe gave good data from the time of deployment (about 98 km) upto the apogee. A few seconds after the apogee, the electric field detector failed and no useful data was recovered thereafter.

7.3.3 The Results:

The variation of average level of AC electric field with altitude in the frequency bands 10 Hz to 100 Hz, 100 Hz to 1 KHz and 1 KHz to 10 KHz are shown in Figure 7.9. The AC field in the highest frequency band 10 KHz to 100 KHz did not show recognisable change throughout the flight indicating that the AC electric field in this frequency band was not present during this flight. The output of this channel is not shown in the figure. The electron density measured in this flight is also shown in this Figure 7.9.

THUMBA

Fl. P 158, 9.2.75, 0559 IST

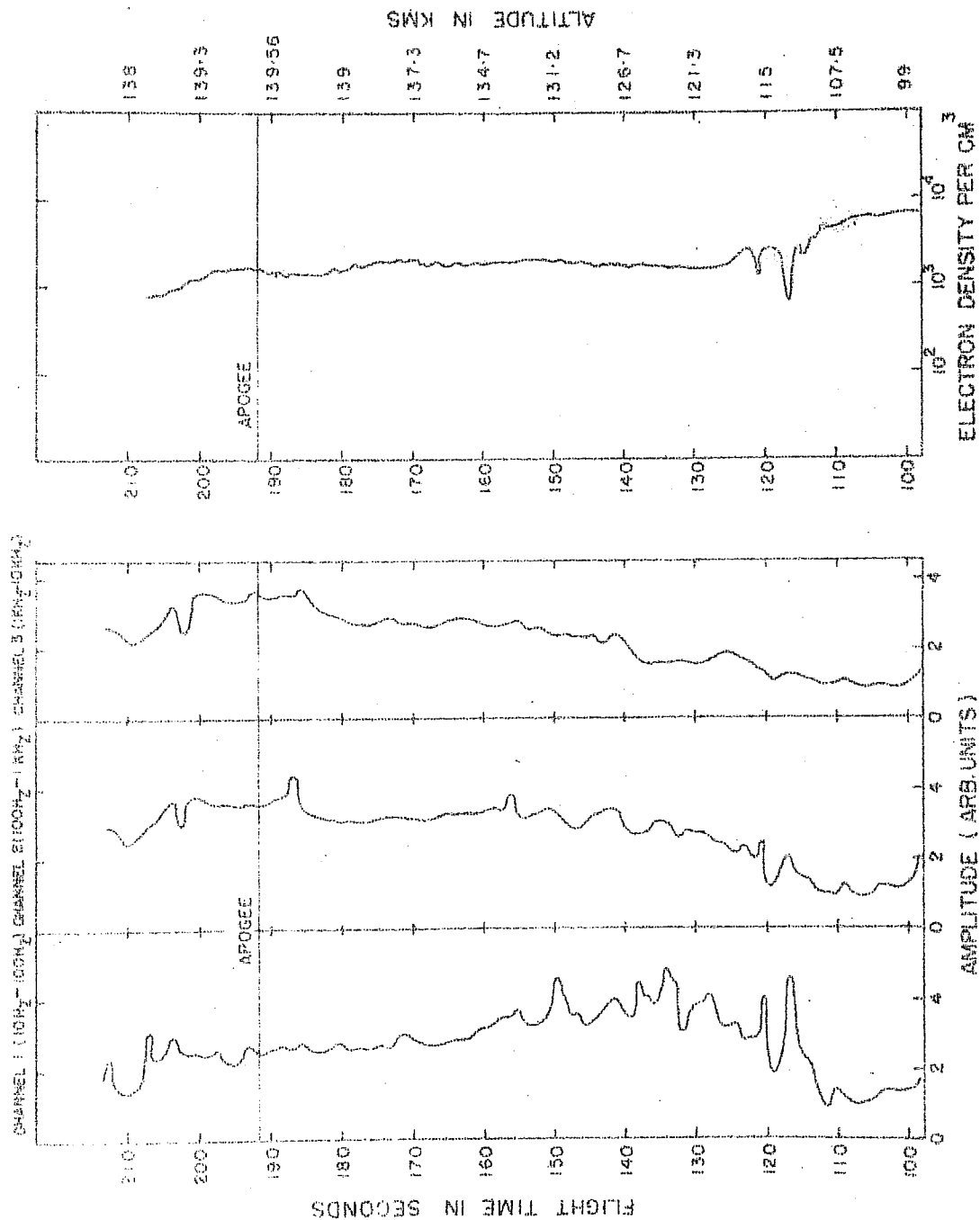


FIG. 7.9. For figure caption, please see overleaf.

FIGURE CAPTION

FIG. 7.9. The average levels of the AC electric field in three spectral bands, 10 Hz to 100 Hz (Channel 1), 100 Hz to 1 KHz (Channel 2) and 1 KHz to 10 KHz (Channel 3), measured during the flight P158 are shown together with the electron density measurements made on the same flight. Large amplitude AC electric field fluctuations in the frequency band of 10 Hz to 100 Hz, were detected between 110 and 131 km. The AC electric field in channel 1 and the electron density, show large changes in the same altitude interval, 110 to 120 km. The large enhancement of AC electric field around the apogee, seen in the high frequency channels 2 and 3, is due to the rocket induced effects.

It is seen from Figure 7.9 that the largest fluctuations in the AC electric field occur in the lowest frequency band, 10 Hz-100 Hz and that the average level of the AC electric field of different frequency bands do not vary in the same way with the altitude. The level of the AC electric field of 10 Hz to 100 Hz band (Ch.1 output), remains steady and quiet between 100 km and 108 km, then it increases sharply near 110 km and shows a broad maximum superposed by large fluctuations between 110 and 131 km. Thereafter, the average AC field level remains steady and quiet towards the apogee. It can be seen that both the low frequency (10 Hz-100 Hz) AC electric field and the electron density measured on the same flight show large changes in the same altitude range 110 and 120 km.

The level of AC electric field of 100 Hz to 1 KHz band (Ch.2 output) is also steady and quiet between 100 and 110 km, then it increases gradually upto 129 km with observable fluctuations, but without showing the broad maxima characteristics of the low frequency channel output Ch.1. The AC field is steady and quiet between 133 and 139 km and just before the apogee, a sudden increase in the field is observed and the field remains significantly high on either side of the apogee.

The AC field level in the frequency band 1 KHz - 10 KHz steadily increases right from 100 km upto the apogee, with small fluctuations superposed on the average level. Just as in Ch.2 output, here also there is a significant enhancement in the AC field level around the apogee.

7.3.4 Discussion of Results:

In the results presented in the figure 7.9, two striking features can easily be observed. First, the AC field in the lowest frequency band (10 Hz - 100 Hz) goes through a broad maximum between 110 and 131 km, and shows large changes in intensity in the same region where the electron density also undergoes large changes. The maximum around the apogee which is the characteristic feature of the higher frequency channels 2 and 3 is not noticeable in the profile of channel 1. The electron density measured on the same flight and shown in Figure 7.9 (Gupta S.P. private communication) shows regions of downward electron density gradients in the altitude intervals 108-113 km, 115-116 km and 117-120 km. Gupta et. al., have detected significant electron density fluctuations at the above mentioned regions of downward electron density gradients. They have ascribed the observed electron density fluctuations to the presence of cross field instability in these regions. It can be seen from the figure

that the AC electric field intensity also increases in the regions of downward electron density gradients where cross field instability has been observed. This indicates that the observed low frequency E field fluctuations can be due to the cross field instability in this region. However, some of the increases observed in channel 1 output are not always well correlated with the downward electron density gradient. Hence, it is necessary to confirm the above findings by further experiments.

The second prominently observable feature in Figure 7.9 is the enhancement of AC electric field level around the apogee in the higher frequency channels Ch.2 and Ch.3. Alpert et. al., (1963) have shown that a vehicle moving in an ionised medium can produce longitudinal ion oscillations in its wake, when the velocity of the vehicle becomes subsonic. The velocity of the rocket becomes subsonic near the apogee and also near the apogee the rocket moves horizontally and one of the probes will be within the wake for the good part of a spin cycle. Therefore, the electric field probe can detect the AC electric field in the wake due to rocket motion in the apogee region. There is some evidence to show that the AC electric field detected in the apogee region must be due to longitudinal ion oscillations in the wake. Gurevich and Pitayevsky (1965) have estimated the frequency of ion

oscillations in the rocket wake to be in the range of 0.1 to 1 times the ion plasma frequency in the region. At the time of the flight, the electron density near the apogee altitude 140 km, was 5×10^3 electrons/cm³. Assuming the ion density is equal to the observed electron density, the ion plasma frequency works out to be about 1 KHz. 1 KHz is near the upper band edge of Ch.2 and also near the lower band edge of channel 3. Hence, both channel 2 and channel 3 show the enhancement of AC field around the apogee with equal prominence. Hence, the observed AC field enhancement near the apogee could be due to the longitudinal ion oscillations in the Rocket wake.

7.4 Conclusions:

1. The two rocket-borne electric field experiments conducted near local noon from Thumba detected for the first time, fluctuations in the horizontal component of electric field, associated with the plasma instabilities within the electrojet. These electric field fluctuations were seen between 85 and 105 km altitudes during both the ascent and the descent in two independent rocket experiments.

2. The observed electric field fluctuations are due to the cross field instability, generated in the altitude region of 85 to 105 km, where the electron density gradient and the vertical Hall field are parallel and upward.
3. The frequency of the observed fluctuations lie in the range of 5 Hz to 120 Hz and are seen in the east-west direction only. No significant fluctuations in E field were seen in the magnetic north-south direction along the field line. A rough estimate shows that the peak to peak amplitude of the observed oscillations to be about one millivolt/meter.
4. No AC electric field attributable to type I irregularities were detected in the experiments. This could be due to the low gain of the E field detector system used in the experiment.
5. In the early morning experiment, AC electric field fluctuations associated with the cross field instability were seen in low frequency band 10 Hz - 100 Hz in the altitude range 115-130 km, especially in the regions of downward electron density gradient.

5. Rocket generated electric field fluctuations were detected around the apogee, the frequency of AC field being 1 KHz. The detected electric field could be due to the longitudinal ion oscillations in the wake.

8.1

The study of the equatorial electrojet by simultaneous rocket-borne and ground based measurements of magnetic field has shown that the strength of the electrojet varies in accordance with the ground magnetic field variation, during the course of a magnetically quiet day. Parameters of the electrojet such as the thickness of the current layer, altitude of the current density maximum and the distribution of current density in the jet do not change significantly during a quiet day. No significant current flows - in either direction - during the night of magnetically quiet days. These results are conformatory to the results of preliminary studies of EEJ over Thumba presented by earlier workers from time to time.

It is significant that the rocket measured current density, peaks at a distinctly higher altitude, higher by about 6 km, compared to the altitude of cowling conductivity (σ_3) maximum, calculated by using model values of ionospheric parameters. Similar discrepancy is seen in the results of measurements of Maynard, Davis et. al., and Shuman, conducted from USNS Croatan in the Peruvian region, which are summarised by Richmond (1973). Extensive data spread over several years, available from Thumba, trajectory

determination done to a fairly good degree of accuracy by different investigators on board USNS Croatan as well as at Thumba show that this discrepancy is real and cannot be explained away by trajectory errors. The reason for the observed discrepancy must be sought in the inaccuracies of vertical distributions of ionospheric parameters used in the EEJ models.

The study of the day-to-day variability of electrojet parameters has shown that large day-to-day changes in the amplitude of H variation observed on quiet days are due to changes in the strength of the electrojet itself. Magnetospheric contribution to the day-to-day variability of the strength of the electrojet appears to be negligible. Observed day-to-day changes in the width, thickness, altitude of the current layer and the extent of the region in which the current flows are too small to account for the large day-to-day changes in H variation amplitude in the EEJ region. These parameters appear to be intimately bound to the configuration of geomagnetic field lines over the dip equator, which hardly changes from one day to another on quiet days. The study leads us to the changes in the velocity of the winds that control the electric fields in the region of the electrojet as the major source of day-to-day variability of the strength of the electrojet and consequently the H variation

amplitude. It also gives us a clue to the nature of these winds and electric fields. The study shows that any wind system proposed to explain the day-to-day variability of geomagnetic field in the EEJ region must be such that, it brings about large day-to-day changes in the electrojet strength only but do not produce appreciable changes in the geometric parameters of the equatorial electrojet. Also one can expect that the E fields responsible for the day-to-day variability, to exhibit large day-to-day changes in intensity but not significantly in its vertical distribution. However, to check whether winds and electric field alone are responsible for large day-to-day variability of H amplitude, it is very necessary to measure, the current density, electron density, DC electric field and day time neutral wind velocities simultaneously in the EEJ region on normal, low and high jet days.

The results from the study of the diurnal and day-to-day variability of the EEJ leads us to the possibility of predicting the vertical profile of current density in the jet, on quiet days, given the magnetogram from a station under the jet. The vertical profile of current density can be predicted with confidence for morning, noon and afternoon hours, for days when J_{\max} does not exceed 14 amp/km^2 or for $\Delta H \leq 135 \text{ nT}$. For dawn and dusk periods, which are

dominated by large electron density gradients, and rapid changes in electron density, and for days of abnormally strong electrojets with $\Delta H > 140$ nT the prediction proposed here, may not be valid. On such days and for dawn and dusk periods, the vertical distribution of current density must be obtained by actual in-situ measurements.

The restriction on the valid prediction of the vertical profile of current density on high jet days arises mainly from the possible modification of current density profile due to stabilisation of two stream instability in the EEJ as predicted by Rogister and Sato. The current density profiles obtained on high jet days during our experiments, however do not show either any significant reduction in peak current density or signs of redistribution of current density in the jet upto $J_{\max} = 14 \text{ amp/km}^2$ and $\Delta H \leq 140$ nT. Whether the effects of stabilisation of two stream instability comes into effect on high jet days with $\Delta H > 140$ nT is open for investigation. This is an important result in view of the fact that efforts are being made to explain the so called 'effect of stabilisation' by including them in wider EEJ models (for instance Richmond 1973), when no such effects are evident in the experimental results obtained so far.

The study of the magnetic data from the ground stations and in-situ measurements further show that a simple uniform current band electrojet model that takes into account the earth induced currents can explain the observed ground magnetic variation in terms of rocket measured electrojet strength. The magnetic field values calculated from a simple EEJ model agree with the observed field at the ground, within ± 5 nT. This study and the study of results from other investigations, in particular, the results from POGO and the Indian Ocean Survey indicate that the depth of the conducting layer cannot be less than 250 km in the Indian zone around Thumba. Based on this value of d , the ratio $H(\text{int})$ to $H(\text{ext})$ for the Indian zone is 0.4.

8.2

The unique magnetometer experiment launched during the maximum depression of a storm main phase showed that the electrojet remained unaffected during the main phase. There were indications in the flight results, of the effects of an eastward electrojet current flow whose magnetic effect at the ground is about 10 nT. Analysis of data from the ground stations showed that such a jet at the time of the flight would be normally expected on quiet days, when no storm is present. The net effect of the storm depression and the normal eastward electrojet was such that it produced a

systematic decrease in the depression of the magnetic field at the ground as the center of the electrojet is approached from higher latitudes. Looking at this result in another way, it shows that the storm depression observed at the ground stations under the jet would have been larger and more uniform if the normal electrojet was absent at the time of the rocket launch.

8.3 A preliminary experiment to measure the increase in electron temperature due to the flow of electrojet currents in the E region, has shown that it is possible to detect the joule heating effect of electrons by the currents of EEJ, using a clean Langmuir probe. Simultaneous measurement of electrojet current density and electron temperature in this experiment, at a time when the jet was strong ($\Delta H = 120$ nT), showed that the measured electrojet strength can account for only one third of the observed joule heating effect. It is known that electron temperatures measured by probe method are always higher than values obtained from back scatter methods. If this is true for the E region T_e measurements also, then the above discrepancy between the observed and calculated joule heating effect will be reduced. Whether further improving the technique of measurement of T_e will bring the two values nearer is open

for investigation. Also, the observed excess temperature ($T_e - T_g$), that finally represents the joule heating effect is evaluated using CIRA model neutral gas temperature values. At present no experimentally determined T_g values over the equator are available. Future experiments must measure J , T_e and T_g simultaneously, when the EEJ is strong to see whether the observed discrepancy can be explained.

8.4 Two series of rocket experiments - one in October 1972 and another in April 1973 - were conducted to detect AC electric field (or electric field fluctuations) associated with the plasma instabilities in the equatorial electrojet. Both experiments detected electric field fluctuations in the region between 85 and 105 km altitude. Near simultaneous measurements of J , N_e and AC electric fields during the above series of experiments showed that the observed E field fluctuations are due to cross field instability, generated in the region between 85 and 105 km, where the electron density gradient and the Hall field are parallel and directed upward. These fluctuations were seen in the east-west direction only. No significant AC fields were seen in the magnetic north-south direction along the field line. A spectral analysis of observed electric field fluctuation showed that the frequency of the AC electric

field associated with the crossfield instability, detected during the experiments, lie in the range 5 Hz and 120 Hz. A rough estimate showed that the peak-to-peak amplitude of the detected fluctuations to be one millivolt/meter.

A third experiment was carried out in February 1975 to study the nature of instabilities that may be present during the early morning hours, and the AC field associated with these instabilities. Presence of cross field instability and AC electric field in the low frequency band 10 Hz-100 Hz associated with this instability were detected, especially in the regions of downward electron density gradient in the altitude range 115-130 km. Rocket generated electric field fluctuations of frequency around 1 KHz, probably due to longitudinal ion oscillations in the wake, were detected near the apogee.

8.5

The study of the equatorial electrojet presented here, has confirmed some of the earlier findings of the diurnal and day-to-day variability of equatorial electrojet. The extensive data available from in-situ measurements from a single station, Thumba, has enabled a systematic study of the behaviour of the EEJ, the variability of its parameters and the relationship of these variabilities with the changes of magnetic field at the ground. Consequently, it

has now become possible to accept the earlier evaluations of the parameters of the electrojet and the deductions concerning the behaviour of the electrojet with much more confidence. As a result, it now appears possible to predict the vertical distribution of current density in the equatorial electrojet on quiet days, using the information from ground magnetogram alone, without recourse to an actual rocket launch.

The study also has brought in new results, concerning the effect of storm main phase on EEJ current flow, the joule heating of electrons due to flow of currents in the EEJ and the effect of stabilisation of two stream instability in the EEJ on abnormally high jet days.

For the first time, electric field fluctuations associated with the plasma instabilities in the electrojet region were detected in three separate experiments. It was possible in these experiments to successfully identify the electric field fluctuations associated with cross-field instability as against rocket generated instabilities and analyse the spectral distribution of AC field generated by these instabilities. Future experiments at Thumba are planned to explore the EEJ instability

and associated electric field fluctuations with simultaneous measurements of magnetic field and electron density fluctuations under different magnetic and ionospheric conditions. This will enable the understanding of the nature, generation, maintenance and propagation of plasma instabilities associated with the equatorial electrojet.

REFERENCES

- Akasofu S.I. and Chapman S., Planet. Space Sci. 12, 6070 (1964).
- Akasofu S.I., Meng C.I. and Chapman S., Proc. of 3rd Int. Symp. on Eq. Aeron. Ahm, India., (1969).
- Allredge, L.R., Physics of Geomagnetic phenomena, Ed. S. Matsushita and W.H. Campbell., Vol. I, (1967).
- Alpert Y.L., Gurevitch A.V. and Pitayevsky L.P., Space Res. III, 1224, (1963).
- Baker W.G. and Martyn D.F., Nature 170, 1090, (1952).
- Baker W.G. and Martyn D.F., Phil. Trans. Roy. Soc. London A 246, 281, (1953).
- Balsley B.B., Report on Eq. Aero. in Proc. of 2nd Int. Symp. in Eq. Aero. 300, (1965).
- Balsley B.B., J. Atmos. Terr. Phys. 31, 475, (1969).
- Balsley B.B., J. Atmos. Terr. Phys. 35, 1035, (1973).
- Banks P.M., Planet Space Sci. 14, 1085, (1966).
- Bartels J. and Johnston H.F., J. Geophys. Res. 45, 269, (1940).
- Bell W.E. and Bloom A.L., Phys. Rev. 107, 1559, (1957).
- ✓ Bhargava B.N., Proc. of III Int. Symp. on Eq. Aero. held at Ahmedabad, India, p346, (1969).
- Blacquiere A., Bonnett G. and Grivet P., Proc. 3rd Quantum Electr. Cong. 1963, Dunod, Paris, p231, (1964).
- Brace L.H., Carignan G.R. and Findlay J.A., Space Res. XI, 1079, (1970).
- Buneman O., Phys. Rev. Lett. 10, 285, (1963).
- Burrows K., J. Atmos. Terr. Phys. 38, 159, (1976).
- Burrows K. and Sastry T.S.G., J. Atmos. Terr. Phys. 38, 307, (1976).
- Burrows K., Sastry T.S.G., Sampath S., Stolarik J.D. and Usher M.J., Presented in the COSPAR XVII Plenary meeting at Philadelphia, Penn., USA. (1976).
- Cahill L.J., J.G.R., 64, 489, (1959).
- Cahill L.J. and Van Allen., J.G.R., 61, 547, (1956).
- Cain J.C. and Sweeny R.E., J. Atmos. Terr. Phys. 35, 1231, (1973).

- Cain J.C., Hendricks S., Daniels W.E. and Jensen D.C.,
NASA-GSFC Rep. X-611-64 316-Oct. 1964, (1964).
- Chapman S., Terr. Magn. Atmos. Elect. 53, 247, (1948).
- Chapman S., Arch. Met. Geophys. Bioklion, 4, 368, (1951).
- Chapman S. and Bartels J., Geomagnetism Vol. I & II, (1940).
- Chapman S. and Raja Rao K.S., J.Atmos.Terr.Phys. 27, 559, (1965).
- ✓ Ching B.K. and Chiu Y.T., Planet. Space Sci. 21, 1633, (1973).
- Closs R.L., J.G.R. 72, 3987, (1967).
- Cloutier P.A. and Haymes R.C., J.G.R. 73, 1771, (1968).
- Cohen R., Phys. of Geomagn. Phen. Edt. S.Matsushita and
Campbell W.H., Vol. I, (1967).
- Cohen R. and Bowles K.L., J.G.R. 68, 2503, (1963).
- Cohen R., Bowles K.L. and Calvert W., J.G.R. 67, 965, (1962).
- Cole K.D., Aust. J. Phys. 15, 223, (1962).
- Cowling T.G., Monthly Notices Roy. Astron. Soc. 93, 90, (1932).
- Dalgarno A., Mcelory M.B. and Moffett R.J., Planet. Space
Sci. 11, 463, (1963).
- Davies K., Ionospheric Radio Propagation, Dover Publ. N.Y.
Ch.3, (1966).
- Davis T.N., Burrows K. and Stolarik J.D., J.G.R. 72, 1845, (1967).
- Davis T.N., Stolarik J.D. and Heppner J.P., J.G.R. 70,
5883, (1965).
- Dehmelt H.G., Phys. Rev. 105, 1924, (1957).
- Dolginov Sh. Sht., Geomagn. and Aero. 12, 611, (1972).
- Driscoll R.L. and Bender P.L., N.B.S. Tech. News Bull.
42, 217, (1958).
- Dunford E., J.Atmos.Terr.Phys. 29, 1489, (1967).
- Egedal J., Terr. Magn. Atmos. Elect. 52, 449, (1948).
- Fahleson U.V., Space Sci. Rev. 7, 238, (1967).
- Fambitakoye O. and Mayaud P.N. J.Atmos.Terr.Phys. 38,1, (1976A).
- Fambitakoye O. and Mayaud P.N., J.Atmos.Terr.Phys. 38,19, (1976B).
- Fambitakoye O. and Mayaud P.N., J.Atmos.Terr.Phys. 39, 123 (1976C).
- Fambitakoye O., Mayaud P.N. and Richmond A.D., J.Atmos.Terr.
Phys. 39, 113, (1976).

- Farley D.T., Phys. Rev. Lett. 10, 504, (1963).
- Ferraro V.C.A. and Unthank H.W., Geofri. Pure E. Appl. 20, 27, (1951).
- Forbush S.E. and Vestine E.H., J.G.R. 60, 299, (1955).
- Forbush S.E. and Casavarde M., Carnegie Inst. Wash. Publ. 620, (1961).
- Farthing W.H. and Folz W.C., Rev. Sci. Instr. 38, 1023, (1967).
- Geisler J.E. and Bowhill S.A., J.Atmos.Terr.Phys. 27, 457, (1965).
- Giesecke A.A., Tran. Brussels Meeting 1951, (1951).
- Gouin P., Nature 193, 1145, (1962).
- Grivet P.A. and Malnar L., Advances in Electronics and Electr. Phys. 23, 39, (1967).
- Gruenberg R.C., Hand Bk. of Tele. and Remote Controls, (1967).
- Gulate B.L., Survey Ind. Tech. Rept. Pt. 3, (1950).
- Gurevitch A.V. and Pitayesky L.P., Phys. Rev. Lett., 15, 346, (1965).
- Hanson W.B., Space Res. III, 282, (1962).
- Hanson W.B. and Johnson F.S., Mem.Roy.Soc. Leige 4, 390, (1961).
- Hanson W.B., Brace L.H., Dyson P.L. and Mc Clure J.P., J.G.R. 74, 400, (1969).
- Harris I. and Priester W., J.Atmos.Sci. 19, 286, (1962).
- Hasegawa M., Proc. Imp. Acad. Tokyo 12, 185, (1936).
- Hasegawa M., J. Geophys. Res. 65, 1437, (1960).
- Hirao K. and Oyama K., J.Geomag.Geolect. 22, 303, (1970).
- Hirono M., J.Geomagn.Geolect. 2, 113, (1950).
- Hirono M., J. Geomagn. Geolect. 4, 7, (1952).
- Hutton R., J.Atmos.Terr.Phys. 29, 1411, (1967).
- Hutton R. and Oyinloye J.O., Ann.Geophys. 26, 921, (1970).
- Jensen D.C. and Cain J.C., J.G.R. 67, 3568, (1962).
- Johnston H.F. and Mc Nish A.G., C R Congr. Int. Elect. Paris 12, 41, (1937).
- Kane R.P., J.Atmos.Terr.Phys. 33, 319, (1971).
- Kane R.P., J.Atmos.Terr.Phys. 34, 73, (1972).
- Kane R.P., J.G.R. 78, 5585, (1973).

- Kane R.P., Proc. Ind. Acad. Sci. 80A, 17, (1974).
- Kane R.P., Space Sci. Rev. 18, 413, (1976).
- ✓ Kato S., Planet. Space Sci. 11, 1297, (1963).
- Kato S., J. Atmos. Terr. Phys. 35, 1073, (1973).
- Kato S. and Hirata Y., Rep. Ionosp. Space Res. Japan 21, 85, (1967).
- Knapp D.G. and Gettmy J.W., J.G.R. 68, 2411, (1963).
- Madwar M.R., Bull. Inst. Egypt. 36, 5, (1953).
- Maeda K., J. Geomagn. Geoelect. 4, 63, (1952).
- Maeda K. and Matsumoto H., Rept. Ionosph. Space Res. Japan 16, 1, (1962).
- Maeda K.I., Tsuda T. and Maeda H., Rep. Ionosph. Space Res. Japan 17, 147, (1963).
- Matsushita S., J. Geomagn. Geoelect. 3, 44, (1951).
- Matsushita S., J.G.R. 65, 1423, (1960).
- Matsushita S., Physics of Geomagnetic Phenomena, Ed. Matsushita and Campbell., (1967).
- ✓ Matsushita S., J. Atmos. Terr. Phys. 35, 1027, (1973).
- Matsushita S. and Maeda H., J.G.R. 70, 2535, (1965).
- Mayaud P.N., Ann. Geophys. 21, 369, (1965).
- Maynard N.C., J.G.R. 72, 1863, (1967A).
- Maynard N.C., Ph.D. Thesis, Univ. New Hampshire, USA, (1967B).
- Maynard N.C., Proc. Advanced study Institute on Magnetosphere Ionosphere Interaction Ed. Folkestad 155, (1971).
- Maynard N.C. and Cahill L.J., J.G.R. 70, 5923, (1965).
- Maynard N.C., Cahill L.J. and Sastry T.S.G., J.G.R. 70, 1241, (1965).
- Mc Dougall J., Proc. III Int. Symp. on Equa. Aero. Ahm., India, Vol. II, P269, (1969).
- McNish., Terrst. Magn. Atmos. Electr. 43, 67, (1938).
- Mitra S.K. Proc. IEE Pt. C, 96, 441, (1949).
- Mozar F.S. Proc. of 1968 COSPAR Symp. on Small Rocket Instr. Tech., N. Holland., (1969).
- Mozar F.S., Space Sci. Rev. 14, 272, (1973).
- Ness N.F., Space Sci. Rev. 11, 459, (1970).

- Nishida A.N., Iwasaki N. and Nagata T., Ann. Geophys. 22, 478, (1966).
- ✓ Obayashi T., Proc. of III Int. Symp. on Eq. Aero. held at Ahm., I ND, P460, (1969).
- Obayashi T. and Maeda K., Problems of Atmospheric and Space Electricity, Ed. S.C. Coroniti, (1965).
- Ogubuehi P.O. and Onwumuchilli A., J. Atmos. Terr. Phys. 26, 889, (1964).
- Ogubuehi P.O., Onwumuchilli A. and Ifedili S.O., J. Atmos. Terr. Phys. 29, 149, (1967).
- Olson W.P., J.G.R. 75, 7244, (1970).
- Onwumuchilli A., J. Atmos. Terr. Phys. 13, 222, (1959).
- Onwumuchilli A., Phys. of Geomag. Phenomena., Ed. Matsushita and Campbell, (1967).
- Onwumuchilli A. and Alexandar N.S., J. Atmos. Terr. Phys. 16, 106, (1959).
- Osborne D.G., J. Atmos. Terr. Phys. 30, 1479, (1968).
- Packard M. and Varian R., Phy. Rev. 93, 941, (1953).
- Pedersen P.O., Danmarks Natur. Sansfurd, Copenhagen, (1927).
- Pontier L., Ann. Geophys. 6, 238, (1950).
- ✓ Prakash S., Gupta S.P., Rao T.R., Sampath S. and Sastry T.S.G., Presented at the XVI COSPAR Symp. at Varna, Bulgaria, (1975).
- Prakash S., Gupta S.P., Subbaraya B.H. and Jain C.L., Nature 233, 56, (1971).
- Pramanik S.K. and Hariharan P.S., Ind. J. Met. Geophys. 4, 353, (1953).
- Pramanik S.K. and Yegnanarayanan., Ind. J. Met. Geophys. 3, 212, (1952).
- Price A.T. and Stone D.J., Ann. Int. Geophys. Yr. 35, 63, (1964).
- Price A.T. and Wilkins G.S., Phil. Trans. R. Soc. 256, 31, (1963).
- Raja Rao K.S., Ind. J. Met. Geophys. 13, 97, (1962).
- Raja Rao K.S., Ind. J. Radio Space Phy. 1, 12, (1972).
- Raja Rao K.S. and Joseph K.T., J. Atmos. Terr. Phys. 33, 1793, (1971).

- Rao K.N. and Raja Rao K.S., Nature 200, 460, (1963).
- Rastogi R.G., J. Geophys. Res. 69, 1020, (1964).
- Rastogi R.G., J. Atmos.Terr.Phys. 35, 367, (1973).
- Reid G.C., J.G.R. 73, 1627, (1968).
- Richmond A.D., J.Atmos.Terr.Phys. 35, 1083, (1973).
- Roble R.G. and Dickinson R.E., J.G.R. 78, 249, (1973).
- Rogister A., J.G.R. 76, 7754, (1971).
- Rogister A., J.G.R. 77, 2975, (1972).
- Rogister A. and D'Angelo N., J.G.R. 75, 3879, (1970).
- Rohitiyansky I.I., Geomagn. and Aero. 9, 726, (1969).
- Ruddock K.A., Space Res. II, 692, (1961).
- Rush C.M. and Richmond A.D., J.Atmos.Terr.Phys.35,1171, (1973).
- Sampath S., Sastry T.S.G., Oyama K. and Hirao K., Space Res. XIV, 253, (1974).
- Sampath S. and T.S.G. Sastry., Proc. of Solar Planetary Physics Symp. held at PRL Ahmedabad, (1976).
- Sastry T.S.G., J. Sci. Industr. Res. 23, 334, (1964).
- Sastry T.S.G., Space Res. X, 778, (1970).
- Sastry T.S.G., Gerland Beitr. Geophys. 80, 253, (1971).
- Sastry T.S.G., J.G.R. 78, 1692, (1973).
- Sastry T.S.G., H.S. Mazumdar and S. Sampath., Ind. J. Radio Space Phys. 4, 60, (1975).
- Sato T., J.G.R., 73, 2941, (1968).
- Sato T., Phys. Rev. Lett. 28, 732, (1972).
- Sato T., J. Geophys. Res. 78, 2232, (1973).
- Satya Prakash, Gupta S.P., Subbaraya B.H., Sinha H.S.S. and Jain C.L., Rev. Paper presented at Lloyd Berkener Symp. held at Univ. of Texas, Dallas, USA, (1973).
- Schieldge J.P., Venkateswaran S.V. and Richmond A.D., J. Atmos. Terr. Phys. 35, 1045, (1973).
- Shankar Narayan P.V. and Ramanujachary K.R., Nature 231, 37, (1971).
- Shuman B.M., J.G.R. 75, 3889, (1970).

Singer S.F. Maple E. and Bowen W.A., J.G.R. 56, 265, (1951).
 Skadron G. and Weinstock J., J.G.R. 74, 5113, (1969).
 Smith L.G., Proc. of 1968 COSPAR Symp. on Small rocket Inst.
 Tech., N. Holland., (1969).
 Stening R.J., J.Atmos.Terr.Phys. 31, 849, (1969).
 Sugiura M., J.G.R. 38, 558, (1953).
 Sugiura M. and Cain J.C., J.G.R. 74, 1869, (1966).
 Sugiura M. and Poros D.J., J.G.R. 74, 4025, (1969).
 Sugiura M. and Poros D.J., GSFC-X-641-71-278, (1971).
 Suzuki A., J.Geomagn.Geolect., (1973).
 Untiedt J., J.G.R. 72, 5799, (1967).
 Van Sabben D., J.Atmos.Terr.Phys. 26, 1187, (1964).
 Van Sabben D., J.Atmos.Terr.Phys. 28, 965, (1966).
 Vestine E.H., J.G.R. 58, 560, (1953).
 Vestine E.H., La Porte L., Lange I. and Scott W.E., Carnogie
 Inst. Wash. Publ. 580, (1947).
 Waldteufel P., Ann.Geophys. 21, 579, (1965).
 Walker J.C.G., Planet. Space Sci. 16, 321, (1968).
 Waters G.S., Nature 176, 691, (1955).
 Waters G.S. and Francis P.D., J.Sci. Instrum. 35, 88, (1958).
 Whitehead J.D., J.Atmos.Terr.Phys. 29, 1288, (1967).
 Willmore A.P., Proc. Roy.Soc. 281, 140, (1964).
 Yabuzaki., Ph.D. Thesis, Kyoto Univ., Kyoto, Japan, (1973).
 Yabuzaki. and Ogawa T., J.G.R. 79, 1999, (1975).
 Yacob A., J.Atmos.Terr.Phys. 28, 580, (1966).
 Yacob A. and Khanna K.B.K., Ind.J.Met.Geophy. 14, 470, (1963).
 Yamura., Mem. Kakioka Mag. OBS. 7, 24, (1954).

Reprint from:

COSPAR

SPACE RESEARCH XIV

Proceedings of Open Meetings of Working Groups
of the Sixteenth Plenary Meeting of COSPAR

Constance, F.R.G. — 23 May—5 June 1973

and

Resumés of the
Symposium on Noctilucent Clouds and Interplanetary Dust

Constance, F.R.G. — 24 and 25 May 1973

Edited by

M. J. RYCROFT

R. D. REASENBERG



AKADEMIE-VERLAG · BERLIN

1974

JOULE HEATING DUE TO THE EQUATORIAL ELECTROJET AS OBSERVED BY ROCKETBORNE PROBES

S. SAMPATH^a, T. S. G. SASTRY^a, K. OYAMA^b and K. HIRAO^b

^a Physical Research Laboratory, Ahmedabad, India

^b Institute of Space and Aeronautical Science, University of Tokyo, Tokyo, Japan

A Nike-Apache rocket carrying a proton precession magnetometer and an electron temperature probe was launched on a magnetically quiet day, near noon, from Thumba, India. The purpose of the experiment was to study Joule heating in the E region of the ionosphere, due to the equatorial electrojet current. The current density (J) profile derived from the magnetometer data, the electron temperature (T_e) profile obtained from the electron temperature probe and the neutral temperature (T_g) profile from the CIRA model are used to study the Joule heating effect. The excess of electron temperature over that of the neutrals $T_e - T_g$, which is a consequence of Joule heating, correlates well with the current density J . To relate J and $T_e - T_g$ quantitatively the Cowling conductivity (σ_c) profile and the calculated profile of mean fractional energy loss per collision (λ) of electrons with the neutrals are used. The energy needed to give the observed increase in temperature, $T_e - T_g$, has also been calculated theoretically and compared with the energy delivered by the electrojet.

1. Introduction

The electron temperature distribution under equilibrium conditions is determined by the rate of heat input to the ambient electron gas and the rate of energy loss by various loss processes. A general heating is produced by the absorption of solar radiation. Much of the absorbed energy appears as kinetic energy of photoelectrons. The energetic photoelectrons lose their energy to the ambient electrons, ions and neutrals. It is assumed that the ambient electrons suffer frequent elastic collisions among themselves and attain a Maxwellian distribution, characterized by the electron temperature T_e . The ions and neutrals, except in the upper F region, attain equilibrium amongst themselves and are considered to have a common temperature T_g . The electron gas cools by collisions with neutrals and ions. The heat loss to positive ions is important only above 200 km, while below this height the heat loss to neutrals is more important.

Theoretical electron temperature profiles based on the above mentioned assumptions have been derived by various workers [1—4]. It is found that the electron temperature increases with height throughout the ionosphere. T_e is equal to T_g below 150 km, above which T_e exceeds T_g . The difference $T_e - T_g$ increases above 150 km and reaches a maximum near 250 km. According to these findings there is no thermal non-equilibrium below 150 km. These conclusions are based upon the assumption that radiation from the sun is the only source of heat energy

and that local heating effects such as Joule heating are negligible. However, for calculating the temperature distribution in the equatorial and auroral ionospheres, Joule heating effects have to be taken into account.

Joule heating in the equatorial E region due to the electrojet has been studied theoretically by Kato [5]. Joule heating affects the thermal equilibrium, by raising T_e above T_g in a way similar to the heating produced by the absorption of solar radiation. In the present discussion, the energy produced by Joule heating is related to the observed increase in T_e over T_g under the assumption that the energy loss of electrons by collisions with neutrals is the only loss process.

2. Flight Data

A Nike-Apache rocket carrying a proton precession magnetometer, an electron temperature probe, a capacitance probe and a gyro-plasma probe, was launched on a magnetically quiet day, 25 April 1971 ($Kp = 2$) at noon from Thumba, near the magnetic dip equator. The proton magnetometer and the electron temperature probe gave satisfactory measurements during the ascent up to 160 km. The electron temperature probe used in this experiment is the same as that described in [6].

3. Flight Results

The proton magnetometer measured a difference field ΔH of $\pm 110 \gamma$ as it traversed the electrojet. The vertical distribution of electric current density is derived from the slope of the difference field by the usual method [7]. The electron temperatures measured by the temperature probe and the gas temperature given by the CIRA 1965 model have been used to derive the temperature difference

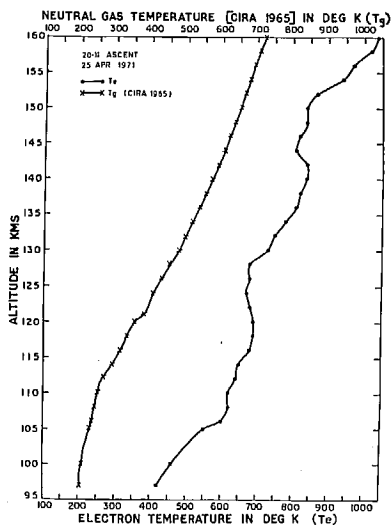


Fig. 1. Vertical profiles of measured electron temperature T_e and the CIRA 1965 model neutral gas temperature T_g .

$T_e - T_g$. Since the electron density measurements from the same flight were not available, vertical profile of electron density obtained by a rocketborne probe launched from the same range under similar magnetic conditions, near local noon, has been used here [8]. The Cowling conductivity (σ_3) profile is calculated, taking

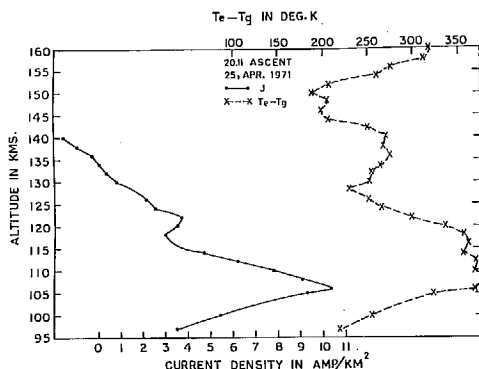


Fig. 2. The current density J derived from the magnetometer data and the difference temperature $T_e - T_g$ plotted as functions of altitude.

the σ_1 and σ_2 profiles of Maeda and Matsumoto [9]. The vertical profile of the electron temperatures obtained from the measurements is shown in Fig. 1, together with the CIRA 1965 model gas temperature profile. The current density J derived from the magnetometer is shown in Fig. 2.

4. Calculations

The power generated by the electrojet is calculated and correlated with the observed difference $T_e - T_g$. It is assumed that this difference $T_e - T_g$ is due to the electrojet currents only. The power Q generated by Joule heating can be written as

$$Q = J^2/\sigma_3. \quad (1)$$

The heat input by the electrojet Q_E is obtained as a function of altitude, and is shown in Fig. 3.

If we consider that the loss of energy due to collisions alone is important, under equilibrium conditions, the balance between the heat input by Joule heating and power dissipation by collision with neutral particles is soon established. Following Kato [5] the energy input can be written

$$Q = \frac{3}{2} k n_e n_e \lambda (T_e - T_g) \quad (2)$$

where k is Boltzmann's constant, n_e is the electron density, ν_e is the collision frequency of electrons with neutrals and λ is the mean fractional energy loss per collision. From (1) and (2)

$$\lambda = \frac{2}{3} \frac{J^2}{\sigma_3} \frac{1}{k n_e \nu_e (T_e - T_g)}. \quad (3)$$

By putting in the known values of J , σ_3 , $T_e - T_g$, n_e and n_e , the parameter λ is calculated as function of altitude. This profile is shown in Fig. 3.

In order to obtain an estimate of Joule heating, the heat input needed to give the observed increase in temperature is calculated. Following Dalgarno et al. [2], if Q_T is the energy transferred to the electron gas in unit time, at equilibrium,

$$Q_T = -\frac{3}{2} k n_e \left\{ \left(\frac{dT_e}{dt} \right)_O + \left(\frac{dT_e}{dt} \right)_{N_2} + \left(\frac{dT_e}{dt} \right)_{O_2} + \left(\frac{dT_e}{dt} \right)_+ \right\} \quad (4)$$

where dT_e/dt is the rate of temperature change by the electrons in collision with the neutrals, the neutral species being denoted by subscripts. In the present case the last term, which denotes the loss due to collisions with positive ions, is neglected. The expressions adopted for these calculations are

$$\left(\frac{dT_e}{dt} \right)_O = -10^{-14} n(O) T_e^{1/2} (T_e - T_g) \quad (5)$$

$$\left(\frac{dT_e}{dt} \right)_{N_2} = - \left\{ 7.6 \times 10^{-16} T_e + \left(\frac{G\bar{\nu}}{n(N_2)} \right)_{\text{rot}} \right\} n(N_2) (T_e - T_g) \quad (6)$$

$$\left(\frac{dT_e}{dt} \right)_{O_2} = -4.7 \times 10^{-16} n(O_2) T_e (T_e - T_g). \quad (7)$$

n is number of particles cm^{-3} , T in $^\circ\text{K}$ and dT/dt in deg s^{-1} .

To evaluate Eqs. (5), (6) and (7), the number densities $n(O)$, $n(N_2)$ and $n(O_2)$ are taken from the CIRA 1965 model. The rotational loss parameter $(G\bar{\nu}/n(N_2))$ in Eq. (6) is calculated according to Dalgarno and Moffett [10]. The energy Q_T needed to maintain the observed temperature difference is then calculated, and is shown in Fig. 3.

5. Discussion

It is evident from Fig. 1 that the measured electron temperatures (T_e) are more than the CIRA model neutral gas temperatures throughout the E region. In Fig. 2, the $T_e - T_g$ and the current density, J , profiles are shown for comparison.

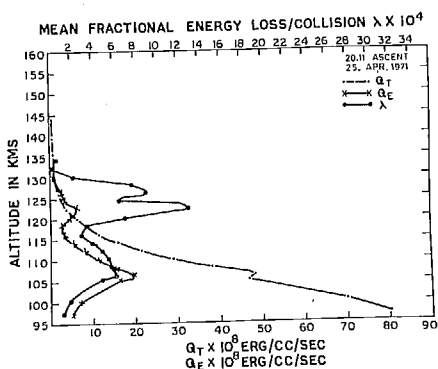


Fig. 3. Experimentally obtained values of Q_E the power generated by the electrojet, theoretical estimates of Q_T the power needed to maintain the observed temperature difference $T_e - T_g$, and the mean fractional energy loss λ per collision of electrons with neutrals plotted as functions of altitude.

It is seen that there is good correspondence between $T_e - T_g$ and J throughout the main electrojet layer around 106 km. The $T_e - T_g$ profile shows a rather broad maximum compared with the current density maximum, implying that the heating is not localized, but extends slightly above the electrojet layer.

The λ values shown in Fig. 3, are slightly higher than those used by Kato [5]. The calculated λ values show that $\lambda > 2m_e/M$, where m_e is the electronic mass (9.1×10^{-28} g) and M is the mass of the heavy particle in collision (5×10^{-23} g). This implies that the collisions are inelastic in the region considered.

The vertical profile of λ shows a large peak between 120 and 130 km. Part of this increase in λ is due to the small increase in current J in this altitude range. This increase in J is due to a second current layer often seen in equatorial J measurements [12]. The broad peak in $T_e - T_g$ around 110 km may partly be due to the effect of this second current layer. Even after removing the effects of this possible second current layer, λ shows a peak around 125 km. The magnitude of this peak depends largely on the rate of fall of electrojet current with altitude above the peak of the electrojet at 107 km. Examining Eq. (3), ν_e falls rapidly with altitude and $[kn_e\nu_e(T_e - T_g)]^{-1}$ has large values beyond 115 km. Since J^2/σ_3 has significant values between 115 and 130 km, λ shows large values in this region. This means that the electrons in this region attain large energies between collisions. Therefore, one can expect the energy transfer per collision of electrons with neutrals to be large in this region.

The Q_T profile shows a slight deviation from its normal trend at 106 km. The Q_E value at 106 km is nearly one third of the Q_T value at the same altitude. This implies that the measured strength of the electrojet current J can account for only one third of the observed difference in temperature $T_e - T_g$. The difference between Q_T and Q_E decreases above 106 km.

The discrepancy between the theory and the experiment can be attributed to the following factors: (i) The experimentally measured electron temperatures could be slightly higher than the actual temperatures in the region. (ii) The CIRA model gas temperatures T_g used in the calculation may not represent the actual gas temperatures in this region. The measurements by Knudsen and Sharp [11] at mid-latitudes suggests that $T_i \cong T_g$ and that the measured T_g values agree with the model gas temperatures up to 120 km. However, there are no direct gas temperature measurements over the equator. (iii) The dependence of ν_e on T_e can increase the ν_e values used here by a factor $(T_e/T_g)^{1/2}$ which is of the order 1.6 around 106 km. This increase in ν_e will reduce the λ values by a factor 0.6 near 106 km. The new λ value thus obtained for the region around 106 km agree with the λ value used by Kato [5] for a difference in temperature of 440°K.

6. Conclusions

1. The pronounced peak of $T_e - T_g$ around 106 km is due to the Joule heating effect of the electrojet.
2. The electron temperatures measured are higher than the CIRA model gas temperatures all over the E region.
3. The observed electrojet strength J can account for only one third of the observed temperature difference $T_e - T_g$.
4. The λ values obtained show that in the region of the electrojet the collisions between electrons and neutrals are inelastic.

To obtain a good understanding of the phenomenon of Joule heating it is

necessary to measure T_e , T_g , J and n_e in simultaneous or near simultaneous flights. It is also necessary to confirm the above findings by further experiments over the equator.

References

- [1] W. B. HANSON and F. S. JOHNSON, *Memoires Soc. R. Liège, Series 5*, 300 (1961).
- [2] A. DALGARNO, M. B. McELROY and R. J. MOFFETT, *Planet. Space Sci.* **11**, 463 (1963).
- [3] A. P. WILLMORE, *Proc. Roy. Soc.* **281**, 140 (1964).
- [4] J. E. GEISLER and S. A. BOWHILL, *J. Atmos. Terr. Phys.* **27**, 457 (1965).
- [5] S. KATO, *Planet. Space Sci.* **11**, 1297 (1963).
- [6] K. HIRAO and K. OYAMA, *J. Geomag. Geoelect.* **22**, 303 (1970).
- [7] T. S. G. SASTRY, *Space Research X*, 778 (1970).
- [8] S. PRAKASH, S. P. GUPTA, B. H. SUBBARAYA and C. L. JAIN, *Nature* **233**, 56 (1971).
- [9] K. MAEDA and H. MATSUMOTO, *Rep. Ionosph. Space Res. Japan* **16**, 1 (1962).
- [10] A. DALGARNO and R. J. MOFFETT, *Planet. Space Sci.* **9**, 439 (1962).
- [11] W. C. KNUDSEN and G. W. SHARP, *J. Geophys. Res.* **70**, 143 (1965).
- [12] T. S. G. SASTRY, *J. Geophys. Res.* **73**, 1789 (1968).

A Digital Pressure Transducer

T. S. G. SASTRY, H. S. MAZUMDAR & S. SAMPATH

Physical Research Laboratory, Ahmedabad

Received 26 October 1974

A digital pressure gauge that can measure pressures from 1 atm down to 0.5 mm Hg was developed using indigenously available materials and components. The performance of these gauges was tested by flying them on Russian M-100 rockets and comparing their performance with the performance of conventional meteorological pressure gauges used in standard meteorological payloads. Details of instrumentation and results of test flights have been presented.

1. Introduction

THE DIGITAL pressure gauge consists of an ionization chamber containing a radioactive source. The output of the chamber is connected to an electrometer which, in turn, is coupled to a blocking oscillator. The output of the oscillator is a series of pulses. At low pressures the number of molecules of air ionized in the chamber by the α emissions from the source is small resulting in a small electrometer current and a small pulse rate. At higher pressures, the pulse rate increases as larger current is detected by the electrometer tube. Low pressure gauges devised on this principle for laboratory purposes have been described by Downing and Mellen¹, Sibley and Roehrig², etc. The gauge described here is of the type devised by Vanderschmidt³ and Cambou *et al.*⁴.

2. Instrumentation

Gauges with different configurations were designed to measure atmospheric pressure up to 50 km altitude, by balloons as well as small and medium sized rockets. Fig. 1 shows some of these instruments. Gauges 1 (a) and 1 (b) use ionization chambers of conical shape cut out of rectangular blocks of brass. The conical chambers are similar in configuration to the chamber described by Cambou *et al.*⁴. Four elliptical windows cut in the cone ensures quick equalization of pressure inside the chamber and the environment whose pressure is to be measured. The collector electrode is a tungsten wire of 0.5 mm in diameter. It runs centrally inside the chamber and is held in position at the broad end of the cone by a brass disc sandwiched between a pair of teflon rings. These teflon rings insulate the central electrode from the body of the chamber. The radioactive source used is polonium 210 of strength 50 μ curie or americium 241 of strength of 30 μ curie. The radioactive material is electrochemically deposited on a silver coin of 15.5 mm diameter and 3 mm thickness.

The coin bearing the radioactive material is enclosed in a brass cap and screwed on to the narrow end of the chamber. All brass parts are polished and silver plated. The dimensions of the chamber and the windows and the angle of the cone are optimized to obtain the desired linearity between the collector current and the ambient pressure.

The gauge shown at 1 (c) is made out of a rectangular aluminium block. A circular hole of 1 cm diameter cut at the centre of the block along its length forms the chamber. The silver coin bearing the radioactive source is fitted at one end of the chamber and the tungsten wire electrode is introduced axially from the opposite end. The tungsten wire electrode is held in position with teflon discs as in the conical chamber. A 1 cm diameter window is cut on one side of the block to ventilate the chamber to outside air. This chamber is easy to mount and is more compact compared to the conical chamber.

The electronic circuits used are shown in Fig. 2. The circuit 2 (a) uses an electrometer tube amplifier coupled to a blocking oscillator. It is similar to the one used by Vanderschmidt, except for a few changes to make the output compatible with the telemetry requirements.

A more versatile circuit was developed which is shown in Fig. 2 (b). The potential at the grid of the electrometer tube at any instant is a function of the chamber capacitance and the charge on the central electrode. If the chamber capacitance and stray capacitance at the input of the electrometer tube remains constant, the potential at the grid of the electrometer tube rises as the charge accumulates on the chamber collector electrode. This potential is amplified by the electrometer tube and is fed to a comparator P which is connected in feedback loop with the transistor Q_1 to form a mono. When the probe potential at the input of the EM tube increases above a certain limiting value due to charge

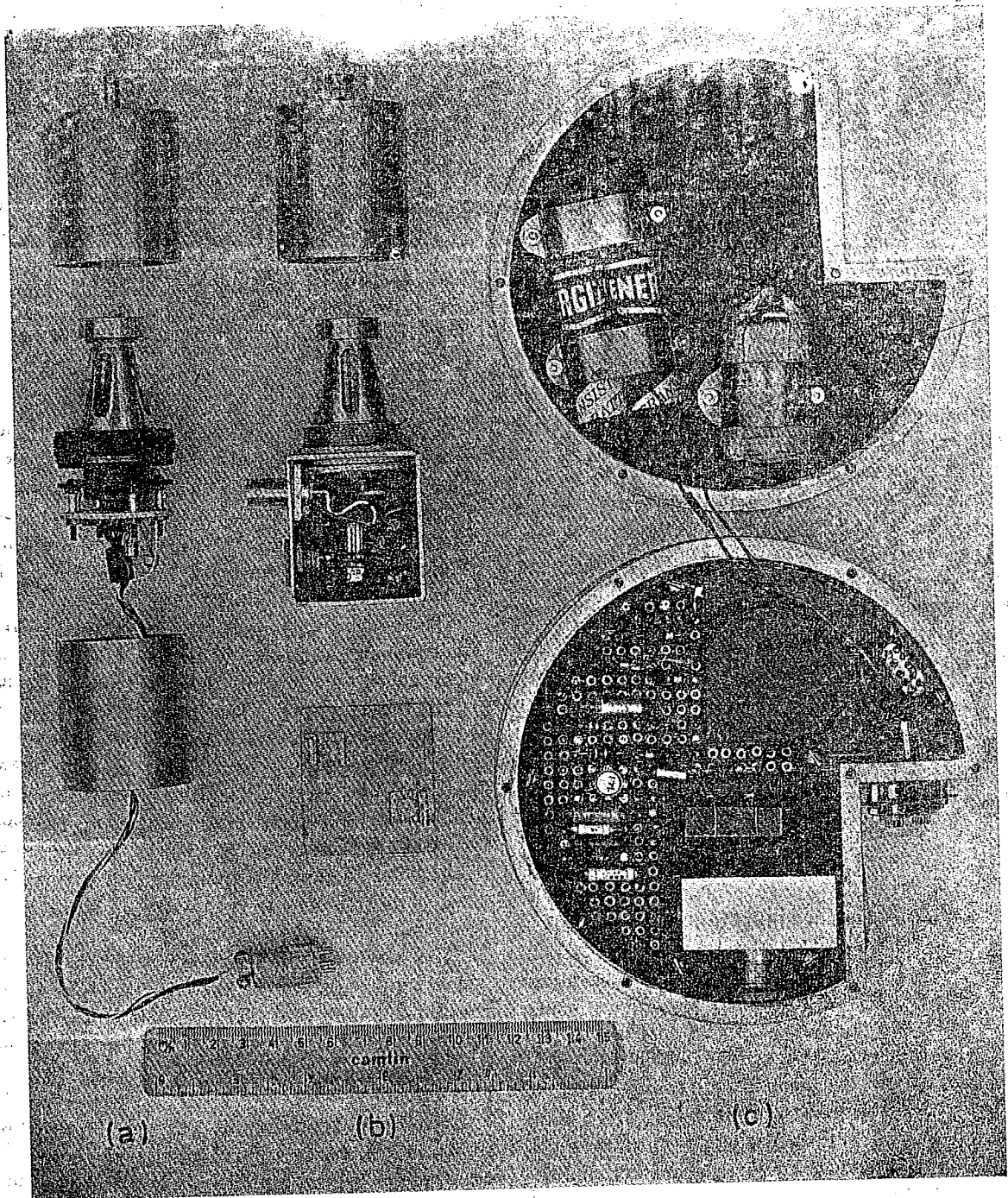


Fig. 1—The digital pressure gauges

accumulation at the grid, the mono generates a positive going pulse which is fed to the chamber through capacitor C. This pulse reaches the grid of the EM tube via the chamber capacitance and drives it to conduction, thus discharging the charge accumulated on the collector electrode of the chamber. At the end of the pulse from the mono, the central electrode is ready to collect the charges due to ionization in the chamber again and the process repeats.

The charging rate of the chamber is proportional to the ambient density of air and if the temperature of air in the chamber does not change appreciably, the mono gives a pulse output whose frequency is proportional to ambient pressure. These pulses are fed to telemetry through the driver transistor Q_2 . In this circuit it is possible to adjust the pulse rate appropriate to the ground pressure by adjusting the feedback. The sensitivity of the chamber depends on

the capacitance of the chamber and stray capacitance of the input circuit. These must be stable and made as small as possible.

3. Preflight Calibration

The pressure gauges made for rocket flights will have to be calibrated after potting the section in which the electronic circuits are enclosed. The potted unit is kept in vacuum chamber fitted with a standard pressure gauge. The voltage for the chamber and the circuit is fed through vacuum feed-throughs. The output of the chamber is connected to a digital counter. The counting rate at normal ground pressure is adjusted between 600 and 700 pulses per second. The counting rates for different pressures are noted as the evacuation of the chamber proceeds. The calibration curve of pressure against counting rate for the unit flown on flight 08-106 is shown in Fig. 3. It is found that the curve is linear even up to fraction of a mm. of pressure.

4. Flight Results

A Russian M-100 rocket (FL 08-106) carrying the digital pressure gauge was launched from Thumba on January 13, 1973 at 2120 hrs IST. Earlier the same day at 2000 hrs IST a standard meteorological payload (FL 08-105) was launched to measure atmospheric pressure, temperature and wind velocity. Both the rockets carried radar transponders to enable trajectory determination. The rocket FL 08-105 payload contained two Pirani (hot wire) manometers for measuring pressure from 50 to 5×10^{-3} mm Hg and two membrane manometers operating in the range 5 to 250 mm Hg. Pressure measurements from 760 to 350 mm Hg were obtained by balloon borne meteorological payload which usually precedes a standard Met. M-100 flight. The procedure adopted to derive the pressure values from data sent by a standard Met. M-100 payload has been described by Narayanan⁵. In Fig. 4 the pressure measurements from the digital pressure gauge of FL 08-106 have

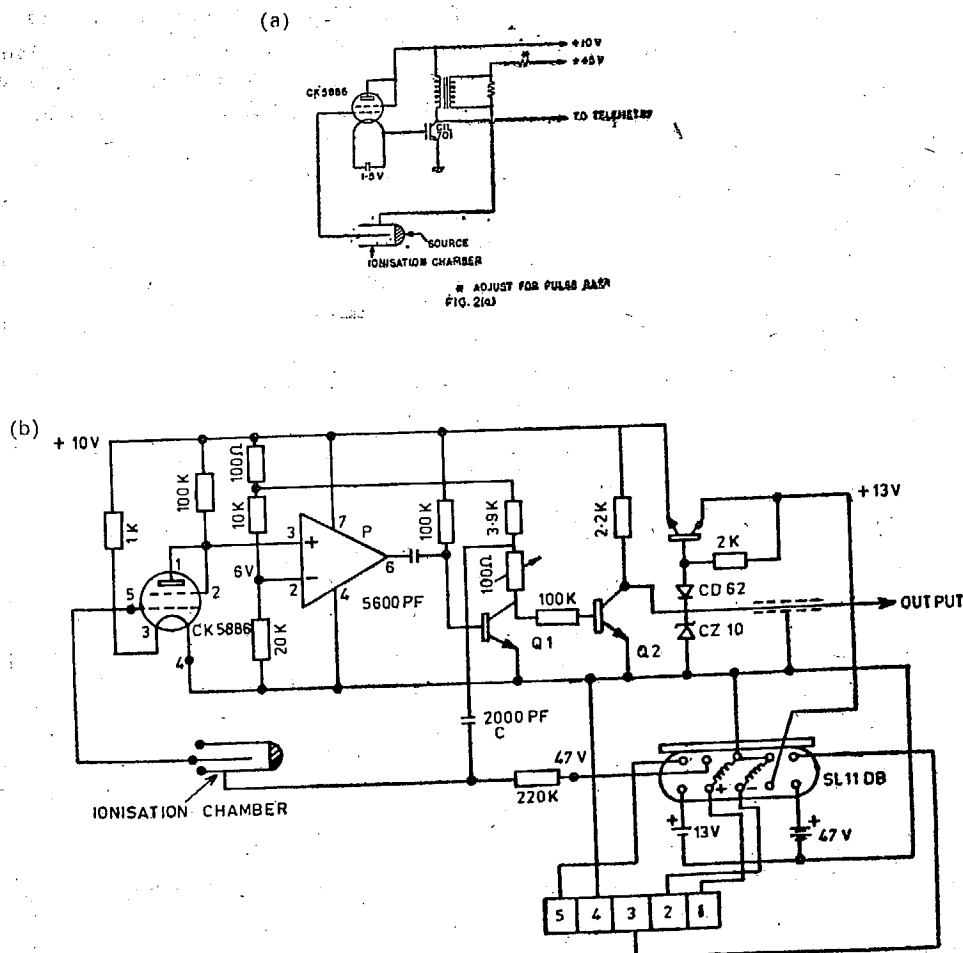


Fig. 2—The electronic circuits used for the rocket-borne digital pressure gauges

been compared with the pressure values derived from the meteorological rocket (FL 08'105) and the balloon data. It is seen that the agreement between the atmospheric pressure measured by the two independent methods is good especially above 20 km altitude.

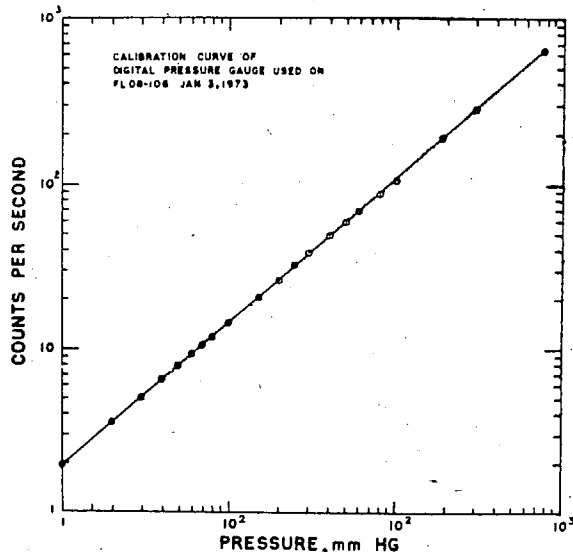


Fig. 3—Preflight laboratory calibration curve of pressure against counting rate for a typical digital pressure gauge instrumented for a rocket payload

A second digital pressure gauge was flown on 11 January 1973 at 2142 hrs IST on M-100 FL 08'108. This rocket did not reach the full expected altitude of 88 km but data could be obtained both on ascent and descent. The data from this flight along with CIRA model pressure has been shown in Fig. 5. In the flight 08'106 launched on January 3, the pressure gauge was mounted in the cylindrical part of the nose cone where the effects of the wake on the measured pressure are least. In the flight FL 08'108 the gauge was located in the conical part of the nose cone where the effects of the wake are more. This appears to have affected the measured ambient pressure at the sensor.

5. Conclusions

The performance of the digital pressure gauge described here compares well with the performance of conventional meteorological pressure gauges. It has the added advantage that its output is digital and hence easy to transmit and count. It also has a wide dynamic range for pressure measurements. Its response to pressure changes, stability of calibration and accuracy of measurement compares well with similar gauges imported and flown in the first few rocket flights from Thumba.⁶ As a laboratory vacuum

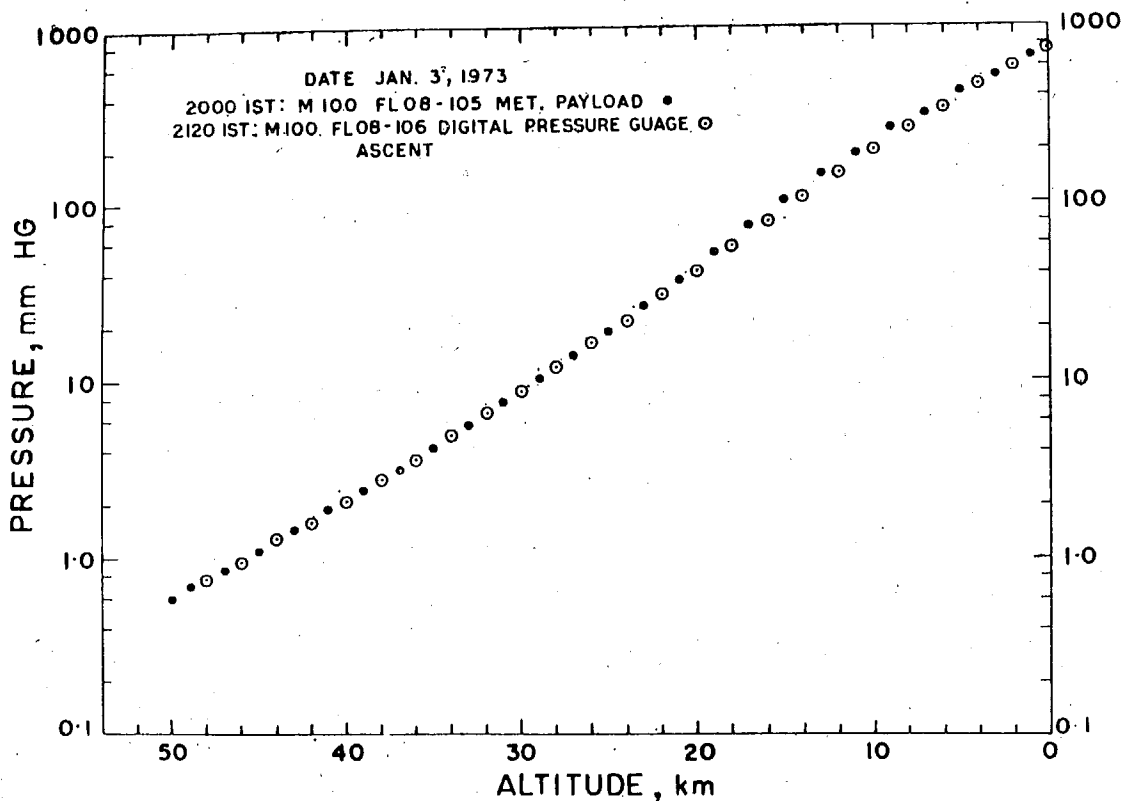
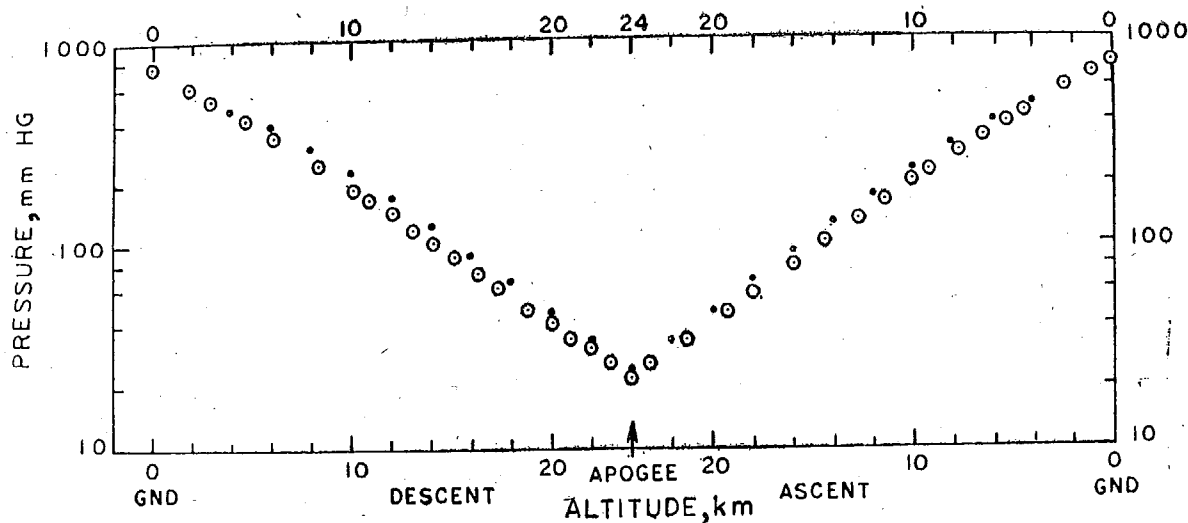


Fig. 4—Comparison of pressure measurements obtained by the digital pressure gauge on FL 08'106 and those obtained from a standard meteorological payload of FL 08'105



DATE: JAN. 10, 1973. 2000 IST FL 08-107 MET. PAYLOAD •

JAN. 11, 1973. 2142 IST. FL 08-108 DIGITAL PRESSURE GAUGE ○

Fig. 5—Comparison of pressure measurements obtained from the digital pressure gauge flown on FL 08-108 and pressure from CIRA model

pressure gauge, its range and performance can be improved on the lines described by Sibley and Roehrig². As a rocket-borne instrument, the range of the digital pressure gauge can be extended to 10^{-2} mm Hg by connecting two chambers in parallel. Using the principle described here, a differential chamber pressure gauge, sensitive to small changes of atmospheric pressure can be instrumented. Such an instrument will be useful as a laboratory barograph.

Acknowledgement

The authors wish to thank Dr V. K. Iya, Isotope Division, Bhabha Atomic Research Centre, Bombay, for preparing the radioactive sources used in these

experiments. They thank Dr V. Narayanan of TERLS for analyzing the pressure data from meteorological payloads. The authors acknowledge with pleasure the cooperation provided by him and his group.

References

1. DOWNING, J. R. & MELLEN, G., *Rev. scient. Instrum.*, **17** (1946), 218.
2. SIBLEY, B. & ROEHRIG, R., *Electronics*, **26** (1953), 176.
3. VANDERSCHMIDT, G. F., *Electronics*, **32** (1959), 60.
4. CAMBOU, F., COTIN, F. & REME, H., *Ann. Geophys.*, **20** (1964), 346.
5. NARAYANAN, V., *Studies of the troposphere, stratosphere and mesosphere over the equatorial India*, Ph. D Thesis, University of Kerala, Trivandrum, 1973.
6. SASTRY, T. S. G., *J. scient. ind. Res.*, **23** (1964), 334.